"On the growth and mechanical properties of non-oxide perovskites and the spontaneous growth of soft metal nanowhiskers"

Von der Fakultät für Georessourcen und Materialtechnik
der Rheinisch-Westfälischen Technischen Hochschule Aachen

zur Erlangung des akademischen Grades eines

Doktors der Ingenieurwissenschaften

genehmigte Dissertation
vorgelegt von **M.Sc.**

Tetsuya Takahashi

aus Tochigi, Japan

Berichter: Univ.-Prof. Jochen M. Schneider, Ph.D.
Professor Dr.-Ing. Dierk Raabe

Tag der mündlichen Prüfung: 18. Januar 2013

Materials Chemistry Dissertation

No.: 19 (2013)

Tetsuya Takahashi

On the growth and mechanical properties of non-oxide perovskites and the spontaneous growth of soft metal nanowhiskers

Shaker Verlag
Aachen 2013

Bibliographic information published by the Deutsche Nationalbibliothek
The Deutsche Nationalbibliothek lists this publication in the Deutsche Nationalbibliografie; detailed bibliographic data are available in the Internet at http://dnb.d-nb.de.

Zugl.: D 82 (Diss. RWTH Aachen University, 2013)

Printed in Germany.

ISBN 978-3-8440-1903-2
ISSN 1861-0595

Shaker Verlag GmbH • P.O. BOX 101818 • D-52018 Aachen
Phone: 0049/2407/9596-0 • Telefax: 0049/2407/9596-9
Internet: www.shaker.de • e-mail: info@shaker.de

Abstract

It has previously been suggested based on *ab initio* calculations that perovskites with the general formula of AB_3X, where *A* and *B* are metals, and *X* is B, C, or N, may exhibit unique mechanical properties such as superior ductility, and hence damage tolerance. In the first part of this thesis, the mechanical behavior of ternary perovskite borides and iron based perovskite nitrides is explored. YPd_3B, Fe_4N, $ZnFe_3N$, and $PdFe_3N$ thin films were synthesized by combinatorial magnetron sputtering, and the mechanical properties thereof were probed by nanoindentation. Generally, the measured elastic moduli were in good agreement with *ab initio* data. The evaluation of the critical shear stress for the onset of plasticity suggests that YPd_3B, Fe_4N, and $PdFe_3N$ can be classified as ductile materials, which is also consistent with the prediction from *ab initio* calculations.

The second part of the work demonstrates a possible application of the combinatorial thin film approach for the fabrication of one-dimensional nanostructured materials. In-Y thin films with a compositional spread were deposited by combinatorial magnetron sputtering. It was found that In-whiskers were extruded spontaneously from the film surface upon exposure to atmosphere. In-whisker growth was accompanied by an increase in oxygen content in the films. The morphology and extrusion kinetics of In-whiskers were affected by the local chemical composition. The results presented here enable controlled processing of one-dimensional nanostructured materials with respect to morphology and growth kinetics.

Zusammenfassung

Ab initio-Berechnungen von Perovskiten der allgemeinen Formel AB_3X, wobei *A* und *B* Metalle sind und *X* für eines der Elemente B, C oder N steht, lassen auf außergewöhnliche mechanische Eigenschaften dieser Stoffklasse schließen, insbesondere eine hohe Duktilität und somit hohe Schadenstoleranz.

Im ersten Teil dieser Arbeit wird das mechanische Verhalten ternärer, perovskitischer Boride und Nitride untersucht. YPd_3B-, Fe_4N-, $ZnFe_3N$- und $PdFe_3N$-Schichten wurden mittels kombinatorischem Magnetronsputtern synthetisiert und ihre mechanischen Eigenschaften mittels Nanoindentation bestimmt. Der Vergleich der gemessenen Werte für den Elastizitätsmodul zeigt eine gute Übereinstimmung mit den ab initio-Daten. Aus der Analyse der kritischen Scherspannung zur Aktivierung plastischer Verformung wird geschlossen, dass YPd_3B, Fe_4N und $PdFe_3N$ als duktile Werkstoffe einzustufen sind. Dies ist ebenfalls konsistent mit den Ergebnissen der ab initio-Berechnungen.

Der zweite Teil der Arbeit befasst sich mit der Evaluierung der potentiellen Anwendung der kombinatorischen Dünnschichtsynthese zur Herstellung eindimensionaler nanostrukturierter Werkstoffe. In-Y-Dünnschichten wurden über einen großen Zusammensetzungsbereich mittels kombinatorischem Magnetronsputtern abgeschieden. Bei anschließender Auslagerung der Dünnschichten an Luft wurde die spontane Extrusion von In-Whiskern aus der der Schicht beobachtet. Das Whisker-Wachstum korreliert mit einem Anstieg des Sauerstoffgehalts der Schichten. Die Morphologie und die Wachstumskinetik der Whisker werden direkt durch die lokale chemische Zusammensetzung beeinflusst. Die hier erarbeiteten Zusammenhänge zwischen dem Bildungsmechanismus, der

Wachstumskinetik und der Whiskermorphologie leisten einen Beitrag zur gezielten Herstellung eindimensional nanostrukturierter Werkstoffe.

List of publications contributing to this thesis work

T. Takahashi, A. Abdulkadhim, D. Music, and J.M. Schneider
Spontaneous formation of In-Whiskers on YIn_3 thin films deposited by combinatorial magnetron sputtering
IEEE Transactions on Nanotechnology 10 (5) (2011) 1202-1208.

T. Takahashi, D. Music, and J.M. Schneider
γ'-$ZnFe_3N$ thin films: A proposal for a moderately ductile, corrosion-protective coating on steel
Scripta Materialia 65 (5) (2011) 380-383.

T. Takahashi, J. Burghaus, D. Music, R. Dronskowski, and J.M. Schneider
Elastic properties of γ'-Fe_4N probed by nanoindentation and ab initio calculation
Acta Materialia 60 (5) (2012) 2054-2060.

T. Takahashi, D. Music, and J.M. Schneider
Influence of magnetic ordering on the elastic properties of $PdFe_3N$
Journal of Vacuum Science & Technology A 30 (3) (2012) 030602-1-5.

T. Takahashi, R. Iskandar, F. Munnik, D. Music, J. Mayer, and J.M. Schneider
Synthesis, microstructure, and mechanical properties of YPd_3B thin films
Journal of Alloys and Compounds 540 (2012) 75-80.

List of publications not contributing to this thesis work

D. Music, J. Burghaus, **T. Takahashi**, R. Dronskowski, and J.M. Schneider
Thermal expansion and elasticity of $PdFe_3N$ within the quasiharmonic approximation
The European Physical Journal B 77 (3) (2010) 401-406.

A. Abdulkadhim, **T. Takahashi**, D. Music, F. Munnik, and J.M. Schneider
MAX phase formation by intercalation upon annealing of TiC_x/Al ($0.4 \leq x \leq 1$) bilayer thin films
Acta Materialia 59 (15) (2011) 6168-6175.

A. Abdulkadhim, M. to Baben, **T. Takahashi**, V. Schnabel, M. Hans, C. Polzer, P. Polcik, and J.M. Schneider
Crystallization kinetics of amorphous Cr_2AlC thin films
Surface and Coatings Technology 206 (4) (2011) 599-603.

T. Gebhardt, D. Music, **T. Takahashi**, and J.M. Schneider
Combinatorial thin film materials science: From alloy discovery and optimization to alloy design
Thin Solid Films 520 (17) (2012) 5491-5499.

Y. Jiang, R. Iskandar, M. to Baben, **T. Takahashi**, J. Zhang, J. Emmerlich, J. Mayer, C. Polzer, P. Polcik, and J.M. Schneider
Growth and Thermal Stability of $(V,Al)_2C_x$ Thin Films
Journal of Materials Research 27 (19) (2012) 2511-2519.

Acknowledgements

First of all, I would like to express my gratitude to my supervisor, Prof. Jochen M. Schneider, for giving me the opportunity to conduct this thesis work. Your kind support, motivation, scientific discussion and encouragement were indispensable for me during working in your group.

I thank Dr. Music for your great support to me during my research work. You could always encourage and help me. Scientific discussion with you was very enjoyable and fruitful. I also thank Dr. Mraz. My current experimental skills and knowledge of vacuum science and thin film depositions were largely originated from you. When I joined the group without any knowledge and experience on this field, you could teach and train me with patience. You were always very cooperative and supportive. I am thankful to all the scientific co-workers in the group for giving me scientific as well as technical supports.

I thank all the members in the mechanical and electrical workshops. This thesis work does not exist without your professional technical supports. I also enjoyed working together with you to develop experimental equipments and to solve technical problems. In particular, my special thanks go to the head of mechanical workshop, Herr Horbach, who could provide me with his expertise knowledge and advices in developing mechanical components. I might give you a large number of terrible technical drawings, but you could kindly correct them, and even suggest much better solutions. Working with you was always productive. Supports from all the members in administrative and networks are also greatly acknowledged.

Last but no the least, I sincerely thank my father and mother for your never ending encouragement and support. I thank my wife, Yoshie, for your support, patience, and encouragement. I could not complete the work without you.

Table of Contents

List of Figures and Tables

Figure 2.8
RHEED analysis for combinatorially deposited Fe-Mn thin film with composition spread from 14 to 32 at.%Mn. (a) RHEED pattern measured at 30 kV acceleration voltage. Simulated RHEED patterns for BCC structure assuming (b) (001) fiber texture with 10° texture a xis distribution, (c) (111) fiber texture with 10° texture axis distribution, a nd (d) (011) fiber texture with 10° texture axis distribution. Experimental pattern is in good agreement with simulated pattern for (111) fiber texture (e). (f) Schematic illustration showing grain orientation of (111) fiber textured film.

Figure 2.9
Schematic illustration of Multi-beam Optical Sensor system (MOS, kSA) for film stress measurement. The figure is produced by referring to an application note written by E. Chason for k-Space Associates Inc., USA.

Figure 2.10
Residual stress evolution in Ti thin films as a function of substrate bias voltage.

Figure 2.11
Schematic illustration of the combinatorial sputter deposition system built in-house equipped with three magnetron sources.

Figure 2.12
Photographs for (a) magnetron source for ϕ39 mm target and (b) cluster flange equipped with three magnetron sources. Both components are built in-house. The inset in figure(a) shows the discharge plasma on a Cu target sputtered in 5 mTorr of Ar at a DC power of 100 W.

Figure 2.13
Schematic illustration for sputter deposition system built in-house equipped with a single magnetron source.

Figure 2.14
Schematic illustration showing signals emitted from sample surface by the interaction between high energy electron beam and sample matter.

Figure 2.15
Schematic illustration for setup of SEM-EDX equipment.

Figure 2.16
Schematic illustration for X-ray diffraction showing the geometrical relationship between incident and diffracted X-rays performed on a powder or polycrystalline sample.

Figure 2.17
(a) Schematic illustrations for Ewald sphere construction for diffraction condition. (b) Geometrical relationship between incident and diffracted X-rays.

Figure 2.18
Schematic representation of nanoindentation (a) and load-displacement curve (b).

Figure 2.19
Screen shot of the graphical user interface program developed for load-displacement curve simulation.

Figure 2.20
Load-displacement curve measured on fused silica using a blunt Berkovich indenter tip. The loading and unloading curves are reversible up to an indentation load of 300 μN.

Figure 2.21
3D laser microscope image of a blunt Berkovich indenter tip: (a) 3D height image and (b) line profile at the tip.

Figure 2.22
Stress field analysis for nanoindentation on Si(100) wafer measured by a blunt Berkovich indenter tip. (a) Measured data and calculated Hertzian curve. Deviation from Hertzian curve is observed at a critical load of about 770 μN. (b) Calculated local maximum shear stress, and (c) hydrostatic pressure distributions at the critical load.

Figure 2.23
Sources of structural compliance [29]. (a) Specimen scale deformation. (b) Elastic heterogeneities such as free edges or (c) interface with a dissimilar material. (d) Layered specimen. The figures are modified from ref. [29].

Figure 2.24
Multi-loading and unloading function used for correction of structural compliance, C_s.

Figure 2.25
Correction method for structural compliance, C_s. (a) Example of load–displacement curves measured for γ′-Fe_4N bulk-like sample using multi-loading and unloading function. Both data before and after the correction of structural compliance, C_s, are presented for comparison. (b) Linear plot to determine the structural compliance value, C_s.

Figure 3.1
Composition-structure map created from combinatorial Y-Pd thin film. (a) Composition spread measured by EDX. The composition map includes total 145 measurement points with a grid size of 3.5 mm. (b) XRD intensity map measured along the composition gradient. The map contains 13 diffraction data. The color intensity is constructed by data interpolation and subsequent smoothening.

Figure 3.2
Pd-Y phase diagram showing a Pd-rich part reconstructed based on ref. [19].

Figure 3.3
Schematics of targets–substrate arrangement for sputter deposition of Y-Pd-B thin films from elemental targets.

Figure 3.4
XRD patterns for (a) binary $YPd_{3.02}$ and (b) ternary $YPd_{2.73}B_{1.18}$ thin films deposited on Si(100) substrates. The inset emphasizes the (100) superlattice diffraction detected for $YPd_{2.73}B_{1.18}$ film.

Figure 3.5
Change in lattice parameter of YPd_3B_x with B content gradient probed on combinatorial Y-Pd-B thin film: (a) EDX results for B content, and (b) lattice parameters measured from (111) and (200) diffraction planes.

Figure 3.6
TEM micrograph showing the cross sectional microstructure of a $YPd_{2.73}B_{1.18}$ thin film: (a) Bright field image and (b) electron diffraction pattern. The patterns can be identified as fcc-type structure. Only (111) and (200) diffractions are indexed here.

Figure 3.7
Fiber texture plots obtained for (111) and (200) diffraction planes in $YPd_{2.73}B_{1.18}$ thin film. The inset schematics illustrates the co-existence of both (111) and (200) fiber textures.

Figure 3.8
Initial portion of load–displacement curve measured on $YPd_{2.73}B_{1.18}$ thin film using a blunt Berkovich indenter tip. A theoretical curve calculated by Hertz contact theory is also plotted for comparison.

Figure 7.1
Schematic illustration of combinatorial magnetron sputtering set-up for deposition of In-Y thin films with composition gradient.

Figure 7.2
Photograph of In-Y thin film with lateral composition gradient deposited on 2 inch Si-wafer after exposure to atmosphere for 30 hours.

Figure 7.3
SEM micrographs showing a variety of In-whisker morphologies obtained from the marked area in Figure 7.2: (a) large area, low magnification image, and (b)-(g) high magnification images taken from positions denoted by (b)-(g) in Figure 7.3(a).

Figure 7.4
SEM micrographs showing cross-sectional features of a film with composition gradient: (a) low magnification image (left side corresponds to In-rich area), high magnification images of a top (b), and a bottom (c) part of In-whiskers grown. The micrographs were taken after one month exposure to atmosphere.

Figure 7.5
Series of SEM micrographs showing temporal growth behavior of In-whisker with different atmosphere exposure time: (a) as-deposited, (b) after 3 min, (c) 6 min, (d) 10 min, (e) 20 min, and (f) 80 min.

Figure 7.6
Schematic illustration of the SEM observation process to capture the growth behavior of In-whisker upon atmosphere exposure. The process of (a) evacuation, (b) micrograph capturing, and (c) atmosphere exposure is repeated several times.

Figure 7.7
Temporal structural evolution on film surface with different atmosphere exposure time: SEM micrographs for (a) as-deposited, (b) after ~2 hours, (c) after ~52 hours, and (d) corresponding XRD patterns.

Figure 7.8
SEM micrograph showing area of retardation of In-whisker growth after being repeatedly exposed to an electron beam.

Figure 7.9
Temporal changes of film compositions and In-whisker growth with different atmosphere exposure time for two different as-deposited films with 22

Chapter 1
Introduction

1.1 Introduction

The term “material” may be differentiated from “substance” in a sense that materials can be utilized for specific applications. For instance, we have been using a huge amount of Si as semiconductor material sustaining the electronic and information technologies in the present time. Whereas Si is one of today’s essential materials for the production of high-tech electronic devices, Si based compounds have been utilized by humans since the Stone Age. They employed stones, a typical constituent of which is SiO_2, as materials for tools. At the time of the Stone Age, ultra pure Si, even if it had been available, might have been a useless material. Instead, stones exhibiting mechanical properties such as high hardness and toughness would have been a more valuable material at the time. In contrast, nowadays, we are not enthusiastic to look for and pick up flint stones in nature to produce, for instance, sophisticated cutting tools applied in metal-machining for automotive components.

Material’s properties are determined by the chemical constituents, and by the “structure”. The structure can be defined on different length-scales ranging from atomistic to macroscopic: Electronic structure, crystal structure, microstructure, mesoscopic-structure, and macrostructure. The understanding of the correlations between chemical composition, structure and properties are essential in materials science and engineering. Although materials may be designed to some extent based on one’s experience and intuition, recent progress in the physical foundation and computational resources allows us to design materials guided by quantum mechanical data and to simulate the behavior of materials within a computer [1]. Hence, computational materials science enables knowledge based materials design.

The material's structure can be affected by the synthesis method or processing protocol. Even if the chemical compositions are identical, different synthesis routes may provide materials with different structure, and hence properties. For instance, the strength and hardness of a thin film material is typically much higher than that of the corresponding bulk material counterpart [2]. This is mainly due to significantly finer grain structures of thin films compared to bulk materials. Some synthesis methods can be characterized as a highly energetic non-equilibrium process where the formation of thermodynamically meta-stable materials can readily be achieved [3]. A typical example of such processes includes physical vapor deposition (PVD) techniques like evaporation, sputtering, and cathodic arc depositions. Because of its non-equilibrium nature, PVD may enable fabrication of new materials which cannot be realized by conventional bulk synthesis routes [4]. In combination with computational materials science tools, PVD is a powerful experimental tool for the design of new materials. The understanding of the structural evolution of thin films during PVD and the optimization of the properties is a common topic of interest in materials science of thin films [5, 6].

State of the art materials characterization tools are essential for materials design. For example, the depth-sensing nanoindentation method [7] is a common tool to investigate the local mechanical properties. The elastic and plastic properties of each microstructural constituent forming a bulk polycrystalline material can be studied. The mechanical properties of thin films can also be evaluated quantitatively by nanoindentation with the minimal influence of substrate. Also, nanoindentation exhibits large spatial resolution and is ideally suited for so-called, combinatorial materials science [8-10] enabling high-throughput study of the relationship between the mechanical properties and chemical composition.

The overall goal in this work is to contribute towards the basic understanding of the correlation between material's composition, material's

structure, and material's properties through combination of theory and experiment. PVD is employed to synthesize materials. The detailed descriptions of the methods used in the present work are introduced in the following chapter, Chapter 2.

The focus of the present works lies on two topics: **1)** the synthesis and mechanical properties of non-oxide perovskite thin films, and **2)** spontaneous whisker growth from thin films containing soft metal and rare earth element. The following sections explain briefly the contributions for each study.

1.2 Synthesis and mechanical property of non-oxide perovskite thin films

The development of damage tolerant materials exhibiting high stiffness, hardness, and strength is a challenge in materials engineering. Ceramic materials exhibit covalent and/or ionic bonds and are generally high hardness, strength, stiffness, chemical inertness, and high temperature resistance. They are also brittle. In contrast, many metallic materials with dominantly metallic bonding are easily plastically deformable, and hence highly ductile. However, their mechanical rigidity and chemical stability such as stiffness, strength, hardness, and corrosion resistance are in general inferior to ceramic materials.

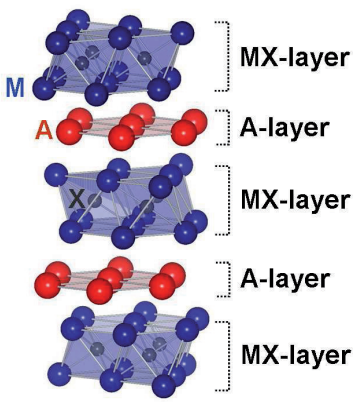

Figure 1.1 Nanolaminated structure of MAX phase, e.g. M_2AX, where covalent -ionic MX-layers are interleaved with metallic A-layers.

There is an interesting class of material with a general formula of $M_{n+1}AX_n$, or the so-called *MAX* phases, where *M* is a transition

metal, *A* is an *A* group element, *X* is either C or N, and *n* is between 1 and 3 [11-13]. Examples of MAX phases include Cr_2AlC, Ti_2AlC, Ti_3SiC_2, V_2AlC, to name just a few. Although MAX phases can crystallographically be defined as a single phase, they are equipped with both features of metals and ceramics such as high stiffness, good thermal and electrical conductors, high thermal shock resistance, and machinable. These unusual features of MAX phases are due to the crystallographic structure, also referred to as nanolaminate structure, as shown in Figure 1.1. It is a layered hexagonal structure (space group $P6_3/mmc$) where ceramic *MX* layers are interleaved with metallic *A* layers. It can also be seen as a ceramic-metal composite material mixed in an atomistic layer scale.

It has been proposed previously based on *ab initio* calculations that ternary non-oxide perovskite phases may also exhibit an unusual combination of metallic and ceramic properties similar to MAX phases, and hence exhibit damage tolerance [14-17]. In contrast to MAX phases, perovskites comprise a simple cubic structure derived from an extension of face centered cubic (fcc) structure as shown in Figure 1.2. The fcc structure is one of the most common structures for metallic elements such as Al, Cu, Ag, Au, Pd, Pt, Ni, and γ-Fe. The unit cell contains one atom (8 x 1/8) at the corner sites and three atoms (6 x 1/2) at the face centered sites, respectively. An ordered form of the fcc structure is described as a general formula of AB_3 where *A* atoms are positioned at the corner sites and *B* atoms at the face centered sites, respectively. This structure is referred to as $L1_2$ or $AuCu_3$-type structure. A typical example of $L1_2$ phase is Ni_3Al which can be found in Ni-based super-alloys for high temperature structural applications [18]. The perovskite structure with a general formula of AB_3X is achieved when an interstitial atom, *X* (*X* = B, C, or N), is positioned at the body centered site of $L1_2$ unit cell. The *A* and *B* atoms can also be identical, for instance, in the case of the binary Fe_4N phase [19].

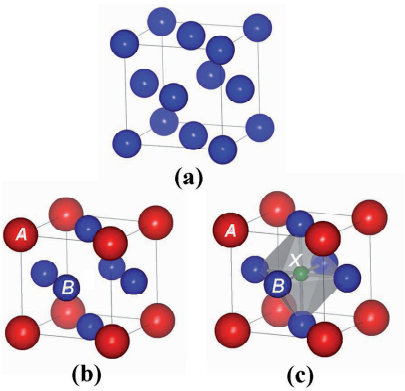

Figure 1.2 Crystal structures of (a) face centered cubic (fcc), (b) AB_3 binary ordered $L1_2$, and (c) AB_3X ternary perovskite.

Among many possible perovskite phases, perovskite borides with rare earth elements, RM_3B (R and M are metals), and iron-based perovskite nitrides derived from the binary Fe_4N, MFe_3N (M is metal), are main research interests in the present work. The ductility prediction of non-oxide perovskite phases by *ab initio* calculations served as motivation for this research. In this thesis work, therefore, the goal is to investigate the correlation between the electronic structure and mechanical properties of non-oxide perovskite. Chapter 3 is devoted to the synthesis and mechanical properties of YPd_3B perovskite boride thin films. In Chapter 4, the elastic properties of the binary iron-based γ'-Fe_4N perovskite nitride are studied. The synthesis of ternary iron-based MFe_3N thin films and their mechanical property characterization are presented in Chapter 5 ($ZnFe_3N$) and Chapter 6 ($PdFe_3N$).

1.3 Spontaneous whisker growth from thin films containing soft metal and rare earth element

In Chapter 7, the spontaneous soft metal whisker growth from alloys containing soft-metals and rare earth elements is investigated. The abnormal spontaneous growth of In-whiskers from In-Y thin films upon atmosphere exposure is observed. The whisker size and growth kinetics are highly affected by the chemical compositions of as-deposited In-Y thin films. The method presented here is suggested to be used as a possible new fabrication technique of one-dimensional nanostructured materials.

References

[1] D. Raabe, *Computational materials science*, Wiley-VCH, Weinheim (1998).
[2] R.P. Vinci, J.J. Vlassak, Annu. Rev. Mater. Sci. 26 (1996) 431.
[3] C. Suryanarayana, C.C. Koch, *Non-equilibrium processing of materials*, Pergamon, New York (1999).
[4] T. Gebhardt, D. Music, T. Takahashi, J.M. Schneider, Thin Solid Films 520 (2012) 5491.
[5] I. Petrov, P.B. Barna, L. Hultman, J.E. Greene, J. Vac. Sci. Technol. 21 (2003) 117.
[6] P.H. Mayrhofer, C. Mitterer, L. Hultman, H. Clemens, Prog. Mater. Sci. 51 (2006) 1032.
[7] W.C. Oliver, G.M. Pharr, J. Mater. Res. 7 (1992) 1564.
[8] E.J. Amis, Nat. Mater. 3 (2004) 83.
[9] K. Rajan, Annu. Rev. Mater. Res. 38 (2008) 299.
[10] X.D. Xiang, Annu. Rev. Mater. Sci. 29 (1999) 149.
[11] M.W. Barsoum, M. Radovic, Annu. Rev. Mater. Res. 41 (2011) 195.
[12] M.W. Barsoum, Prog. Solid State Chem. 28 (2000) 201.
[13] Z.M. Sun, Int. Mater. Rev. 56 (2011) 143.
[14] D. Music, J.M. Schneider, JOM 59 (2007) 60.
[15] D. Music, J.M. Schneider, Appl. Phys. Lett. 89 (2006) 121914.
[16] D. Music, J.M. Schneider, Appl. Phys. Lett. 88 (2006) 031914.
[17] D. Music, Z. Sun, J.M. Schneider, Phys. Rev. B 71 (2005) 052104.
[18] R.L. Fleischer, D.M. Dimiduk, H.A. Lipsitt, Annu. Rev. Mater. Sci. 19 (1989) 231.
[19] H. Jacobs, D. Rechenbach, U. Zachwieja, J. Alloys Compd. 227 (1995) 10.

Chapter 2
Methods

2.1 Introduction

This chapter describes the experimental and theoretical methods employed in this work. First of all, the basic principle of sputter deposition is presented with a brief introduction of the combinatorial thin film approach. Sputter deposition systems used in this work were developed in-house, and their designs and functions are explained. Scanning electron microscopy, energy dispersive X-ray spectroscopy, X-ray diffraction, and nanoindentation were common characterization techniques employed to obtain the chemical, structural, and mechanical properties, and their underlying principles are presented. Information on indentation stress field analysis and a methodology for probing mechanical properties of porous samples is given. Finally, a brief introduction to ab initio calculations is presented.

2.2 Thin film synthesis: Magnetron sputtering

Sputter deposition is one of the most widely used Physical Vapor Deposition (PVD) techniques. Applications range from hard coatings on machinery tools to semiconductor microelectronics. Figure 2.1 illustrates how the sputter deposition process works. A solid material being sputtered is referred to as a "target". A "substrate" is a solid material on which a target material is deposited as a thin film. The target can be made of elements or alloys. A non-conductive target such as ceramics can also be sputtered using a RF (Radio Frequency) power supply. Both target and substrate are placed in a vacuum chamber which is evacuated down to a base pressure of 10^{-4}~10^{-6} Pa. Subsequently, a controlled amount of sputtering gas, typically inert Ar gas, is introduced to the chamber. Other gases such as N_2 and O_2 can also be added for reactive sputtering for deposition of nitrides and oxides. When a negative pole of a power supply is connected to a

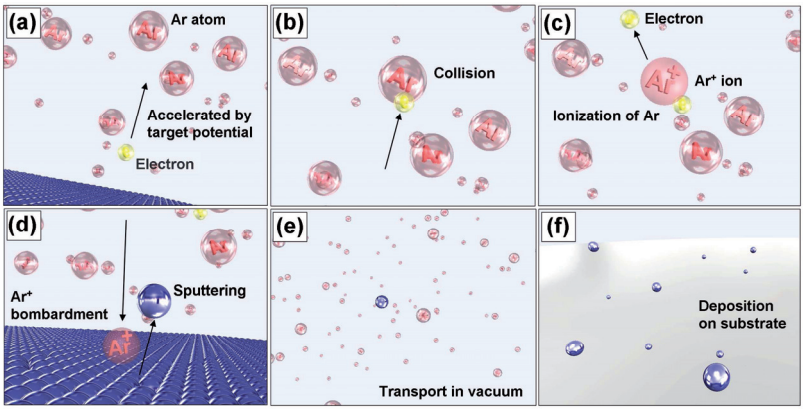

Figure 2.1 Schematic illustrations for sputter deposition process, (a) acceleration of electrons by a negative target potential, (b) collision between electron and Ar atom, (c) electron impact ionization of the Ar atom, (d) sputtering of target atoms by Ar^+ bombardment, (e) transportation of sputtered target atom, and (f) deposition on the substrate.

target, an electron being present around the target surface generated due to, e.g., photoionization of neutral species by cosmic rays and field emission, can be accelerated in vacuum by the potential field on the target (Figure 2.1(a)). This high energetic electron will collide with an Ar gas atom during traveling in vacuum (Figure 2.1(b)). If the kinetic energy of the accelerated electron is high enough, this collision causes an ejection of an electron from the Ar neutral resulting in the ionization to form an Ar^+ ion, i.e., electron impact ionization, (Figure 2.1(c)). An additional electron produced by the electron impact ionization may cause another Ar ionization so that an avalanche ionization process takes place. The Ar^+ produced in the vicinity of the target surface can be accelerated towards the target surface. The accelerated Ar^+ bombards the target surface and transfers its kinetic energy onto target atoms within a so-called collision cascade. The collision cascade affects structure evolution and may introduce point defects, dislocation loops, and stacking faults. Secondary electrons are also emitted from the target surface due to the Ar^+ ion bombardment, which is essential

for sustaining the discharge plasma. Besides these phenomena, target atoms at the surface can also be ejected into the space with a certain kinetic energy, i.e., sputtering (Figure 2.1(d)). Sputtered target atoms travel in vacuum towards a substrate facing the target surface (Figure 2.1(e)). Eventually, when sputtered target atoms reach the substrate surface, they condense on the surface and constitute a thin film (Figure 2.1(f)).

In almost all cases in practice in sputter depositions, a set of magnets is placed behind a target in such a way that a closed loop of magnetic field is formed on the target surface. An example of the magnet configuration for a disk shaped target is schematically illustrated in Figure 2.2. Due to the magnetic field, electrons accelerated by the target potential can be trapped at the vicinity of the target surface. Hence, the electron density at the target surface can be increased. Consequently, the number of electron impact ionization collisions of Ar gas increases, which enhances the sputtered flux. This type of sputtering technique is referred to as magnetron sputtering. Nowadays, the term “sputtering” implicitly means “magnetron sputtering” since diode sputtering, i.e., without magnetic field, is hardly used today in applications.

Sputter deposition is an atomistic process so that the film thickness can be very precisely controlled. From a material synthesis point of view, it is interesting that sputter deposited thin films experience rapid quenching with an extremely high cooling rate of ~10^{15} K/s [1]. Such a high cooling rate cannot be achieved with conventional bulk material synthesis routes. In other words, sputter deposition is characterized as a highly non-equilibrium material processing. This non-equilibrium feature of sputtering is

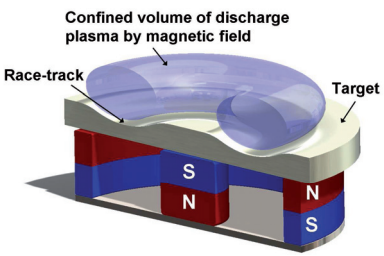

Figure 2.2 Schematic illustration of a typical magnet configuration for a disk shaped magnetron cathode.

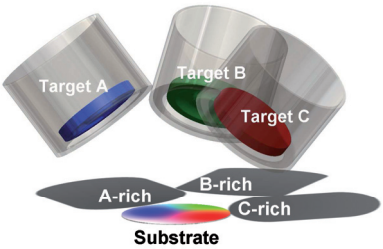

Figure 2.3 Schematic illustration for combinatorial magnetron sputter deposition to fabricate a thin film with lateral composition gradient.

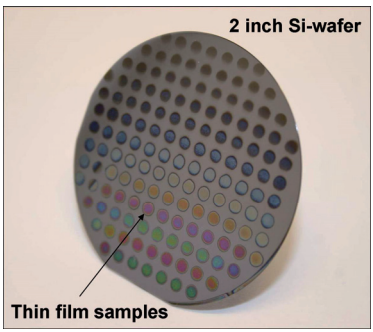

Figure 2.4 Photograph of combinatorial sample library fabricated for demonstration purpose.

very attractive for materials engineering since it provides a possibility to produce new materials which may not be realized by conventional material synthesis routes such as casting-solidification and powder metallurgy. An example is the deposition of (Ti-Al)N hard coatings employed for cutting tools [2]. The binary TiN phase crystallizes in cubic NaCl structure. The solubility limit of Al in TiN is very small at room temperature, and hence TiN and AlN (hcp, wurtzite structure) should coexist in the thermodynamic equilibrium state. However, the formation of this phase mixture is kinetically hindered in sputter deposition, and instead, the single phase metastable NaCl-type (Ti-Al)N is formed with supersaturated Al up to ~60 mol.% AlN [3]. It is known that the addition of Al in TiN improves the wear performance as well as oxidation resistance [2].

Sputter deposition is also a powerful tool for the so-called combinatorial materials science [4-6]. The basic idea behind this newly evolving field of materials science is to probe hundreds of combinations of material systems and processing conditions with a minimum experimental effort and time investment. The recent development of spatially resolved material characterization techniques such as micro-beam X-ray diffraction

and nanoindentation is essential for combinatorial materials science. Co-sputter deposition can be used to fabricate thin film materials with lateral compositional gradients by applying an appropriate geometrical configuration of individual cathodes as schematically illustrated in Figure 2.3. The sample produced contains a combinatorial sample library. Figure 2.4 demonstrates an example of a combinatorial sample library prepared on a 2 inch Si wafer. Isolated pads of films were created by using a mask on the wafer. (Note that the sample shown in Figure 2.4 was fabricated only for demonstration purpose. An elemental boron target was sputtered using a RF power supply with the deposition incident angle of 45° so that continuous thickness variation was created. Hence, the color variation appeared in the film is not due to any chemical composition effects in the film, but due to optical effects arising from the difference in thickness of the deposited boron (or boron oxide) thin film.) With suitable spatially resolved characterization techniques applied on these combinatorial thin film samples, high-throughput screening of the composition, structure, and property relationship can be realized.

2.3 Development of sputter deposition systems

2.3.1 UHV combinatorial magnetron sputtering system

A combinatorial sputter deposition chamber was designed and built in-house. An overview of the system setup including in-situ film analytical devices is schematically shown in Figure 2.5. To insure a sufficiently low base pressure in the main deposition chamber, the system is equipped with a load lock substrate transfer system. Both the main deposition and load lock chambers are evacuated using turbomolecular pumps (Varian, Inc.) backed with dry scroll pumps (Varian, Inc.). The base pressure of ~10^{-8} Torr can ordinarily be achieved, and lower base pressure is possible after the chamber is baked. The standard substrate size which can be loaded on a substrate manipulator (Bestec, GmbH) is a 2 inch wafer. The substrate can

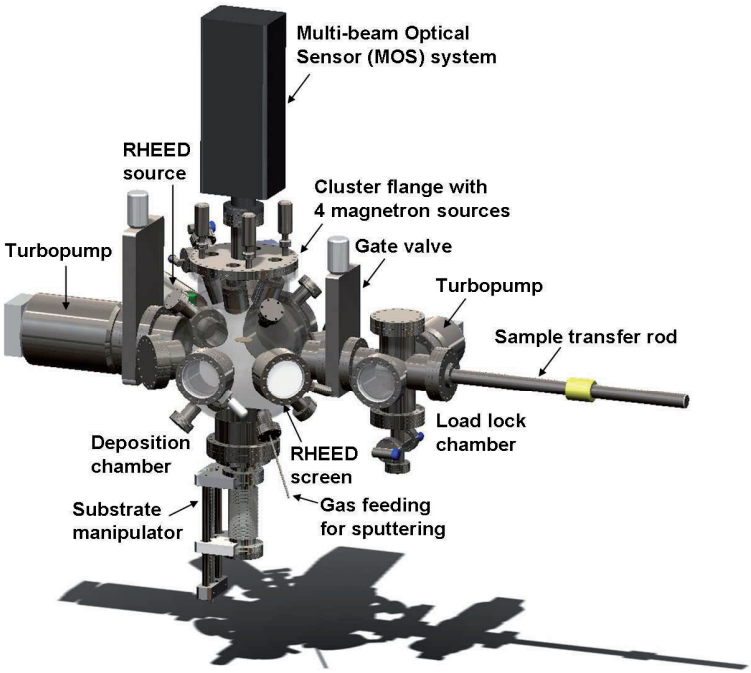

Figure 2.5 Schematic illustration for the basic setup of the combinatorial sputter deposition system built in-house including RHEED and MOS systems for in-situ film analysis.

be heated up to 1273 K by a BN-ceramic heater, be rotated, and be electrically biased. A cluster flange equipped with four 2 inch magnetron sources (Gencoa, Ltd.) as shown in Figure 2.6 can be fixed on the top. Both DC and RF power supplies are applicable for the cathodes. Ar gas for sputtering is introduced to the deposition chamber through mass flow controllers (MKS Instruments, GmbH). N_2 and O_2 gases can additionally be supplied for reactive sputter deposition. In addition to this standard deposition setup, the chamber can be equipped with in-situ thin film analytical devices such as a Reflection High Energy Electron Diffraction (RHEED, STAIB Instruments, GmbH) apparatus and Multi-beam Optical stress Sensor system (MOS, k-Space Associates, Inc.). In the following two

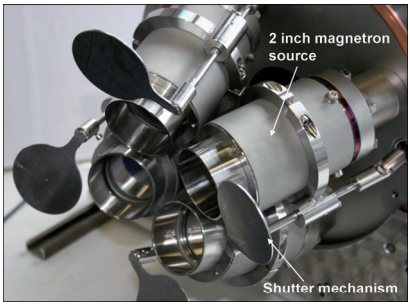

Figure 2.6 Photograph of a cluster flange equipped with four 2 inch magnetron sources with shutter mechanism installed.

sections the basic theoretical background is described briefly. Selected examples of applications of RHEED and the MOS system are given.

Reflection High Energy Electron Diffraction (RHEED) is a powerful analytical tool to study the surface crystallography in epitaxial or single crystalline thin films. The information about the surface-phase and the reconstructed two-dimensional surface structure can be obtained by in-situ even during the film growth process. A period of RHEED intensity oscillation during layer by layer deposition such as molecular beam epitaxy (MBE) is known to be equal to the monolayer deposition time [7], which provides an opportunity to make a real time monitoring of the growth mode in MBE. Hence, most MBE systems are nowadays equipped with RHEED devices.

Although epitaxial or single crystalline thin films are most suitable for RHEED analysis, it has been applied to polycrystalline thin films. It has been demonstrated that quantitative information regarding film texture can directly be determined through RHEED pattern analysis [8-10]. Furthermore, the crystallinity (amorphous or crystalline) of an as-deposited film can be analyzed in-situ. Similarly, the direct phase identification from a RHEED pattern may also be possible.

A RHEED pattern obtained from a polycrystalline thin film is due to diffraction of the incident electron beam by many different crystallites. It is not a reflection mode operated as in two-dimensional surface structure analysis, but essentially a three-dimensional transmission diffraction mode as schematically shown in Figure 2.7. Hence, the kinematic theory of

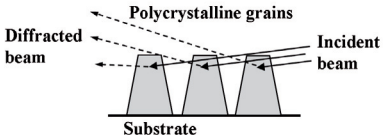

Figure 2.7 Schematic illustration showing a transmission diffraction mode in RHEED on a polycrystalline thin film.

diffraction in this case is quite similar to that for a selected area electron diffraction (SAED) technique commonly used in transmission electron microscopy (TEM). Based on the Ewald diffraction theory, the diffraction condition is formulated by

$$\boldsymbol{K'}-\boldsymbol{K}=\boldsymbol{G}, \tag{2.1}$$

where ***K'*** and ***K*** are the diffracted and the incident wave vectors of the electron beam, and ***G*** is the reciprocal lattice vector, respectively. The Ewald sphere can be approximated by a plane since $G << K$ for typical electron diffraction conditions. Hence, the RHEED pattern is essentially the intersection of the Ewald plane with the reciprocal lattice, which is defined mathematically by

$$\boldsymbol{K}\cdot\boldsymbol{G}=0. \tag{2.2}$$

Figures 2.8 demonstrates an example of RHEED pattern analysis for a compositionally spread Fe-Mn binary thin film deposited on a 2 inch Si(100) wafer without substrate heating. The chemical compositions were measured to be from 14 to 32 at.% Mn with 22 at.% Mn at the center on the substrate, from which the RHEED pattern was supposed to be obtained. Diffraction rings are clearly detected (Figure 2.8(a)), which evidences the formation of crystalline phase even without substrate heating. Based on the measurement of relative *d*-spacing for each diffraction planes, the film structure can be identified as the body centered cubic (BCC) structure. Moreover, the diffraction rings are seen to be discontinuous, which indicates that the film is strongly textured. Figures 2.8(b), (c), and (d) give simulated diffraction patterns assuming (001), (111), and (011) fiber textures with the orientation spread of the texture axis, $\Delta\phi$, of 10°, respectively. The simulated patterns were plotted by a program written by

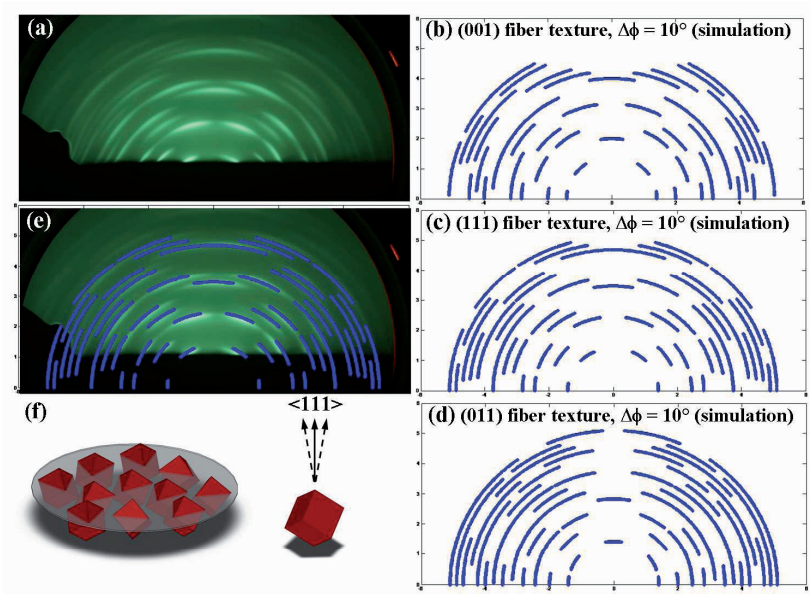

Figure 2.8 RHEED analysis for combinatorially deposited Fe-Mn thin film with composition spread from 14 to 32 at.%Mn. (a) RHEED pattern measured at 30 kV acceleration voltage. Simulated RHEED patterns for BCC structure assuming (b) (001) fiber texture with 10° texture axis distribution, (c) (111) fiber texture with 10° texture axis distribution, and (d) (011) fiber texture with 10° texture axis distribution. Experimental pattern is in good agreement with simulated pattern for (111) fiber texture (e). (f) Schematic illustration showing grain orientation of (111) fiber textured film.

MATLAB™ software. The basic formalism for RHEED pattern simulation in polycrystalline films can be found elsewhere [8-10]. Among these three simulated patterns, one for the (111) fiber texture is in good agreement with the experimental pattern (Figure 2.8(e)), and hence the film deposited can be characterized as the (111) fiber texture with the texture axis spread of 10° as schematically shown in Figure 2.8(f). In short, the application of RHEED on an as-deposited film provides the fruitful information about the crystallographic structure of the film. This will facilitate the optimization of deposition parameters to grow a film with the desired phase and structure.

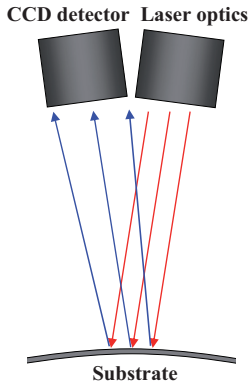

Figure 2.9 Schematic illustration of Multi-beam Optical Sensor system (MOS, kSA) for film stress measurement. The figure is produced by referring to an application note written by E. Chason for k-Space Associates Inc., USA.

In addition to the RHEED apparatus, the deposition chamber is equipped with a film residual stress measurement device. In thin film technologies, irrespective of a field of application such as hard coatings, microelectronics, optical coatings, control of residual stress in thin films is a common topic of interest. This is simply because of the fact that the residual stress affects the mechanical and functional properties of thin films. Furthermore, the lifetime of thin film-substrate system can also be varied depending on residual stresses. Depending on the stress magnitude, cohesive or adhesive failures may be observed.

Film residual stress can be classified into extrinsic and intrinsic stresses. For instance, thermal stress developed due to a mismatch of thermal expansion coefficient between the film and substrate is an example of extrinsic residual stress. Thermal residual stress at a given change in temperature can be estimated relatively easily if the values of thermal expansion coefficient and elastic modulus for the film and substrate are available. On the other hand, intrinsic stress in the film is in general very difficult to predict since it is directly linked to the film microstructure evolution, and hence is dependent on many different deposition parameters. In sputter depositions, the intrinsic film stress can be affected by, for example, the sputtering gas pressure, deposition rate, angle of deposition incidence [11]. Also, Ar ion bombardment on a growing film by applying a

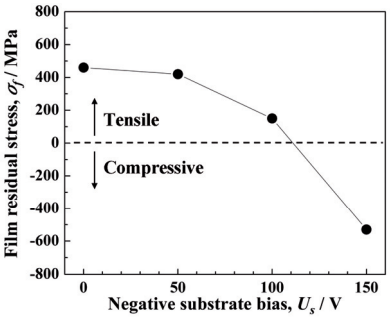

Figure 2.10 Residual stress evolution in Ti thin films as a function of substrate bias voltage.

negative substrate bias voltage induces compressive stress due to atomic peening effects [12].

When a film is stressed, curvature in the substrate is induced due to elastic deformation. Based on the Stoney equation [13], the change in curvature, $\Delta\kappa$, is related to the film stress, σ_f, by

$$\Delta\kappa = \frac{6\sigma_f h_f}{M h_s^2} \qquad (2.3)$$

where h_f is the film thickness, M is the biaxial elastic modulus of the substrate, and h_s is the substrate thicknesses. This equation allows to determine the film stress by the measurement of the change in curvature in the substrate before and after the film deposition. The curvature-change can precisely be measured in a non-destructive manner using a laser optical technique. The Multi-beam Optical Sensor (MOS, kSA) system [14] contains an array of parallel laser beams that strike the substrate and are reflected back towards a CCD detector to monitor the relative change in positions of laser spots after or even during depositions in real time. The curvature in the substrate can be determined with the given distance from the substrate to the CCD detector. A schematic illustration of the set-up of the MOS system is shown in Figure 2.9.

Figure 2.10 gives an example of the film stress measurements obtained using the MOS system equipped in the deposition chamber. Ti thin films were sputter deposited on 2 inch Si(100) substrates at room temperature with different substrate bias voltages. Only one of four magnetron cathodes was operated. A Ti target (ϕ50 mm) was sputtered with the Ar pressure of 3 mTorr at the DC power of 120 W for 120 min. The target to substrate distance was approximately 10 cm. The substrate was

rotated during deposition to ensure a uniform film thickness distribution. The resulting film thicknesses were measured to be in the range of 1.1–1.2 μm. It can be seen that the film residual stress changes from tensile for the grounded substrate into compressive as the substrate bias voltage is increased. The increase in compressive stress with substrate bias voltage can be understood by the increased ion bombardment of the growing Ti films, and hence by atomic peening effects. The evolution of intrinsic tensile stresses may be explained by a constrained volume shrinkage during the film growth associated with the grain boundary coalescence and/or the rearrangement of disordered constituent atoms [11].

2.3.2 Small magnetron sputtering systems

A research combinatorial sputter deposition system was also designed and built in-house. A schematic illustration of the system is shown in Figure 2.11.

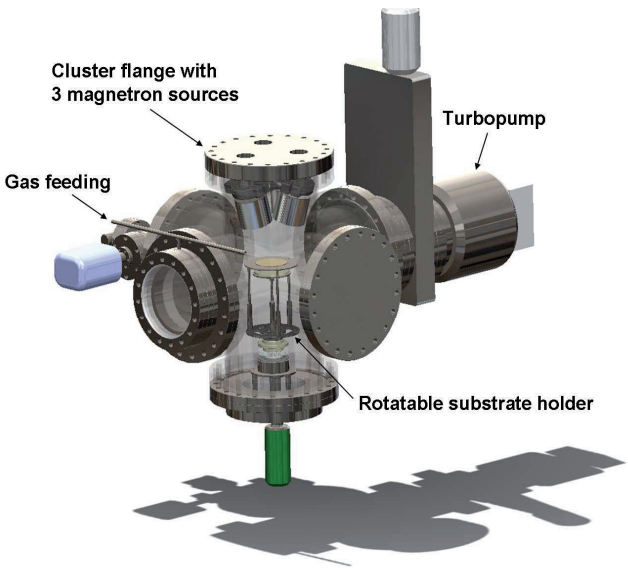

Figure 2.11 Schematic illustration of the combinatorial sputter deposition system built in-house equipped with three magnetron sources.

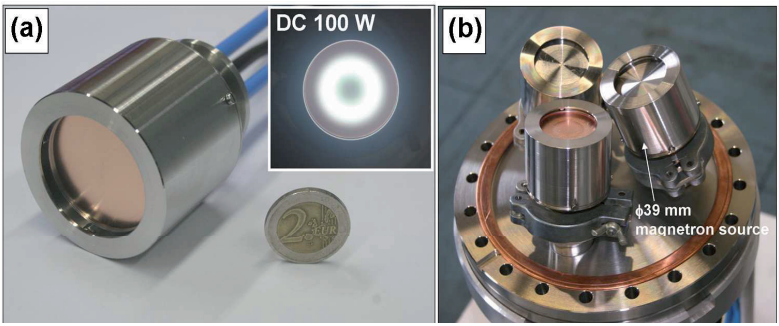

Figure 2.12 Photographs for (a) magnetron source for ϕ39 mm target and (b) cluster flange equipped with three magnetron sources. Both components are built in-house. The inset in figure(a) shows the discharge plasma on a Cu target sputtered in 5 mTorr Ar at a DC power of 100 W.

Small magnetron cathodes for the target size of 39 mm in diameter and 3 mm in thickness (see Figure 2.12(a)) as well as a cluster flange for three magnetron cathodes (see Figure 2.12(b)) were also manufactured in-house. A set of magnets placed behind a Cu plate is in contact directly with cooling water to avoid possible demagnetization of the magnets due to overheating of the target. Hence, the maximum input power which can be delivered to the cathode should be determined by the target conditions, e.g. melting point, thermal conductivity, thermal shock resistance. A main chamber is evacuated with a turbomolecular pump backed with an oil rotary vane pump. The base pressure of ~10^{-4} Pa can be achieved. The substrate holder (built in-house) is equipped optionally with an in-vacuum rotation system so that a homogeneous film in terms of the thickness and composition can be deposited if

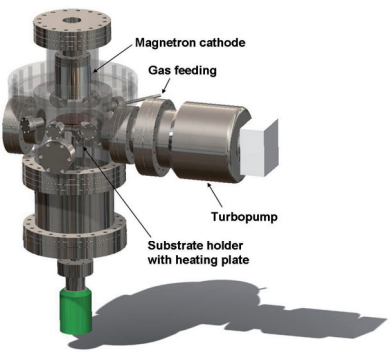

Figure 2.13 Schematic illustration for sputter deposition system built in-house equipped with a single magnetron source.

necessary. A 2 inch wafer can be placed on the holder in a standard setup. Ar and N_2 gas feeding lines controlled individually with mass flow controllers are connected to the deposition chamber for sputtering.

A simple sputter deposition system for a single magnetron source was also built in-house. A magnetron cathode with a target size of 50 mm in diameter and a substrate holder equipped with a heating plate were manufactured in-house as well. Figure 2.13 shows a schematic illustration for a basic setup of the system. The deposition chamber is evacuated by a turbomolecular pump backed with a rotary vane pump. The base pressure of the system is 5×10^{-4} Pa. A 2 inch wafer can be placed on the holder with a Cu heating plate for heating substrate. The Cu plate can be heated up to 673 K by a resistance heating wire fixed behind the plate. Both Ar and N_2 gas lines with mass flow controllers are connected to the chamber.

2.4 Characterization

2.4.1 Scanning Electron Microscopy (SEM) and Energy Dispersive X-ray (EDX) analysis

SEM is nowadays one of the most common microscopy tools for materials research in a variety of fields such as for organic biomaterials, microelectronic devices, and structural steels, just to name a few. The principle for imaging in SEM is essentially different from an optical microscope in that a SEM image is constructed based on the detection of signals emitted from a sample surface due to the irradiation by a focused high energy electron beam. When a sample surface is irradiated by a high energy electron beam with a typical acceleration voltage between 5 and 30 kV in SEM, signals such as secondary electrons (SE), back-scattered electrons (BSE), Auger electrons, and characteristic X-rays can be created by the interaction between the incident electron beam and atoms in the sample (Figure 2.14). For imaging purpose, the detection of secondary electrons is most widely used. Since a secondary electron detector is fixed

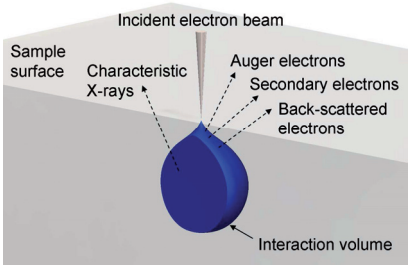

Figure 2.14 Schematic illustration showing signals emitted from sample surface by the interaction between high energy electron beam and sample matter.

in a certain position and angle with respect to the irradiated location, the number of secondary electrons which can be detected is highly dependent on the surface topography of the sample. In other words, the intensity of secondary electrons detected provides the information about the surface topographical feature at the irradiated location. In SEM, as the term "scanning" indicates, an electron beam with a given acceleration voltage scans over an observation area, and the secondary electron intensity for each location irradiated can be detected. A SEM image (secondary electron image) is a contrast image of secondary electrons detected, which can eventually reproduce the surface topographical feature of the observation area. Besides the SE, BSE can also be used for microscopic imaging. The intensity of BSE is highly sensitive to the atomic number of irradiated samples. Therefore, a BSE contrast image is very useful to reveal, for example, the microstructural inhomogeneity consisting of phases with different chemical compositions.

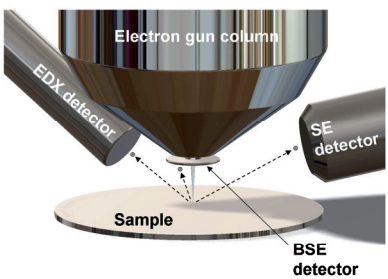

Figure 2.15 Schematic illustration for setup of SEM-EDX equipment.

Characteristic X-rays emitted due to the electron beam irradiation is used to analyze the chemical composition of a sample. The high energy electron beam can eject inner shell electrons from atomic nuclei. The vacant electron sites created can be filled by outer shell electrons, which leads to the

emission of characteristic X-rays as a way to release the energy to surrounding. Since the energy levels (wavelength) of characteristic X-rays are definitely atom-specific, atoms being present in the sample can be identified by measuring the energy of characteristic X-rays, i.e., energy dispersive X-ray spectroscopy. The chemical composition quantification for a multielement system is also possible by analyzing the intensity of each characteristic X-ray in the spectrum measured.

The microstructural features and chemical compositions of the samples in the present work were studied in most cases using SEM (JEOL JSM-6480) equipped with EDX (EDAX Genesis 2000). The system setup is schematically shown in Figure 2.15. The SEM was also used to measure the thickness of the deposited thin films. A tungsten filament was employed. The acceleration voltage of electron beam was selected to between 5 and 30 kV depending on the samples and the EDX measurement conditions. A standard ZAF method was employed for quantification of chemical composition in the EDX. For each EDX measurement, the depth of interaction volume was smaller than the thicknesses of deposited thin films in order to avoid the influence of substrate, and hence to ensure the use of the ZAF method. The interaction volume size was estimated by a Monte Carlo simulation using the Casino software [15-17].

2.4.2 X-ray diffraction (XRD)

A crystalline material is composed of a periodic arrangement of atoms. The physical properties of a material cannot be determined solely by its chemistry, but highly depend on its crystallographic structure. For instance, both diamond and graphite are composed of elemental carbon. Diamond is known to be one of the hardest materials while graphite is very easily shearable and machinable, and hence used often as a solid lubrication material. This large difference in properties is caused simply by the difference in crystallographic structures between diamond and graphite. In

order to understand the behavior of a material, the information about the crystallographic structure is indispensable.

The most common technique in materials research for the determination of the crystallographic structure is X-ray diffraction. When a sample is irradiated by an X-ray beam with a particular wavelength, the X-rays are scattered by electrons in atoms consisting of the sample, and can be emitted in all the directions with the wavelength of the incident X-ray, i.e., elastic scattering. The wavelength of X-ray commonly used for structural analysis is comparable to a length scale of atomic distances in the solid. In other words, a periodic arrangement of atoms, more precisely of electron density, in the solid acts as a diffraction grid for X-rays. Hence, the constructive interference of scattered X-rays occurs in particular angular directions, i.e., diffraction (Figure 2.16). When the sample studied is composed of powders or polycrystals with random grain orientation, the diffracted beams from many crystallites assume a cone shape. The angular feature of diffracted X-ray, which is commonly represented in terms of diffraction angle, 2θ, contains the information about the spatial distribution of electron density and hence of the real space position of atoms in a crystal.

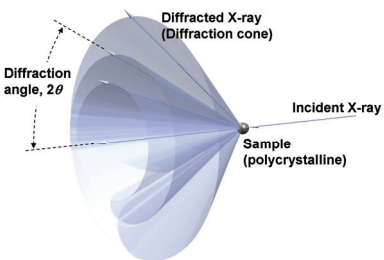

Figure 2.16 Schematic illustration for X-ray diffraction showing the geometrical relationship between incident and diffracted X-rays performed on a powder or polycrystalline sample.

The diffraction condition from a material having a certain crystallographic structure can be described based on the Ewald sphere construction [18]. A schematic example is shown in Figure 2.17(a). The incident wave vector, ***K***, with its scalar magnitude of $1/\lambda$ represents the radius of the sphere, where λ is the wavelength of

the incident beam. Similarly, the scattered wave vector, ***K'***, is also defined with the magnitude of $1/\lambda$. The reciprocal lattice vector of the structure, $\boldsymbol{G_{hkl}}$, is placed with its origin at the tip of ***K***. The magnitude of $\boldsymbol{G_{hkl}}$ is given by the reciprocal value of interplanner d_{hkl}-spacing, $1/d_{hkl}$. The diffraction can occur when the scattering vector, ***K'*** - ***K***, corresponds to a reciprocal point, $\boldsymbol{G_{hkl}}$. Namely,

$$\boldsymbol{K'} - \boldsymbol{K} = \boldsymbol{G_{hkl}} . \tag{2.4}$$

In the example illustrated in the figure, $\boldsymbol{G_{111}}$ and its equivalent points are located on the Ewald sphere surface, and hence satisfy the diffraction condition above. The scattering or diffraction angle between ***K*** and ***K'*** is given by 2θ as schematically represented by Figure 2.17(b). Based on the consideration of diffraction geometry, the diffraction condition in equation (2.4) can then be reformulated by

$$\frac{2}{\lambda}\sin\theta = \frac{1}{d_{hkl}} . \tag{2.5}$$

This is equivalent to the well-known Bragg's law for diffraction, namely,

$$\lambda = 2d_{hkl}\sin\theta . \tag{2.6}$$

For a given crystallographic structure, not all the set of *hkl* planes contribute

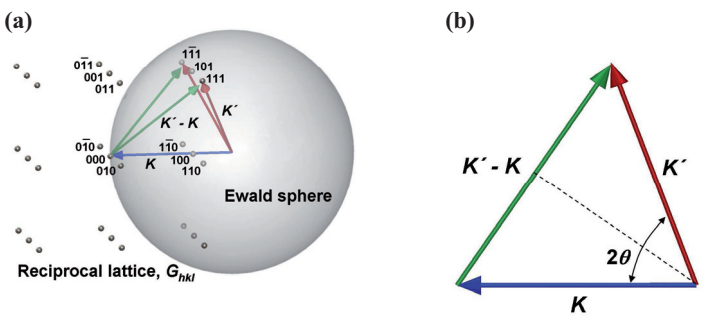

Figure 2.17 (a) Schematic illustrations for Ewald sphere construction for diffraction condition. (b) Geometrical relationship between incident and diffracted X-rays.

to the diffraction. The possible diffraction planes can be provided in terms of its structure factor, and hence be uniquely defined for each crystallographic structure. X-ray diffraction is used not only for the crystallographic structure identification, but also for evaluating other microstructural parameters including, for instance, dislocation density, grain size, orientation distribution of grains, i.e., texture, and residual stress.

For the present work, two diffractometers were employed for different samples and purposes. One was Siemens D5000 equipped with a Cu-K_α source and a goniometer with a standard scintillation counter. The other was Bruker D8 Advance diffractometer equipped with a collimated X-ray (Cu-K_α) beam and an areal detector enabling the fast collection of XRD patterns. For all measurements, a collimator size of 0.5 mm in diameter was used. In both diffractometers, the measurements were performed at voltage and current settings of 40 kV and 40 mA, respectively.

2.4.3 Nanoindentation

2.4.3.1 Basic theoretical background

Nanoindentation becomes nowadays a common tool for studying the elastic and plastic properties of materials. As the term “nanoindentation” implies, this technique enables us to probe the mechanical properties from an extremely small volume with the indentation penetration depth of, for instance, only less than 100 nm. The corresponding lateral size of the indentation can be less than 1 μm, which is even smaller than a grain size of typical polycrystalline metals and ceramics. This provides an opportunity to directly measure the mechanical properties of a single grain from a polycrystalline material or of an individual phase in a multiphase material. Because of its extremely small probed volume, nanoindentation is also suitable for the mechanical property characterization of thin films without the influence of substrate effect.

The basic principle of nanoindentation is found in the pioneering study by Oliver and Pharr [19] and in others [20-23]. Nanoindentation is essentially different from a conventional indentation method such as the Vickers hardness test in that the size of the indentation impression can indirectly be quantified from the precise measurement of indentation depth and the exact indenter tip geometry. The projected contact area of indentation, A_c, as a function of contact depth, h_c, is given by defining the so-called tip area function. For an ideal Berkovich indenter tip, the tip area function is calculated to be

$$A_c = 24.5 h_c^{\,2}. \tag{2.7}$$

The indentation load, P, and depth displacement, h, are recorded continuously during indentation loading and unloading. The actual contact depth, h_c, at the maximum penetration depth, h_{max}, is determined to be

$$h_c = h_{max} - \varepsilon \frac{P_{max}}{S}, \tag{2.8}$$

where ε is the geometric constant and S is the contact stiffness defined as the first derivative dP/dh at h_{max} measured for an unloading curve fitted by a power law function as

$$P = A(h - h_f)^m, \tag{2.9}$$

where A, h_f, and m are the fitting parameters. The measurements of h_{max}, P_{max}, and S allow us to determine the corresponding contact depth, h_c, and hence the contact area, A_c using a given tip area function. The elastic modulus (reduced modulus, E_r) can then be calculated from the equation

$$E_r = \frac{\sqrt{\pi}}{2} \frac{S}{\sqrt{A_c}}, \tag{2.10}$$

and

$$\frac{1}{E_r} = \frac{(1-\nu^2)}{E} + \frac{(1-\nu_i^{\,2})}{E_i}. \tag{2.11}$$

E and ν are the elastic modulus and Poisson's ratio of the sample while E_i and ν_i are those of the indenter tip. Similar to other indentation tests, the hardness, H, can be defined as

$$H = \frac{P_{max}}{A_c}. \tag{2.12}$$

A schematic representation of indentation and a load-displacement curve are illustrated in Figure 2.18.

As can be seen in the equations above, the precise determination of the contact area, A_c, is of great importance to measure the correct elastic modulus, E, and hardness, H, in nanoindentation. The ideal tip area function for the Berkovich indenter geometry as given by equation (2.7) is not valid in practice especially when the penetration depth is smaller than a few hundred nanometers. This is simply because of the fact that a real indenter tip is not perfectly sharp, but is rounded to some extent, and hence deviates from the ideal tip area function. Therefore, the real tip area function for an indenter tip used has to be experimentally determined prior to the indentation measurements for samples. In order to account for a deviation from the ideal tip area function, the real tip area function is commonly described by a polynomial function like

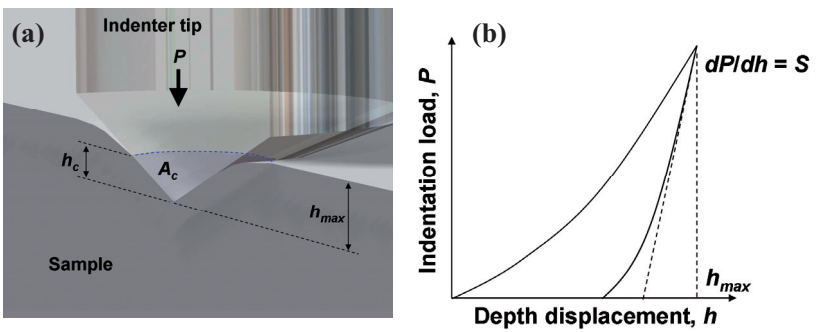

Figure 2.18 Schematic representation of nanoindentation (a) and load-displacement curve (b).

$$A_c = C_0 h_c^{\,2} + C_1 h_c + C_2 h_c^{\frac{1}{2}} + C_3 h_c^{\frac{1}{4}} + C_4 h_c^{\frac{1}{8}} + C_5 h_c^{\frac{1}{16}}. \qquad (2.13)$$

The parameters C_0, C_1, C_2, C_3, C_4, and C_5 can be determined from a set of experimental data with different penetration depths measured from a standard sample, e.g,. fused silica, with the known elastic modulus.

As-measured data in nanoindentation contains the non-negligible elastic displacements of machine components such as the indenter shaft, the indenter tip, and the sample mounting stage. These machine-related displacements need to be subtracted from as-measured load-displacement data prior to calculating the E_r and H. This correction can be done by defining the so-called load frame compliance or machine compliance, C_m:

$$h = h_t - PC_m, \qquad (2.14)$$

where h_t is the as-measured displacement. The value of C_m depends on the nanoindentation machine employed, and therefore has to be experimentally determined. Equation (2.14) can be reformulated using the definition of contact stiffness into

$$\frac{1}{S} = \frac{1}{S_t} - C_m, \qquad (2.15)$$

where S_t is the as-measured contact stiffness. The combination of equations (2.10), (2.12), and (2.15) leads to

$$\frac{1}{S_t} = \left(\frac{\sqrt{\pi}}{2}\frac{\sqrt{H}}{E_r}\right)\frac{1}{\sqrt{P_{max}}} + C_m. \qquad (2.16)$$

When the E_r and H are assumed to be independent of the indentation loads applied, a linear relationship should be established between the inverse of S_t and the inverse of square root of P_{max}. Indentations with varied peak loads performed on a standard sample such as fused silica provide a linear plot according to equation (2.16). The intercept corresponds to C_m, machine compliance. Because of its simplicity, this method is widely used for the determination of C_m in practice.

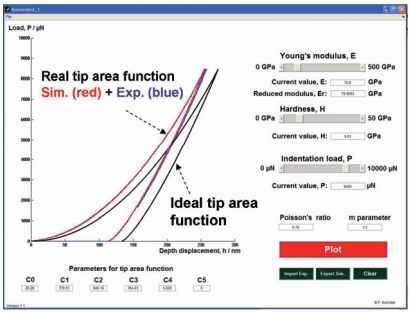

Figure 2.19 Screen shot of the graphical user interface program developed for load-displacement curve simulation.

In this work, the nanoindentation measurements were performed using a Hysitron TriboIndenter. A Berkovich diamond indenter tip (E_i = 1140 GPa and ν_i = 0.07) was used for all the measurements. The tip area function was determined using fused silica. The machine compliance of the system was also calibrated using fused silica. A sample to be investigated was glued on a steel plate, and then the steel plate was fixed on the magnetic sample stage. The data analysis was carried out using the standard Oliver-Pharr method.

To assess the nanoindentation data measured, a graphical user interface program was also developed in-house using MATLAB^{TM} environment. A screen shot of the program is presented in Figure 2.19. The program simulates the load-displacement curve for given input sample parameters (elastic modulus, hardness, Poisson's ratio), an indentation load, and a geometry dependent exponent, *m*. The program enables to simulate the load-displacement curves both for the ideal tip area function and for the real tip area function determined experimentally. The simulation program is based on the basic formalism described in ref. [23]. Furthermore, the measured data can be imported to the plot so that the experimental and simulated results are directly compared. The figure shows an example of the data from nanoindentation on fused silica. As can be seen, the simulated load-displacement curve with a real tip area function is in very good agreement with the experimental one. On the other hand, the simulated curve with the ideal tip area function overestimates the total

penetration depth due to the assumption of the perfectly sharp indenter tip geometry.

2.4.3.2 Indentation stress field analysis by Hertz contact theory

The tip radius of a newly manufactured Berkovich indenter is typically ~50 nm. As the number of indentation increases, the indenter tip becomes blunt due to deformation and wear, and hence the tip radius increases further. The indenter tip is therefore assumed to be spherical in shape at the initial contact with the sample surface.

According to the Hertz elastic contact theory, the relationship between the indentation load, P, and the penetration depth, h, in elastic contact for spherical indentation is given by [24]

$$P = \frac{4}{3} E_r R^{1/2} h^{3/2}, \tag{2.17}$$

where E_r is the reduced modulus, and R is the tip radius, respectively. Figure 2.20 shows an example of load-displacement curves measured on fused silica with a blunt Berkovich indenter tip. The load-displacement curve is fully reversible with an indentation load up to 300 μN. This indicates that the only elastic deformation takes place up to this load, and therefore the load-displacement curve can be described by the Hertz elastic contact theory. Since the reduced modulus of fused silica is known, curve fitting based on equation (2.17) enables to determine the tip radius indirectly. Consequently, a mean tip radius of 760 ± 70 nm was obtained from 10 measurements for this particular blunt Berkovich tip.

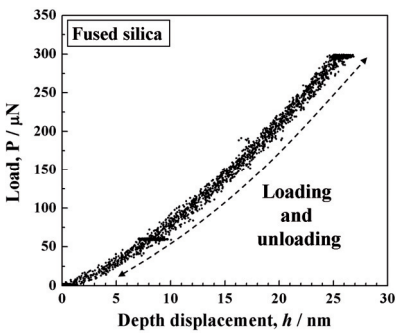

Figure 2.20 Load-displacement curve measured on fused silica using a blunt Berkovich indenter tip. The loading and unloading curves are reversible up to an indentation load of 300 μN.

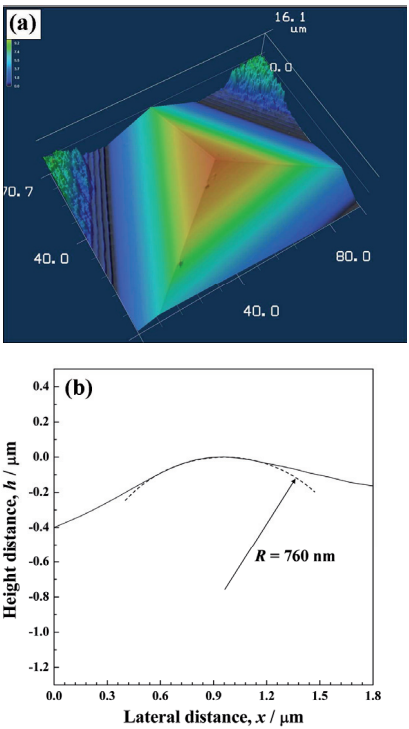

Figure 2.21 3D laser microscope image of a blunt Berkovich indenter tip: (a) 3D height image and (b) line profile at the tip.

In order to test the tip radius measurement above, the same tip was analyzed topographically by a 3D laser microscope (KEYENCE, VK-9710) as illustrated in Figure 2.21. Noise filtering and subsequent smoothing of the image data were performed before analysis of the shape of the tip. Figure 2.21(b) present a line profile measured at a location of the tip. It is seen that the profile can be fitted by a circle with the radius of 760 nm. This is consistent with the result obtained from the data fitting based on the Hertz contact theory as described above.

The elastic stress field within the sample during spherical indentation can be calculated in an analytic form without employing sophisticated numerical simulation such as the finite element method. In the cylindrical coordinate system (r, θ, z), the components of the stress tensor are [25]:

$$\sigma_r = \frac{3}{2}P_m\left\{\frac{1-2\nu}{3}\frac{a^2}{r^2}\left[1-\left(\frac{z}{u^{0.5}}\right)^3\right]+\left(\frac{z}{u^{0.5}}\right)^3\frac{a^2u}{u^2+a^2z^2}\right.$$

$$\left.+\frac{z}{u^{0.5}}\left[u\frac{1-\nu}{a^2+u}+(1+\nu)\frac{u^{0.5}}{a}\tan^{-1}\left(\frac{a}{u^{0.5}}\right)-2\right]\right\}, \qquad (2.18)$$

$$\sigma_\theta = -\frac{3}{2}P_m\left\{\frac{1-2\nu}{3}\frac{a^2}{r^2}\left[1-\left(\frac{z}{u^{0.5}}\right)^3\right] + \frac{z}{u^{0.5}}\left[2\nu + u\frac{1-\nu}{a^2+u} - (1+\nu)\frac{u^{0.5}}{a}\tan^{-1}\left(\frac{a}{u^{0.5}}\right)\right]\right\}, \quad (2.19)$$

$$\sigma_z = -\frac{3}{2}P_m\left(\frac{z}{u^{0.5}}\right)^3\left(\frac{a^2u}{u^2+a^2z^2}\right), \quad (2.20)$$

$$\tau_{rz} = -\frac{3}{2}P_m\left(\frac{rz^2}{u^2+a^2z^2}\right)\left(\frac{a^2u^{0.5}}{a^2+u}\right), \quad (2.21)$$

where

$$u = \frac{1}{2}\left\{\left(r^2+z^2-a^2\right)+\left[\left(r^2+z^2-a^2\right)^2+4a^2z^2\right]^{0.5}\right\}, \quad (2.22)$$

and P_m is the mean contact pressure calculated to be

$$P_m = \left(\frac{16}{9}\frac{PE_r^{\,2}}{\pi^3R^2}\right)^{\frac{1}{3}}. \quad (2.23)$$

Then, the three principal stresses, σ_1, σ_2, and σ_3 are given by

$$\sigma_1 = \frac{\sigma_r+\sigma_z}{2}+\left[\left(\frac{\sigma_r-\sigma_z}{2}\right)^2+\tau_{rz}^{\,2}\right]^{0.5}, \quad (2.24)$$

$$\sigma_2 = \sigma_\theta, \quad (2.25)$$

$$\sigma_3 = \frac{\sigma_r+\sigma_z}{2}-\left[\left(\frac{\sigma_r-\sigma_z}{2}\right)^2+\tau_{rz}^{\,2}\right]^{0.5}. \quad (2.26)$$

A local maximum shear stress, τ_{max}, at a given position within the sample is calculated to be

$$\tau_{max} = \frac{\sigma_1-\sigma_3}{2}, \quad (2.27)$$

and the hydrostatic pressure component, σ_H, is obtained as

$$\sigma_H = \frac{1}{3}(\sigma_1+\sigma_2+\sigma_3). \quad (2.28)$$

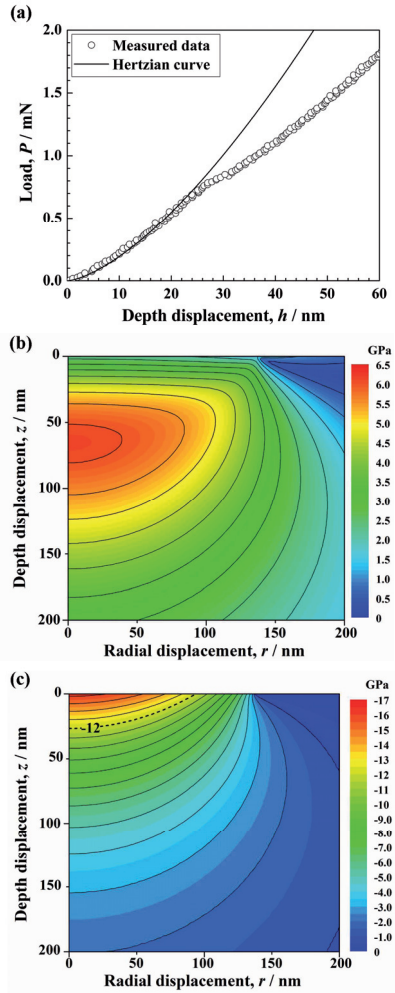

Figure 2.22 Stress field analysis for nanoindentation on Si(100) wafer measured by a blunt Berkovich indenter tip. (a) Measured data and calculated Hertzian curve. Deviation from Hertzian curve is observed at a critical load of about 770 μN. (b) Calculated local maximum shear stress, and (c) hydrostatic pressure distributions at the critical load.

Figure 2.22 demonstrates the stress field analysis from the experimental data measured on a Si(100) wafer using a blunt Berkovich indenter tip with the tip radius of ~760 nm. The initial stage of the loading curve is presented in Figure 2.22(a). For comparison, the figure also contains the theoretical Hertzian curve calculated based on equation (2.17) with the measured reduced modulus of Si(100) from the unloading curve. The initial stage of the deformation behavior is consistent with the Hertz contact theory, indicating that the deformation is purely elastic in this region. In this measurement, a deviation from the Hertzian curve occurs clearly at a critical load of about 770 μN, at which the transition from elastic to elastoplastic deformation is expected. In particular for Si, the pressure induced phase transformation from the diamond cubic structure to the metallic β-tin structure is also considered [26, 27]. The mean contact pressure at the transition point is calculated to be 12.9 GPa

which is reasonably close to a value of 11.8 ± 0.6 GPa reported previously for the onset of deformation during spherical indentation on Si(100) [26]. The stress field distribution within the sample at the transition point can also be analyzed based on the stress tensor calculation introduced above. A Poisson's ratio of 0.27 for Si is used for the calculations. Figures 2.22(b) illustrates the calculated distributions of the local maximum shear stress, τ_{max}, at the critical load of the transition point. The maximum shear stress evolved at the onset of plastic deformation and/or phase transformation amounts to 6.2 GPa. It should be noted that the point of the maximum shear stress is located not at the direct contact surface, but at a depth of about 70 nm measured from the sample surface. This distance is approximately half the contact radius, $a = (R\,h)^{0.5}$. It has been reported that the transition from the diamond to β-tin structure occurs at a hydrostatic compressive pressure of ~11 GPa [28], and hence it is interesting to check the hydrostatic pressure distribution. As shown in Figure 2.22(c), a sample volume directly below the indenter tip with a depth of ~25 nm and a contact radius of ~100 nm experiences the compressive hydrostatic pressure larger than 12 GPa. Therefore, this indented volume is assumed to be transformed into metallic β-tin structure at the transition point.

In short, the stress field analysis by the Hertz contact elastic theory provides an opportunity to measure the elastic-plastic transition of thin films by nanoindentation.

2.4.3.3 Structural compliance

In nanoindentation analysis, the sample being indented is assumed to be homogeneous, structurally dense, and semi-infinite in length. Also, the sample surface should be perfectly flat and perpendicular to the indentation direction. Strictly speaking, these ideal conditions need to be satisfied in order to apply a standard analytical method such as introduced by Oliver and Pharr [19]. This is true since the method is essentially derived from a

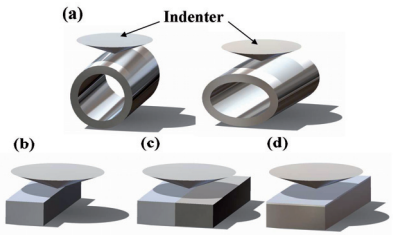

Figure 2.23 Sources of structural compliance [29]. (a) Specimen scale deformation. (b) Elastic heterogeneities such as free edges or (c) interface with a dissimilar material. (d) Layered specimen. The figures are modified from ref. [29].

contact mechanics theory which, of course, does not take any heterogeneities of the sample into account. In most practical applications of nanoindentation on common materials, however, the influence of sample heterogeneity is believed to be small and hence is often neglected. Nevertheless, systematic errors in nanoindentation data may appear if the sample heterogeneity is overwhelmingly large such as for indentations on a porous sample and on a rigid particle sample embedded in a compliant mounting material.

Jakes *et al*. have defined the so-called “structural compliance” in order to account for the influence of the sample heterogeneity on the nanoindentation measurement [29, 30]. They illustrated examples of the sources of structural compliance as shown in Figure 2.23. For instance, when an indentation is performed on a flexible or structurally not rigid sample such as for Figure 2.23(a), a large elastic displacement of the sample itself is expected to be involved during the measurement, and hence the as-measured depth displacement will largely overestimate a true indentation penetration depth. Such an additional displacement due to structural compliance needs to be corrected before applying the standard Oliver-Pharr method in order to obtain the correct reduced modulus and hardness values.

It is rather improbable that the structural compliance is defined as a fixed value for each sample being indented. Since the structural compliance is caused by macro- as well as microscopic sample heterogeneities, its value may change largely depending on a location where the indentation is

performed on the sample. In other words, the structural compliance needs to be measured and corrected for each indentation experiment. A possible practical approach for correcting the structural compliance has been proposed previously by Jakes *et al*. [29, 30], which employs a multi-loading and unloading function in order to account for the structural compliance for each indentation testing. The method is described below with a modified set of equations from the original ones [29, 30], but the basic principle is essentially the same.

Assuming that additional displacements due to sample heterogeneities are represented by elastic deformation, its structural compliance, C_s, can linearly be added to the machine compliance, C_m, in equation (2.16):

$$\frac{1}{S_t} = \left(\frac{\sqrt{\pi}}{2}\frac{\sqrt{H}}{E_r}\right)\frac{1}{\sqrt{P_{max}}} + C_m + C_s \,. \tag{2.29}$$

While the machine compliance, C_m, can uniquely be defined using a standard sample, the C_s value is expected to be varied for each indentation depending on the structural feature of the sample. The simultaneous determination of C_s during indentation testing can be achieved by applying a multi-loading and unloading function with successively increased peak loads. An example of the functions, also used in the present work, is presented in Figure 2.24. The sequence contains ten unloading segments with successively increased peak loads from 0.45 to 2 mN. Hence, during this single indentation, ten values of as-measured contact

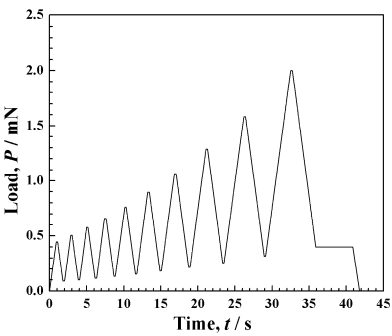

Figure 2.24 Multi-loading and unloading function used for correction of structural compliance, C_s

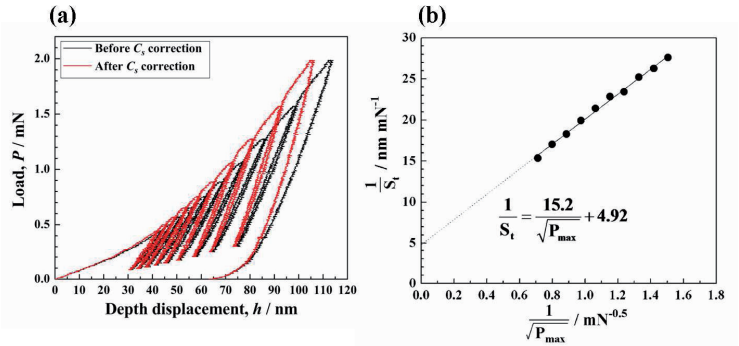

Figure 2.25 Correction method for structural compliance, C_s. (a) Example of load–displacement curves measured for γ′-Fe_4N bulk-like sample using multi-loading and unloading function. Both data before and after the correction of structural compliance, C_s, are presented for comparison. (b) Linear plot to determine the structural compliance value, C_s.

stiffness, S_t, can be evaluated from the unlading segments at varied peak loads. Consequently, similar to the determination of C_m value introduced above, a linear plot can be constructed according to equation (2.29). Here, the intercept value represents the sum of C_m and C_s. Similar to equation (2.14), the contributions of both C_m and C_s are subtracted from the as-measured displacement:

$$h = h_t - P(C_m + C_s)\,. \tag{2.30}$$

As an example for C_s determination, Figure 2.25(a) demonstrates a load–displacement curve measured with the loading function of Figure 2.24 on a partially sintered γ′-Fe_4N bulk-like sample containing porosities. More detailed information about the study is presented later in Chapter 4. Figure 2.25(b) illustrates a linear plot constructed according to equation (2.29). The intercept value is measured to be 4.92 nm/mN which represents the sum of C_m and C_s values. Since the C_m value was determined to be 1.10 nm/mN for the machine set-up employed, the C_s value for this particular indentation is calculated to be 3.81 nm/mN. This additional compliance is believed to be due to the porosity effect being present within the sample.

2.5 First principles calculations

One of the most important scientific achievements of the twentieth century is the development of the theory of quantum mechanics. The properties of matter can well be described in the quantum theory by the Schrödinger equation as follows

$$H\psi = E\Psi , \tag{2.31}$$

where H is the Hamiltonian operator, ψ is a wavefunction, and E is the total energy of the system. With the Born-Oppenheimer approximation, i.e. the fixed positions of atomic nuclei, the resultant form of Hamiltonian is described as

$$H = -\frac{\hbar^2}{2m}\sum_{i=1}^{N}\nabla_i^2 + \sum_{i=1}^{N}V(r_i) + \sum_{i=1}^{N}\sum_{j<i}U(r_i, r_j), \tag{2.32}$$

where the first, second, and third terms are the kinetic energy of each electron with the electron mass, m, the interaction energy between each electron and the atomic nuclei, and the interaction energy between electrons, respectively. The solution of the Schrödinger equation with the Hamiltonian above, i.e. electronic wave function, ψ is a function of each of the spatial positions of each of the N electrons, and hence it becomes a many body problem.

Density Functional Theory (DFT) [31] states that there is a one-to-one correspondence between the ground state wave function and the ground state electron density, $n(r)$. This means that the Schrödinger equation with N electrons can be solved not through finding a function of $3N$ variables, but by finding a function of only 3 spatial variables. The problem can then be described by the Kohn–Sham equation [32] with the form of

$$\left[-\frac{\hbar^2}{2m}\nabla^2 + V(r) + V_H(r) + V_{XC}(r)\right]\psi_i(r) = \varepsilon_i\psi_i(r). \tag{2.33}$$

The first potential term, V, determines the interaction between an electron and the atomic nuclei as appeared in the complete Schrödinger equation

above. The second one, V_H, is referred to as the Hartree potential defined by

$$V_H(r) = e^2 \int \frac{n(r')}{|r - r'|} d^3r' . \quad (2.34)$$

V_{XC} is the exchange and correlation potential which is mathematically given by a derivative of the exchange and correlation energy, E_{XC}, as

$$V_{XC}(r) = \frac{\delta E_{XC}(r)}{\delta n(r)} . \quad (2.35)$$

The exact form of the exchange and correlation potential is however not known.

To solve the Kohn–Sham equation, one needs to define the Hartree potential. To define the Hartree potential, one requires to know the electron density. To obtain the electron density, the single-electron wave functions have to be found. To know the electron wave functions, one needs to solve the Kohn–Sham equation: A circular argument which can be solved iteratively by numerical computation.

References

[1] T.W. Barbee Jr, W.H. Holmes, D.L. Keith, M.K. Pyzyna, G. Ilonca, Thin Solid Films 45 (1977) 591.
[2] S. PalDey, S.C. Deevi, Mater. Sci. Eng. 342 (2003) 58.
[3] M. Zhou, Y. Makino, M. Nose, K. Nogi, Thin Solid Films 339 (1999) 203.
[4] X.D. Xiang, Annu. Rev. Mater. Sci. 29 (1999) 149.
[5] K. Rajan, Annu. Rev. Mater. Res. 38 (2008) 299.
[6] E.J. Amis, Nat. Mater. 3 (2004) 83.
[7] J.J. Harris, B.A. Joyce, P.J. Dobson, Surf. Sci. 103 (1981) L90.
[8] F. Tang, T. Parker, G-C. Wang, T-M. Lu, J. Phys. D: Appl. Phys. 40 (2007) R427.
[9] D. Litvinov, T. O'Donnell, R. Clarke, J. Appl. Phys. 85 (1999) 2151.
[10] S. Andrieu, P. Fréchard, Surf. Sci. 360 (1996) 289.
[11] J.A. Thornton, D.W. Hoffman, Thin Solid Films 171 (1989) 5.
[12] F.M. D'Heurle, J.M.E. Harper, Thin Solid Films 171 (1989) 81.
[13] G.G. Stoney, Proc. R. Soc. London, Ser. A 82 (1909) 172.
[14] E. Chason, http://www.k-space.com/pdfs/kSA_MOS_Resolution.pdf.
[15] P. Hovington, D. Drouin, R. Gauvin, D.C. Joy, N. Evans, Scanning 19 (1997) 29.

[16] P. Hovington, D. Drouin, R. Gauvin, Scanning 19 (1997) 1.
[17] D. Drouin, P. Hovington, R. Gauvin, Scanning 19 (1997) 20.
[18] B.D. Cullity, Elements of X-ray Diffraction, Addison-Wesley, Reading (1978).
[19] W.C. Oliver, G.M. Pharr, J. Mater. Res. 7 (1992) 1564.
[20] W.C. Oliver, G.M. Pharr, J. Mater. Res. 19 (2004) 3.
[21] A.C. Fischer-Cripps, Surf. Coat. Technol. 200 (2006) 4153.
[22] A.C. Fischer-Cripps, Vacuum 58 (2000) 569.
[23] T. Chudoba, N.M. Jennett, J. Phys. D: Appl. Phys. 41 (2008) 215407.
[24] K.L. Johnson, Contact mechanics, Cambridge University Press, Cambridge (1985).
[25] A.C. Fischer-Cripps, Introduction to Contact Mechanics, Springer, New York (2000).
[26] E.R. Weppelmann, J.S. Field, M.V. Swain, J. Mater. Res. 8 (1993) 830.
[27] J.E. Bradby, J.S. Williams, J. Wong-Leung, M.V. Swain, P. Munroe J. Mater. Res. 16 (2001) 1500.
[28] J.Z. Hu, L.D. Merkle, C.S. Menoni, I.L. Spain, Phys. Rev. B 34 (1986) 4679.
[29] J.E. Jakes, C.R. Frihart, J.F. Beecher, R.J. Moon, D.S. Stone, J. Mater. Res. 23 (2008) 1113.
[30] J.E. Jakes, C.R. Frihart, J.F. Beecher, R.J. Moon, P.J. Resto, Z.H. Melgarejo, O.M. Suarez, H. Baumgart, A.A. Elmustafa, D.S. Stone, J. Mater. Res. 24 (2009) 1016.
[31] P. Hohenberg, W. Kohn, Phys. Rev. B 136 (1964) B864.
[32] W. Kohn, L.J. Sham, Phys. Rev. B 140 (1965) A1133.

Chapter 3
Combinatorial thin film synthesis and mechanical properties of YPd_3B

3.1 Introduction

The ternary perovskite boride YPd_3B belongs to a large group of cubic non-oxide perovskite phases with the general formula of RM_3X, where *R* and *M* are metals, and *X* is a light element of B, C, or N. These phases are drawing a lot of attention due to their interesting properties [1-13] such as superconductivity [1-3], negative thermal expansion [4], giant magnetoresistance [5], and negative temperature coefficient of resistance [6]. For the mechanical properties, it has been suggested that RM_3X may possess an unusual combination of metallic and ceramic properties similar to damage tolerant nanolaminate compounds, the so-called MAX-phases [7-10]. According to the previously performed *ab initio* calculations, the bulk to shear modulus ratio of YPd_3B has been reported to be 3.4 [7]. Hence, according to a classical classification of the ductile–brittle behavior of materials [14], YPd_3B may exhibit ductility. In spite of these exciting and from an application point of view interesting mechanical properties, no experimental evaluation of this notion is available in the literature.

The crystallographic structure of perovskite YPd_3B can be derived from an extension of the binary YPd_3 phase, which exists as a stable form, and crystallizes in an ordered face-centered-cubic (fcc) structure, the so-called $L1_2$ structure [15]. In this unit cell, Y atoms are positioned at the corner sites and Pd atoms are at the face centered sites. The insertion of one B atom into the body centered site in the $L1_2$-YPd_3 unit cell leads to the YPd_3B perovskite structure. The YPd_3B stoichiometry is achieved by full occupation of the body centered sites with B atoms. However, Schaak *et al*. have previously reported based on the lattice parameter measurements of YPd_3B_x bulk samples that the $L1_2$-YPd_3 phase can accommodate a

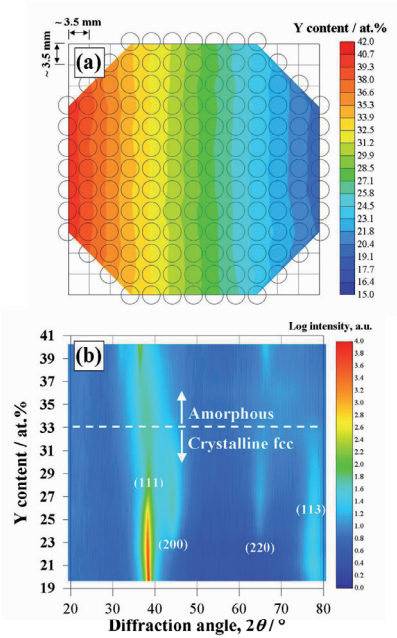

Figure 3.1 Composition-structure map created from combinatorial Y-Pd thin film. (a) Composition spread measured by EDX. The composition map includes total 145 measurement points with a grid size of 3.5 mm. (b) XRD intensity map measured along the composition gradient. The map contains 13 diffraction data. The color intensity is constructed by data interpolation and subsequent smoothening.

maximum B content of $YPd_3B_{0.5}$ [11]. Consequently, the synthesis of the stoichiometric YPd_3B perovskite is believed to involve B supersaturation and hence a thermodynamical non-equilibrium scenario. Hence, it is a challenging task to form and experimentally explore the mechanical properties of the perovskite YPd_3B phase.

A possible approach for the synthesis of non-equilibrium phases is to utilize physical vapor condensation techniques such as sputtering. The formation of non-equilibrium phases with an extended solubility can readily be achieved during sputter deposition especially at low substrate temperatures due to the kinetically limited adatom mobility [16, 17] as the quenching rates are on the order of 10^{15} K/s [18]. Figure 3.1 shows a composition-structure map constructed from a preliminary study on a combinatorial Y-Pd thin film deposited at low temperatures. A compositional gradient ranging from 20 to 40 at.% Y is obtained on a 2 inch Si substrate (Figure 3.1(a)). The composition of 25 at.% Y corresponds to the stoichiometric YPd_3. It should be noted that, for the Y content up to 25 at.% Y, the Y-Pd thin film exhibits strong (111) as well as minor (113) diffraction peaks from fcc-type structure (Figure 3.1(b)). When the Y content is further

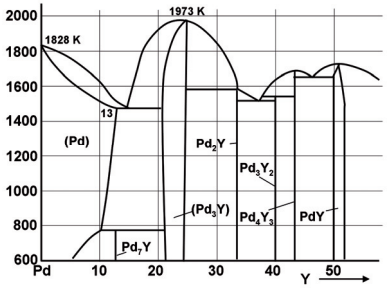

Figure 3.2 Pd-Y phase diagram showing a Pd-rich part reconstructed based on ref. [19].

increased, additional peaks of (200) and (220) appear, but the whole diffraction intensities decrease significantly and the peaks become broader (note that the peak intensity in Figure 3.1(b) is displayed in a log-scale). Eventually, for the composition close to 33 at.% Y, the film structures can be described as X-ray amorphous. On the other hand, according to a binary phase diagram as shown in Figure 3.2 [19], YPd_3 has a homogeneity range of about 4–5 at.% towards a lower Y content, and is hence in thermodynamic equilibrium for a composition range of 25–33 at.% Y with YPd_2. Evidence for the formation of YPd_2 cannot be detected by XRD data measured on the Y-Pd film, implying that the homogeneity range for the fcc-type YPd_3 can be extended to some extent to an overstoichiometric direction due to the limited kinetics of the constituent atoms during thin film growth at low temperatures. The notion of limited adatom mobility during film growth is consistent with the formation of an amorphous phase at higher Y concentrations.

In this work, we grow Y-Pd-B thin films by sputtering in order to investigate the potentially interesting mechanical properties of the perovskite YPd_3B. Structurally-related binary YPd_3 and pure Pd films were also deposited for comparison. The film mechanical properties of the elastic modulus, hardness, as well as critical shear stress for the onset of the plastic deformation were probed by nanoindentation.

3.2 Thin film depositions and characterization

Thin film samples were deposited using magnetron sputtering with the system shown in Figure 2.5. Figure 3.3 gives a schematic illustration of the

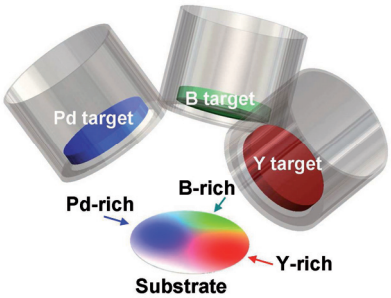

Figure 3.3 Schematics of targets–substrate arrangement for sputter deposition of Y-Pd-B thin films from elemental targets.

targets–substrate arrangement of the experimental set-up employed here. Pure elemental targets (50 mm in diameter) of Y, Pd, and B were co-sputtered with the Ar pressure of 0.4 Pa onto a 2 inch Si(100) wafer. The targets to substrate distance was ~10 cm. The base pressure prior to depositions was 1×10^{-6} Pa. The Y and Pd targets were sputtered at the DC powers of 10 and 8 W, respectively, while the B target at the RF power of 140 W for a compositionally homogeneous film and of 90 W for a combinatorial film. A homogeneous Y-Pd film was deposited at the same sputtering powers, but without the B target being sputtered. Depositions for 3 hours resulted in the film thickness of about 1.5 μm. A pure Pd thin film with approximately the same thickness was also deposited at the DC power of 16 W for 1.5 hours. For all the depositions, the substrate was electrically grounded, and no intentional substrate heating was applied.

The compositions of the homogenous Y-Pd-B and Y-Pd films were analyzed using wavelength dispersive X-ray spectroscopy (WDX, performed at Central Facility for Electron Microscopy (GFE), RWTH Aachen University) with an acceleration voltage of 15 kV. Especially for the purpose of B quantification, elastic recoil detection analysis (ERDA, performed at Forschungszentrum Dresden-Rossendorf) was also carried out with 35 MeV Cl^{7+} incidence ions. The composition data of the combinatorial film were obtained using EDX with an acceleration voltage of 10 kV. The homogeneous Y-Pd-B film characterized using the WDX was used as a standard sample for B quantification in the present EDX measurements. The structures for the homogeneous films were studied using XRD

(Siemens D5000) under the Bragg–Brentano geometry. An X-ray diffraction system equipped with a collimated X-ray beam and an area detector (Bruker D8 GADDS) was employed to locally probe the structure on the combinatorial film. The collimator size used was 0.5 mm in diameter, and the beam incident angle was fixed at 20°. The film texture evolution was also studied using the GADDS system. Fiber texture plots were measured for (111) and (200) diffraction planes with the fixed incident angles of 18.7° and 21.8°, respectively. The microstructure of the homogenous Y-Pd-B thin film was observed by transmission electron microscopy (TEM, performed at Central Facility for Electron Microscopy (GFE), RWTH Aachen University). Cross-sectional TEM samples were prepared using the focused ion beam (FIB) workstation FEI Strata FIB 205. The TEM investigations were performed in a 200 kV field emission TEM FEI Tecnai F20 ST. The film mechanical properties were measured by nanoindentation (Hysitron TriboIndenter) with a peak load up to 3 mN with a Berkovich indenter. In addition, the critical shear stresses for the onset of the plastic deformation were also evaluated using a blunt Berkovich tip with a tip radius of about 760 nm. The determination of tip radius and the elastic stress field analysis were described in Chapter 2, section 2.4.3.2.

3.3 Results and discussion

Based on the WDX measurements, the composition of the homogeneous Y-Pd-B film was determined to be 20.4 at.% Y and 24.0 at.% B, while that of the binary Y-Pd film was 24.9 at.% Y. These measured film compositions give rise to the chemical formulas of $YPd_{2.73}B_{1.18}$ and $YPd_{3.02}$, which are close to the stoichiometric compositions of YPd_3B and YPd_3, respectively. The B content in the ternary film measured by ERDA was 24.9 at.% B, which is close to the WDX data. Consequently, the homogeneous Y-Pd-B film deposited is found to contain a higher amount of B than the stoichiometric YPd_3B.

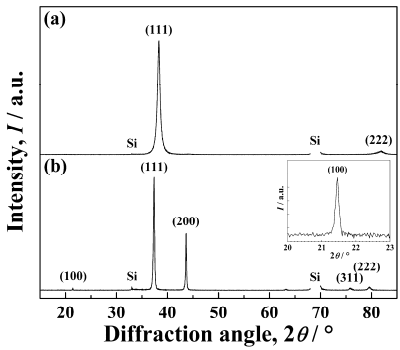

Figure 3.4 XRD patterns for (a) binary $YPd_{3.02}$ and (b) ternary $YPd_{2.73}B_{1.18}$ thin films deposited on Si(100) substrates. The inset emphasizes the (100) superlattice diffraction detected for $YPd_{2.73}B_{1.18}$ film.

Figures 3.4(a) and (b) show the XRD diffractograms for the homogeneous $YPd_{3.02}$ and $YPd_{2.73}B_{1.18}$ films, respectively. For the $YPd_{3.02}$ film, only two diffraction peaks are detected at 2θ angles of around 38.3° and 81.8° due to film texture in Bragg–Brentano geometry. These two peaks can be attributed to diffractions from (111) and (222) planes in the fcc-type structure. The pure Pd film exhibited a (111) fiber texture as well. For the $YPd_{3.02}$ film, the lattice parameter estimated from the measured (111) *d*-spacing is 0.407 nm. This is in very good agreement with previously reported lattice parameters of 0.407 nm [11] and 0.4074 nm [15] for $L1_2$-YPd_3. However, possible superlattice diffractions from (100) and (110) due to atomic ordering for the $L1_2$ structure are not seen in the diffractogram. This is probably due to the fact that the film is strongly (111) textured, and/or due to the formation of a metastable disordered fcc-YPd_3 phase, which might be formed because of the kinetically limited film growth at low substrate temperatures. In fact, the formation of disordered fcc-Ni_3Al instead of the ordered $L1_2$-Ni_3Al has been reported in sputter deposited thin films at low temperatures [20].

The XRD data of the $YPd_{2.73}B_{1.18}$ film (see Figure 3.4(b)) reveals major diffraction peaks at around 37.4° and 43.7°. These peaks can be associated with the diffractions from (111) and (200) planes in the fcc-type structure. Note that, in contrast to the $YPd_{3.02}$ film shown in Figure 3.4(a), the (200) peak was clearly detected. As we will see later on, this is due to the co-existence of both (111) and (200) fiber texture components in the

film. Furthermore, the (100) superlattice diffraction was also detected (see inset in Figure 3.4(b)), which indicates, at least in part, the ordered occupation of Y atoms at the corner sites and/or B at the body centered site in the perovskite unit cell. No other phases are evident from the diffractogram, implying that the film is phase pure. The lattice parameters estimated from the measured (111) and (200) *d*-spacings in the $YPd_{2.73}B_{1.18}$ film are derived to be 0.417 nm and 0.414 nm, respectively, with the mean value of 0.415(5) nm. Hence, compared to the binary YPd_3 phase, an approximately 2% lattice expansion is obtained. This indicates that B is incorporated in the structure.

The chemical composition of the homogeneous $YPd_{2.73}B_{1.18}$ film deviates slightly from the ideal stoichiometry of YPd_3B. To probe the influence of the compositional variation on the structure evolution, a combinatorial Y-Pd-B film was deposited. The effect of the B concentration on the interplanar distances was investigated for a constant Pd to Y ratio of 2.96 ± 0.08. According to the EDX measurements, a concentration spread of 15–25 at.% B was measured along a distance of 42 mm on the substrate as shown in Figure 3.5(a), where the B content of 20 at.% corresponds to the stoichiometric YPd_3B. The structures probed at the respective locations were all identified as the phase pure fcc-type structure irrespective of the local B content variation. Figure 3.5(b) gives the change in (111) and (200) lattice parameters measured along the B content gradient. It can be seen that the (111) lattice parameter increases from 0.414 to 0.418 nm corresponding to a 1% change as the B content is increased from 15 to 25 at.% whereas the (200) lattice parameter changes only slightly from 0.414 to 0.415 nm corresponding a 0.2% change. It is reasonable to assume that the systematic change in lattice parameter is caused by the B incorporation in the YPd_3 lattice. The anisotropy of (111) and (200) lattice parameters, which increases with increasing the B content, could be interpreted by adopting a model proposed by Goldfarb *et al.* [21], which explains the

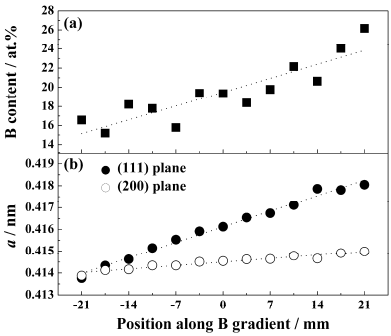

Figure 3.5 Change in lattice parameter of YPd_3B_x with B content gradient probed on combinatorial Y-Pd-B thin film: (a) EDX results for B content, and (b) lattice parameters measured from (111) and (200) diffraction planes.

expansion of the (111) lattice parameter observed in cubic transition metal nitride thin films. Namely, interstitial atoms are selectively trapped depending on the type of crystallographic planes. In the case of YPd_3B_x, the B atoms should be incorporated into interstitial sites, preferably octahedral sites, of the fcc-type YPd_3 lattice during thin film growth. The number of interstitial sites per unit area on the (111) layer should be higher than on the (100) layer as in the case for cubic transition metal nitride thin films [21]. Consequently, a higher intake probability of B atoms in (111) oriented grains is expected than in (200) orientated grains. This selective trapping of B atoms might eventually lead to the larger lattice expansion in (111) oriented grains than in (200) oriented grains as shown in Figure 3.5(b). Nevertheless, possible microstructural effects such as residual stress, oriented stacking faults and dislocation loops may also contribute towards the lattice parameter anisotropy [22, 23].

Generally speaking, the here obtained lattice parameters from the combinatorial YPd_3B_x ($0.71 \leq x \leq 1.33$) as well as the homogeneous $YPd_{2.73}B_{1.18}$ films are larger than the 0.4133 nm reported previously for the bulk $YPd_3B_{0.5}$ sample [11]. This supports the hypothesis that excess B in YPd_3B_x with $x > 0.5$ can be incorporated into the lattice during kinetically limited thin film growth at low temperatures. However, if the change in lattice parameter of bulk YPd_3B_x samples in reference [11] is linearly extrapolated with the B content, an lattice parameter for stoichiometric YPd_3B is estimated to be about 0.420 nm, which is about 1% larger than the

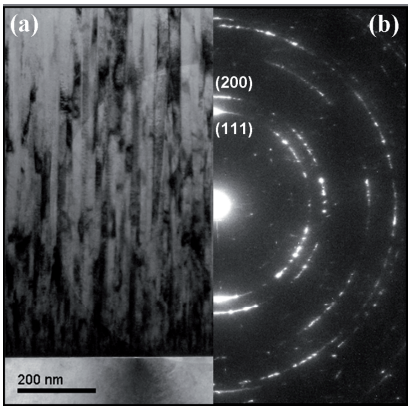

Figure 3.6 TEM micrograph showing the cross sectional microstructure of a $YPd_{2.73}B_{1.18}$ thin film: (a) Bright field image and (b) electron diffraction pattern. The patterns can be identified as fcc-type structure. Only (111) and (200) diffractions are indexed here.

mean lattice parameters, i.e., the average of (111) and (200) lattice parameters, obtained in the present thin film study. The reason for this minor discrepancy is still unknown. It might be the case that some excess B atoms were not incorporated into the lattice. Namely, although the films were deposited at low temperatures, a part of the excess B atoms might gain the enough surface adatom mobility to find energetically more preferential locations such as segregation at grain boundaries and stacking faults. Otherwise, a more complex microstructural evolution might be involved during film growth. For instance, it has been observed in sputter deposited overstoichiometric TiB_2 thin films that ~20 nm wide columnar grains consist of a bundle of ~5 nm diameter TiB_2 subcolumns separated by an ultrathin B-rich tissue phase [24].

To obtain more detailed microstructural information, we have performed TEM investigations on the $YPd_{2.73}B_{1.18}$ film, and preliminary results were previously reported [25]. Figure 3.6(a) gives a TEM bright-field image showing a cross sectional feature of the film. The film microstructure is found to be rather dense, and exhibits columnar grains with column widths of 20–30 nm. The columnar grains appear to be fully crystalline, and no clear evidence for the existence of a second phase or amorphous phase can be seen. Furthermore, the careful analysis of the selected area diffraction pattern (see Figure 3.6(b)) in connection with the bright-field image reveals that the diffraction intensities from both (111) and (200)

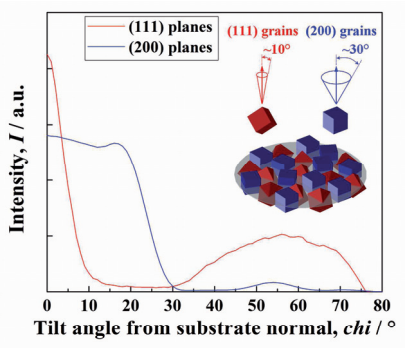

Figure 3.7 Fiber texture plots obtained for (111) and (200) diffraction planes in $YPd_{2.73}B_{1.18}$ thin film. The inset schematics illustrates the co-existence of both (111) and (200) fiber textures.

planes are relatively strong in the film growth direction. This indicates that the film microstructure consists of both (111) and (200) fiber texture components, which is also consistent with the XRD result from Figure 3.4(b).

The texture evolution in the $YPd_{2.73}B_{1.18}$ film was further studied using XRD. Figure 3.7 shows the fiber texture plots obtained for the (111) and (200) diffraction planes as a function of tilt angle, *chi*, with respect to the substrate normal. The fiber texture plot represents semi-quantitatively the angular distributions of the (111) and (200) fiber texture axes. As can be seen from the figure, large fractions of both (111) and (200) axes are oriented close to the substrate normal (*chi* = 0°), indicating that the film microstructure is composed of a mixture of (111) and (200) fiber textures. This is consistent with the results of XRD and TEM investigations as presented earlier. The (111) fiber texture component is rather sharp with an angular distribution of only less than 10° with respect to the surface normal while the (200) texture component shows a broader angular distribution up to 30°. Moreover, the (200) texture component exhibits an additional intensity peak at about 16°. Note that this peak at around 16° may be associated with a twinning of (111) fiber textured grains as suggested previously [26]. This implies that an appreciable amount of twins are introduced during the thin film growth. A fraction of twinned (111) fiber textured grains might contribute to the subsequent growth of (200) texture since the (200) planes by twinned (111) grains are inclined only by 16° from the substrate normal. Twin boundaries might also act as preferential incorporation sites for excess B in the film.

The film mechanical properties were studied by nanoindentation. The maximum indentation penetration depth at a load of 3 mN was about 120 nm which is less than 10% of the film thickness. Therefore, the influence of substrate on the nanoindentation measurements is expected to be small. The reduced modulus of the $YPd_{2.73}B_{1.18}$ film was 139 ± 2 GPa. Indentations were also carried out on the combinatorial YPd_3B_x film along the B gradient at the same locations as in Figure 3.5. The measured reduced moduli were in the range of 127–145 GPa, which are similar to the value obtained from the $YPd_{2.73}B_{1.18}$ film. In the present nanoindentation study on the combinatorial film, no clear correlation between the reduced modulus and the B content was detected. If we employ a previously calculated Poisson's ratio of 0.37 for YPd_3B [7], the elastic modulus of the $YPd_{2.73}B_{1.18}$ film is calculated to be 137 ± 2 GPa. This value deviates by 14% from the calculated one of 120 GPa for YPd_3B [7], and hence is in good agreement with *ab initio* calculations. For comparison, the reduced modulus of the $YPd_{3.02}$ film was 155 ± 2 GPa. It may appear that the B incorporation into the YPd_3 lattice leads to the stiffness reduction. The decrease in stiffness with increasing the lattice volume has also been reported in fcc stainless steels with carbon and nitrogen as interstitial alloying elements [27]. However, we neglect any microstructural effects such as texture, residual stress, and grain size on the measurement of the reduced modulus by nanoindentation. These issues should be addressed in order to evaluate the influence of B incorporation into the YPd_3 lattice on the stiffness. In fact, we measured the elastic modulus of 167 ± 3 GPa by nanoindentation performed on the pure Pd film exhibiting a strong (111) fiber texture. A Poisson's ratio of 0.386 [28] was employed to calculate the elastic modulus from the reduced modulus measured. The elastic modulus of a bulk polycrystalline Pd was reported to be 132 GPa [28]. Hence, the here obtained elastic modulus of the Pd film is overestimated, which may be

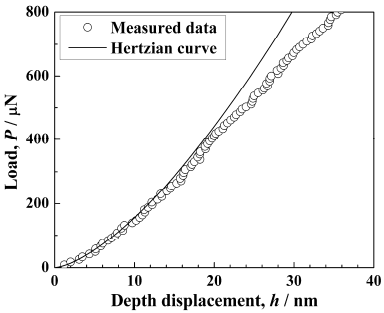

Figure 3.8 Initial portion of load–displacement curve measured on $YPd_{2.73}B_{1.18}$ thin film using a blunt Berkovich indenter tip. A theoretical curve calculated by Hertz contact theory is also plotted for comparison.

attributed to the (111) texture growth with a combination of elastic modulus anisotropy as reported previously [29].

The hardness values of the $YPd_{2.73}B_{1.18}$ and $YPd_{3.02}$ films were 11.6 ± 0.2 GPa and 10.8 ± 0.2 GPa, respectively, whereas that of the pure Pd film was 4.7 ± 0.1 GPa. Note that the here obtained hardness value of the $YPd_{2.73}B_{1.18}$ film is larger than those of other perovskite borides in bulk samples, e.g., 7.5 GPa for YRh_3B [30] and 9.9 GPa for $ScRh_3B$ [31]. In contrast, *ab initio* calculations have predicted that the shear modulus of YPd_3B is 44 GPa while that of YRh_3B is 96 GPa [7]. This implies that YPd_3B is intrinsically less resistant against plastic deformation, and hence exhibits a lower hardness value than YRh_3B. This discrepancy could be explained in terms of the microstructural effect, in particular, the Hall-Petch effect [32, 33] that the hardness increases with decreasing the grain size. As we have seen earlier, the $YPd_{2.73}B_{1.18}$ film consists of very fine grains with 20–30 nm column width while a typical grain size of a bulk sample is on the micrometer scale or even larger.

The mechanical properties of the films were further studied by nanoindentation with the aid of the Hertzian elastic contact theory for a spherical tip. The present work employed a blunt Berkovich indenter tip as a spherical tip with the corresponding tip radius of about 760 nm. Figure 3.8 shows an example of the initial stages of loading curves measured on the $YPd_{2.73}B_{1.18}$ film. The figure also contains a theoretical Hertzian curve calculated based on equation 2.17. It can be seen that an initial stage of the

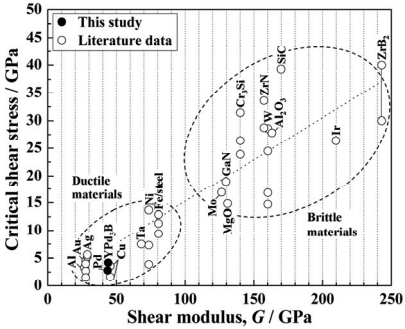

Figure 3.9 Critical shear stresses for the onset of plasticity for $YPd_{2.73}B_{1.18}$ and Pd thin films in comparison with other materials from the literature data. The data is plotted as a function of shear modulus.

deformation can well be described by the Hertzian contact theory, indicating that the deformation is purely elastic in this region. The deviation of the measured data from the Hertzian curve occurs at a load of 471 μN. This load can be regarded as a critical load for the initiation of the plastic deformation of the excited volume. The components of stress tensor can also be analyzed for a given indentation load, which enables to calculate a local maximum shear stress developed within the sample [34]. The maximum shear stress at the critical load, also referred to as critical shear stress, is calculated to be 4.2 GPa, where the Poisson's ratio of 0.37 is employed for the calculation. The statistics out of 20 measurements provided the value of 4.2 ± 0.2 GPa for the $YPd_{2.73}B_{1.18}$ film. Similarly, the critical shear stresses for the pure Pd and $YPd_{3.02}$ films were determined to be 2.8 ± 0.5 GPa and 4.3 ± 0.1 GPa, respectively, assuming that the Poisson's ratio of YPd_3 is the same as pure Pd.

It has been suggested that the critical shear stress obtained by nanoindentation is associated with the homogeneous nucleation of dislocations [35, 36], and is close to the ideal shear strength of materials which can roughly be estimated as ~*G*/10 where *G* is the shear modulus. Therefore, it is reasonable to assume that materials with low critical shear stresses are easily plastically deformable, and the critical shear stress assessed by nanoindentation may be used as an indicator to classify ductile and brittle materials. Figure 3.9 compares the critical shear stresses for a variety of materials available in the literature (Cu [37-39], Al [37], Au [40, 41],

Ag [42], Ni [39, 43, 44], Ta [45], Fe/steel [44, 46, 47], Mo [43], W [36, 44, 48], Ir [49], Cr_3Si [50], GaN [51], MgO [52], Al_2O_3 [53], ZrN [54], ZrB_2 [55], SiC [56]) with those for the $YPd_{2.73}B_{1.18}$ and Pd films in the present study. The corresponding shear moduli are obtained from the literature [7, 14, 57-65]. The positive slope of the critical shear stress – shear modulus dependence is approximately 0.15. The materials listed in the plot may be classified into two groups; ductile materials (Cu, Al, Au, Ag, Ni, Ta, Fe/steel) and brittle materials (Mo, W, Ir, Cr_3Si, GaN, MgO, Al_2O_3, ZrN, ZrB_2, SiC). Ductile materials exhibit lower critical shear stresses and shear modulus whereas brittle materials are characterized by higher critical shear stresses and shear modulus.

While the exact location of the boundary between ductile and brittle material behavior is a matter of debate, it is evident that the critical shear stress for the pure Pd film is comparable to those for typical ductile materials. The $YPd_{2.73}B_{1.18}$ film exhibits a 1.5 times higher critical shear stress than the Pd film, indicating that YPd_3B is more resistant against plastic deformation than pure Pd. However, the magnitude of the critical shear stress is clearly located within the range of ductile materials, and hence YPd_3B can be classified as ductile material which is consistent with previously reported *ab initio* data [7].

3.4 Conclusions

Ternary Y-Pd-B thin films were deposited by magnetron sputtering at low temperatures to explore the mechanical properties of perovskite YPd_3B phase. Binary YPd_3 as well as pure Pd films were also deposited for comparison since they are structurally similar. Based on the XRD data, the compositionally homogeneous $YPd_{2.73}B_{1.18}$ and $YPd_{3.02}$ films deposited were both identified as phase pure fcc-type structures with the measured lattice parameters of 0.415(5) and 0.407 nm, respectively. The structural analysis performed on the combinatorial YPd_3B_x film ($0.71 \leq x \leq 1.33$) revealed that

the (111) lattice parameter increased systematically with increasing the B concentration, which can be interpreted as a B incorporation induced lattice expansion. The $YPd_{2.73}B_{1.18}$ film exhibited a dense columnar grain structure with the column widths of 20–30 nm. The elastic modulus and hardness of the $YPd_{2.73}B_{1.18}$ film measured by nanoindentation were 137 ± 2 GPa and 11.6 ± 0.2 GPa, respectively. The measurement of the critical shear stress for the initiation of the plastic deformation suggests that perovskite YPd_3B can be classified as ductile material.

References

[1] H. Takei, N. Kobayashi, H. Yamauchi, T. Shishido, T. Fukase, J. Less-Common Met. 125 (1986) 233.
[2] T. He, Q. Huang, A.P. Ramirez, Y. Wang, K.A. Regan, N. Rogado, M.A. Hayward, M.K. Haas, J.S. Slusky, K. Inumara, H.W. Zandbergen, N.P. Ong, R.J. Cava, Nature 411 (2001) 54.
[3] I. Hase, Phys. Rev. B 70 (2004) 033105.
[4] A. Pandey, C. Mazumdar, R. Ranganathan, S. Tripathi, D. Pandey, S. Dattagupta, Appl. Phys. Lett. 92 (2008) 261913.
[5] A. Pandey, C. Mazumdar, R. Ranganathan, Appl. Phys. Lett. 94 (2009) 172509.
[6] A. Pandey, C. Mazumdar, R. Ranganathan, M.D. Raychaudhury, T.S. Dasgupta, S. Tripathi, D. Pandey, S. Dattagupta, EPL 84 (2008) 47007.
[7] D. Music, Z. Sun, J.M. Schneider, Phys. Rev. B 71 (2005) 052104.
[8] D. Music, J.M. Schneider, Appl. Phys. Lett. 88 (2006) 031914.
[9] D. Music, J.M. Schneider, Appl. Phys. Lett. 89 (2006) 121914.
[10] D. Music, J.M. Schneider, JOM 59 (2007) 60.
[11] R.E. Schaak, M. Avdeev, W.L. Lee, G. Lawes, H.W. Zandbergen, J.D. Jorgensen, N.P. Ong, A.P. Ramirez, R.J. Cava, J. Solid State Chem. 177 (2004) 1244.
[12] A. Pandey, C. Mazumdar, R. Ranganathan, J. Magn. Magn. Mater. 322 (2010) 3765.
[13] R. Sahara, T. Shishido, A. Nomura, K. Kudou, S. Okada, V. Kumar, K. Nakajima, Y. Kawazoe, Phys. Rev. B 73 (2006) 184102.
[14] S.F. Pugh, Philos. Mag. 45 (1954) 823.
[15] A.E. Dwight, J.W. Downey, R.A. Conner, Acta Crystallogr. 14 (1961) 75.
[16] J.A. Thornton, Annu. Rev. Mater. Sci. 7 (1977) 239.
[17] N. Saunders, A.P. Miodownik, J. Mater. Sci. 22 (1987) 629.
[18] T.W. Barbee, Jr., W.H. Holmes, D.L. Keith, M.K. Pyzyna, G. Ilonca, Thin Solid Films 45 (1977) 591.

[19] B. Predel: *Pd-Y (Palladium-Yttrium)*. O. Madelung (ed.). SpringerMaterials - The Landolt-Börnstein Database (http://www.springermaterials.com).
[20] G.B. Thompson, R. Banerjee, X.D. Zhang, P.M. Anderson, H.L. Fraser, Acta Mater. 50 (2002) 643.
[21] I. Goldfarb, J. Pelleg, L. Zevin, N. Croitoru, Thin Solid Films 200 (1991) 117.
[22] V. Valvoda, Surf. Coat. Technol. 80 (1996) 61.
[23] V. Valvoda, A.J. Perry, L. Hultman, J. Musil, S. Kadlec, Surf. Coat. Technol. 49 (1991) 181.
[24] P.H. Mayrhofer, C. Mitterer, J.G. Wen, J.E. Greene, I. Petrov, Appl. Phys. Lett. 86 (2005) 131909.
[25] R. Iskandar, T. Takahashi, J.M. Schneider, J. Mayer, in: W. Grogger, F. Hofer, P. Pölt (Eds.), Microscopy Conference MC2009, 3 (2009) 305.
[26] I. Tomov, M. Adamik, P.B. Barna, Thin Solid Films 371 (2000) 17.
[27] H.M. Ledbetter, M.W. Austin, Mater. Sci. Eng. 70 (1985) 143.
[28] P.G. Sanders, J.A. Eastman, J.R. Weertman, Acta Mater. 45 (1997) 4019.
[29] S.U. Jen, T.C. Wu, Thin Solid Films 492 (2005) 166.
[30] T. Shishido, J. Ye, K. Kudou, S. Okada, K. Obara, T. Sugawara, M. Oku, K. Wagatsuma, H. Horiuchi, T. Fukuda, J. Alloys Compd. 291 (1999) 52.
[31] T. Shishido, J. Ye, S. Okada, K. Kudou, T. Sasaki, S. Isida, T. Naka, M. Oku, I. Higashi, H. Kishi, H. Horiuchi, T. Fukuda, J. Alloys Compd. 309 (2000) 107.
[32] N.J. Petch, J. Iron Steel Inst. London 174 (1953) 25.
[33] E.O. Hall, Proc. Phys. Soc. London, Sect. B 64 (1951) 747.
[34] A.C. Fischer-Cripps, Introduction to Contact Mechanics, Springer, New York (2000).
[35] D. Lorenz, A. Zeckzer, U. Hilpert, P. Grau, H. Johansen, H.S. Leipner, Phys. Rev. B 67 (2003) 172101.
[36] D.F. Bahr, D.E. Kramer, W.W. Gerberich, Acta Mater. 46 (1998) 3605.
[37] Y. Shibutani, T. Tsuru, A. Koyama, Acta Mater. 55 (2007) 1813.
[38] Z.H. Cao, P.Y. Li, H.M. Lu, Y.L. Huang, X.K. Meng, J. Phys. D: Appl. Phys. 42 (2009) 065405.
[39] D.F. Bahr, G. Vasquez, J. Mater. Res. 20 (2005) 1947.
[40] M. Dietiker, R.D. Nyilas, C. Solenthaler, R. Spolenak, Acta Mater. 56 (2008) 3887.
[41] S.G. Corcoran, R.J. Colton, E.T. Lilleodden, W.W. Gerberich, Phys. Rev. B 55 (1997) 16057.
[42] Y. Cao, S. Allameh, D. Nankivil, S. Sethiaraj, T. Otiti, W. Soboyejo, Mater. Sci. Eng. A 427 (2006) 232.
[43] L. Wang, H. Bei, T.L. Li, Y.F. Gao, E.P. George, T.G. Nieh, Scr. Mater. 65 (2011) 179.

[44] S. Vadalakonda, R. Banerjee, A. Puthcode, R. Mirshams, Mater. Sci. Eng. A 426 (2006) 208.
[45] M.M. Biener, J. Biener, A.M. Hodge, A.V. Hamza, Phys. Rev. B 76 (2007) 165422.
[46] T. Ohmura, K. Tsuzaki, J. Mater. Sci. 42 (2007) 1728.
[47] D.F. Bahr, D.E. Wilson, D.A. Crowson, J. Mater. Res. 14 (1999) 2269.
[48] A.A. Zbib, D.F. Bahr, Metall. Mater. Trans. A 38A (2007) 2249.
[49] K.J. Van Vliet, J. Li, T. Zhu, S. Yip, S. Suresh, Phys. Rev. B 67 (2003) 104105.
[50] H. Bei, E.P. George, J.L. Hay, G.M. Pharr, Phys. Rev. Lett. 95 (2005) 045501.
[51] M. Fujikane, M. Leszczyński, S. Nagao, T. Nakayama, S. Yamanaka, K. Niihara, R. Nowak, J. Alloys Compd. 450 (2008) 405.
[52] Z. Dong, H. Huang, R. Kang, Mater. Sci. Eng. A 527 (2010) 4177.
[53] W.G. Mao, Y.G. Shen, C. Lu, Scr. Mater. 65 (2011) 127.
[54] G.W. Egeland, K. Wheeler, P. Peralta, K.J. McClellan, S.A. Maloy, G.M. Bond, J. Nucl. Mater. 416 (2011) 253.
[55] S. Guicciardi, C. Melandri, F.T. Monteverde, J. Eur. Ceram. Soc. 30 (2010) 1027.
[56] X. Zhao, R.M. Langford, I.P. Shapiro, P. Xiao, J. Am. Ceram. Soc. 94 (2011) 3509.
[57] X. Zhang, X. Luo, J. Han, J. Li, W. Han, Comput. Mater. Sci. 44 (2008) 411.
[58] Y. Sumino, O.L. Anderson, I. Suzuki, Phys. Chem. Miner. 9 (1983) 38.
[59] Z. Li, R.C. Bradt, J. Mater. Sci. 22 (1987) 2557.
[60] F.H. Featherston, J.R. Neighbours, Phys. Rev. 130 (1963) 1324.
[61] D.H. Chung, G. Simmons, J. Appl. Phys. 39 (1968) 5316.
[62] Y. Cheng, Y.-J. Tu, Z.-Y. Zeng, Q.-Q. Gou, Commun. Theor. Phys. 50 (2008) 1443.
[63] X.-J. Chen, V.V. Struzhkin, Z. Wu, M. Somayazulu, J. Qian, S. Kung, A.N. Christensen, Y. Zhao, R.E. Cohen, H.-K. Mao, R.J. Hemley, Proc. Natl. Acad. Sci. USA. 102 (2005) 3198.
[64] H. Bei, E.P. George, G.M. Pharr, Scr. Mater. 51 (2004) 875.
[65] G.R. Speich, A.J. Schwoebl, W.C. Leslie, Metall. Trans. 3 (1972) 2031.

Chapter 4

Elastic properties of perovskite γ′-Fe_4N

4.1 Introduction

Iron nitride, γ′-Fe_4N, crystallizes in a simple cubic structure in the space group $Pm\bar{3}m$. The structure can be described as a variant of face-centered cubic γ-Fe by N atom insertion at the body-centered position. γ′-Fe_4N exhibits rather different physical properties compared to γ-Fe although they are structurally quite similar. For instance, γ-Fe is known to be antiferromagnetic [1] while γ′-Fe_4N is ferromagnetic [2]. The high saturation magnetization and low coercivity of γ′-Fe_4N are attractive for applications such as high-density recording media [3-5]. γ′-Fe_4N is also a common phase after surface nitriding of steel products, which provides the high hardness, excellent wear, and corrosion resistance [6-8]. It should also be pointed out that γ′-Fe_4N has been proposed as a ductile and hence damage-tolerant material due to its high bulk, *B*, to shear modulus, *G*, ratio according to *ab initio* calculations [9-11]. Moreover, it has been suggested that γ′-Fe_4N exhibits an anomalous strength anisotropy [12].

The elastic modulus is one of the most fundamental physical quantities when the mechanical responses of materials are concerned. Despite of the potentially interesting mechanical properties of γ′-Fe_4N as introduced above, the data available on the elastic modulus of γ′-Fe_4N are inconsistent. For instance, it has been proposed that the elastic modulus of γ′-Fe_4N is as high as that of α-Fe [13]. The value was determined to be 211 GPa through mechanical resonance frequency measurements on nitrided steel sheets. However, due to the presence of porosity in the nitride layer, a correction calculation was adopted to estimate the elastic modulus of a fully dense γ′-Fe_4N layer in reference [13]. γ′-Fe_4N layers produced by plasma nitriding treatments of iron and steels have been investigated by

nanoindentation, and the elastic moduli were measured to be 200–205 GPa [14]. On the one hand, the elastic modulus of 172 ± 12 GPa has been reported in a nanoindentation study performed on a γ′-Fe_4N layer formed after friction treatment with nitriding of iron [15]. To the best of our knowledge, no single-crystal samples of γ′-Fe_4N were characterized in terms of elasticity. The elastic moduli obtained by *ab initio* calculations have been reported to be 161.5 GPa (as the mean value of E_{Voigt} and E_{Reuss}) [16], 168.9 GPa [11], and 197.0 GPa [10]. Hence, the difference between the calculated and measured elastic modulus is up to 31%. The reason for this inconsistency is unclear.

To establish the mechanical properties of γ′-Fe_4N, the elastic properties of γ′-Fe_4N are studied experimentally and theoretically. In this work, thin film and bulk-like γ′-Fe_4N samples are synthesized using a reactive magnetron sputtering technique and a two-step ammonolysis reaction, respectively. The elastic moduli of these samples are characterized using nanoindentation, and compared to data obtained by *ab initio* calculations.

4.2 Methods

4.2.1 Thin film depositions

γ′-Fe_4N thin films were deposited using the reactive magnetron sputtering technique. Figure 4.1 gives a photo showing the experimental set-up employed here. A pure Fe (99.95 wt.%) target with the diameter of 50 mm was sputtered at the DC power of 100 W using an Ar and N_2 gas mixture. The Ar pressure was kept constant at 0.5 Pa while the N_2 pressure was varied from 0 up to 0.12 Pa. 2 inch Si(100) wafers were used as substrates. The substrate was placed on a Cu plate heated up to approximately 623 K prior to the depositions. The target–substrate distance was 7 cm. The base pressure before deposition was 2×10^{-4} Pa. The depositions were performed for 60 min for Fe-N reactive sputtering and for 45 min for pure Fe

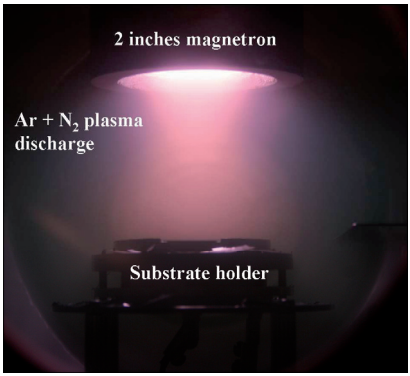

Figure 4.1 Photograph taken during reactive sputter depositions of Fe-N thin films.

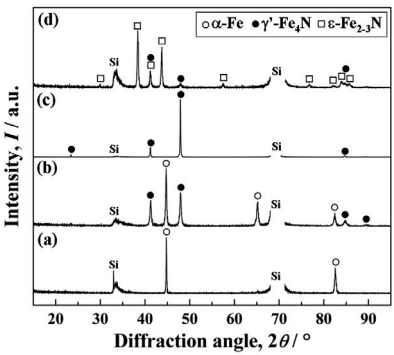

Figure 4.2 XRD patterns for Fe-N thin films deposited with Ar pressure of 0.5 Pa and N_2 pressures of (a) 0 Pa, (b) 0.03 Pa, (c) 0.06 Pa, and (d) 0.12 Pa, respectively.

deposition. These deposition conditions led to the film thicknesses ranging from 1.5 to 2 μm.

Figure 4.2 shows XRD patterns for Fe-N thin films deposited with the N_2 partial pressures of (a) 0 Pa, (b) 0.03 Pa, (c) 0.06 Pa, and (d) 0.12 Pa, respectively. The data were collected using a Siemens D5000 diffractometer in Bragg–Brentano geometry. During reactive sputtering of Fe-N, the film structural evolution is found to be highly sensitive to the partial pressure of N_2. For the film deposited with pure Ar (Figure 4.2(a)), the diffraction peaks can be associated with α-Fe. The film deposited with 0.03 Pa N_2 is characterized as a two phase mixture consisting of α-Fe and perovskite γ′-Fe_4N (Figure 4.2(b)). A slight increase in N_2 pressure to 0.06 Pa leads to the formation of phase pure γ′-Fe_4N (Figure 4.2(c)). A further increase in N_2 pressure to 0.12 Pa changes the major phase constitution of the film from γ′-Fe_4N into ε-$Fe_{2-3}N$ (Figure 4.2(d)). This structural evolution here is qualitatively consistent with the Fe-N phase diagram [17] as shown in Figure 4.3. Namely, α-Fe and γ′-Fe_4N coexist for the N content lower than 20 at.% while γ′-Fe_4N and

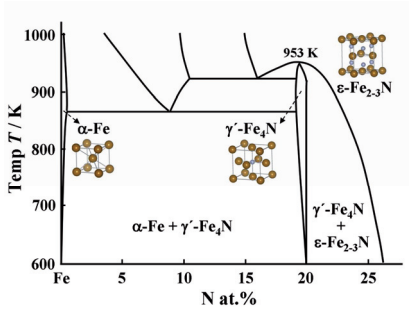

Figure 4.3 Fe-N phase diagram reconstructed based on ref [17].

ε-$Fe_{2-3}N$ for the N content higher than 20 at.%. It should be noted that the homogeneity range of γ′-Fe_4N is very limited, implying that the N_2 partial pressure needs to be adjusted precisely to form single phase γ′-Fe_4N. Similar trends in structural evolution with a variation of N_2 partial pressures have been reported in Fe-N thin films deposited by RF reactive sputtering [18, 19].

Based on the interplanar *d*-spacing measurements, a lattice parameter of the γ′-Fe_4N thin film (Figure 4.2(c)) was determined to be 3.794 Å. This is consistent with the γ′-Fe_4N lattice parameter of 3.790 Å reported previously [20]. According to the chemical composition analysis by wavelength-dispersive X-ray spectroscopy (WDX, performed at Central Facility for Electron Microscopy (GFE)), the N concentration of the thin film was 18.9 at.%, which is very close to the stoichiometric N concentration of γ′-Fe_4N. The thin film sample synthesized here can therefore be regarded as phase-pure γ′-Fe_4N.

Figure 4.4 gives cross sectional SEM micrographs for Fe-N thin films deposited with the N_2 partial pressures of (a) 0 Pa, (b) 0.03 Pa, (c) 0.06 Pa, and (d) 0.12 Pa, respectively. It appears that the phase pure α-Fe and γ′-Fe_4N thin films (Figures 4.4(a) and (c)) exhibit columnar structures with the column width of up to several hundred nanometers whereas the phase mixture films show rather finer microstructural features. The difference in crystallite size was characterized by full width half maximum (FWHM) data obtained from the diffraction peaks in Figure 4.2. The FWHM values evaluated from major diffraction peaks of phase pure α-Fe and γ′-Fe_4N thin films are determined to be 0.154° and 0.124° while those of α-Fe + γ′-Fe_4N

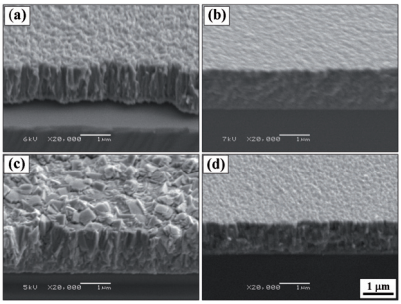

Figure 4.4 Cross-sectional SEM micrographs for Fe-N thin films deposited with Ar pressure of 0.5 Pa and N_2 pressures of (a) 0 Pa (α-Fe), (b) 0.03 Pa (α-Fe + γ'-Fe_4N), (c) 0.06 Pa (γ'-Fe_4N), and (d) 0.12 Pa (γ'-Fe_4N + ε-$Fe_{2-3}N$), respectively.

and γ'-Fe_4N + ε-$Fe_{2-3}N$ films are 0.254° and 0.308°, respectively. Furthermore, the surface of the phase pure γ'-Fe_4N film is found to be very rough. As will be discussed more in detail later, the surface roughness is an important issue in nanoindentation measurements.

4.2.2 Bulk-like samples

The bulk-like γ'-Fe_4N sample was provided from Institute of Inorganic Chemistry (IAC), RWTH Aachen University. The sample was synthesized in a partially sintered form from pure α-Fe powders as a starting material. A two-step ammonolysis reaction with a 3 h sintering step at 1023 K and a 12 h nitridation reaction at 773 K was carried out using a NH_3:H_2 gas mixture with a 1:1 ratio. The partially sintered γ'-Fe_4N bulk-like sample with the dimension of approximately 5 × 5 × 1 mm was analyzed using XRD (Bruker D8 GADDS) with a collimated X-ray beam using a 0.5 mm collimator size and a fixed incident angle of 20°. The XRD result showed that the diffraction peaks detected were all associated with γ'-Fe_4N with a measured lattice parameter of 3.794 Å. According to the EDX measurement, the N concentration of the sample was determined to be 19.7 at.%. Hence, the bulk-like γ'-Fe_4N sample synthesized here can also be regarded as phase-pure γ'-Fe_4N.

4.2.3 Nanoindentation methods

The elastic modulus and hardness were measured using nanoindentation (Hysitron TriboIndenter) with a Berkovich indenter tip. For the thin film, a simple load–unloading function was employed with the maximum load of 2.5 mN. A holding segment for 10 s at a constant load of 0.5 mN was added before complete unloading for the purpose of thermal drift correction. The load–displacement curves obtained were analyzed based on the standard method [21]. Preliminary indentation measurements performed on the as-deposited γ'-Fe_4N thin film showed a large scattering of measured data because of its large surface roughness. A root mean square roughness value of 42 nm was measured using a scanning probe microscope option available in the TriboIndenter. Hence, in order to improve the quality of the nanoindentation measurements, the surface of the as-deposited γ'-Fe_4N thin film was polished to minimize the surface roughness effect. 25 indentations were performed for statistics. The influence of surface roughness on the nanoindentation results is discussed more in details in 4.5 Appendix.

It should be noted that the bulk-like γ'-Fe_4N sample is not structurally dense, and hence the influence of structural compliance, C_s, of the sample on the nanoindentation data needs to be taken into account. The correction method for structural compliance used in this study is described in Chapter 2, Section 2.4.3.3. To perform indentations on the bulk-like γ'-Fe_4N sample, the sample was fixed on a steel plate using a polymer bond. Then, the sample was polished to prepare flat surfaces on γ'-Fe_4N grains. The polymer bond might introduce an additional compliance component, but it can eventually be included into C_s evaluated.

4.2.4 Theoretical methods

Ab initio calculations using the Vienna Ab initio Simulation Package (VASP) [22-24] were performed with projector augmented wave potentials and the

generalized-gradient approximation. A γ′-Fe_4N unit cell consisting of five atoms was studied. The wave functions were sampled on a set of 11 × 11 × 11 *k*-points constructed by the Monkhorst–Pack scheme [25]. The energy cut off on the wave function was 500 eV. Spin polarization was included since the ground state of γ′-Fe_4N is ferromagnetic. The Birch–Murnaghan equation of states [26] was used to fit the energy–volume curve to determine a ground state lattice parameter, *a*, and bulk modulus, *B*. Orthorhombic and monoclinic shear strains were applied to calculate elastic constants of $C_{11} - C_{12}$ and C_{44}, respectively, so the three independent elastic constants for a cubic structure are obtained using the bulk modulus calculated from the energy–volume curve [27]. The average polycrystalline elastic modulus, *E*, and shear modulus, *G*, were calculated based on Hill's approximation scheme [28, 29]. The Poisson's ratio, ν, was obtained using a relation, $\nu = (3B - 2G)/(2(3B + G))$. Table 4.1 lists the results of the *ab initio* calculations.

4.3 Results and discussion

Figures 4.5(a) and (b) provide SEM micrographs for the γ′-Fe_4N thin film and bulk-like sample both after being polished, respectively. In Figure 4.5(a), it can be seen that the γ′-Fe_4N thin film exhibits the columnar growth morphology with a column width of < 1 μm. For the bulk-like sample, γ′-Fe_4N grains are seen to be partially sintered, but the sample is obviously porous. However, the individual γ′-Fe_4N grains appear to be rather dense since no porosity can be detected on the polished surface. It is evident that the polished surface areas of γ′-Fe_4N grains are large enough, i.e. > 5 μm,

a (Å)	C_{11} (GPa)	C_{12} (GPa)	C_{44} (GPa)	*B* (GPa)	*E* (GPa)	*G* (GPa)	ν
3.792	313	137	46	196	162	59	0.36

Table 4.1 Calculated lattice parameter, *a*, elastic constants (C_{11}, C_{12}, and C_{44}), bulk modulus, *B*, elastic modulus, *E*, shear modulus, *G*, and Poisson's ratio, ν, for γ′-Fe_4N.

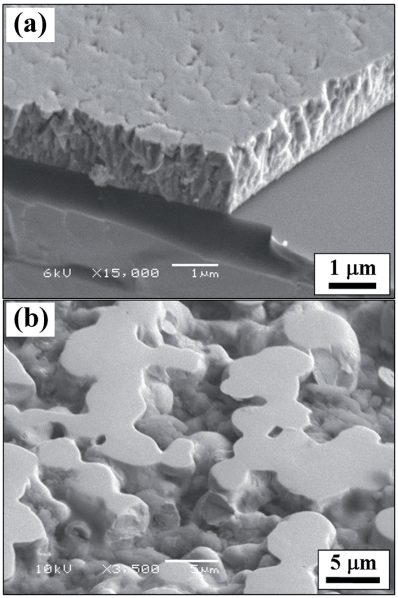

Figure 4.5 SEM micrographs for (a) γ′-Fe_4N thin film and (b) γ′-Fe_4N bulk-like sample after surface polishing for nanoindentation.

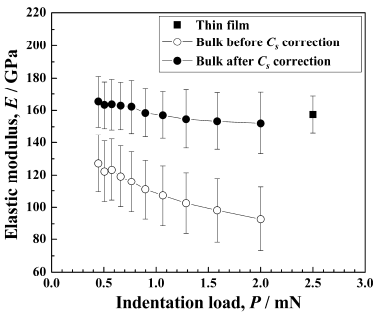

Figure 4.6 Elastic modulus of γ′-Fe_4N bulk-like sample measured by nanoindentation. Both results before and after the correction of structural compliance, C_s, are presented for comparison. The results from γ′-Fe_4N thin film are also included.

for at least a single indentation to be performed.

Figure 4.6 shows the nanoindentation results for the elastic modulus of the γ′-Fe_4N thin film and bulk-like sample as a function of peak loads. To calculate the elastic modulus, E, from the reduced modulus measured, E_r, we employed the calculated Poisson's ratio of 0.36, see Table 4.1. The elastic modulus of the γ′-Fe_4N thin film was measured to be 157 ± 11 GPa, which deviates only 3% from the calculated value of 162 GPa, see Table 4.1, and is consistent with the theoretical data in literature [11, 16]. As addressed above, the bulk-like sample is porous, and hence the influence of which on the nanoindentation measurements should be corrected through the simultaneous determination of structural compliance, C_s, for each indentation experiment. An example of C_s determination is demonstrated in Chapter 2, Section 2.4.3.3. For statistics, we have performed in total 74 indentations on randomly

selected polished γ′-Fe_4N grains. Among all the data measured, however, 25 load–displacement curves were removed since these data exhibited large hysteresis loops during loading and unloading processes. Out of 49 measurements analyzed, the measured C_s values ranged from 1.53 to 17.3 nm/mN with a mean value of 6.49 nm/mN. As shown in Figure 4.6, if the C_s correction is not applied, the elastic moduli of the γ′-Fe_4N bulk-like sample were measured to be in the range of 127 ± 18 GPa at the lowest load to 93 ± 20 GPa at the highest load. These values are up to 41% lower than the values obtained for the γ′-Fe_4N thin film. With the C_s correction, however, the measured elastic moduli range from 165 ± 16 to 152 ± 19 GPa. If we take, as the first approximation, the arithmetic mean value of all the measured values with the C_s correction, the elastic modulus of γ′-Fe_4N bulk-like sample is determined to be 159 ± 17 GPa. This is in good agreement with that of the γ′-Fe_4N thin film measured as well as the *ab initio* calculations.

Our results are in conflict with the previously measured elastic moduli for γ′-Fe_4N of 211 GPa [13] and 200–205 GPa [14], but in relatively good agreement with 172 ± 12 GPa [15]. The exact reason for this scattering among the measured data is not clear. In the previous studies, γ′-Fe_4N samples were prepared by nitriding of iron and steels. It is commonly observed that the compressive residual stress develops in γ′-Fe_4N layers formed after nitriding [16]. Hence, a possible difference in the residual stress state in γ′-Fe_4N layers may in part be responsible for the scattering of the measured elastic moduli of γ′-Fe_4N.

The experimental and theoretical results obtained in the present study indicate that the elastic modulus of γ′-Fe_4N is about 20–25% lower than those of α-Fe, 211 GPa [30], and of γ-Fe austenitic stainless steels, e.g. Fe-Ni-Cr alloys, ~200 GPa [31]. It is very interesting to note that γ′-Fe_4N is more elastically compliant than γ-Fe austenitic stainless steels in spite of

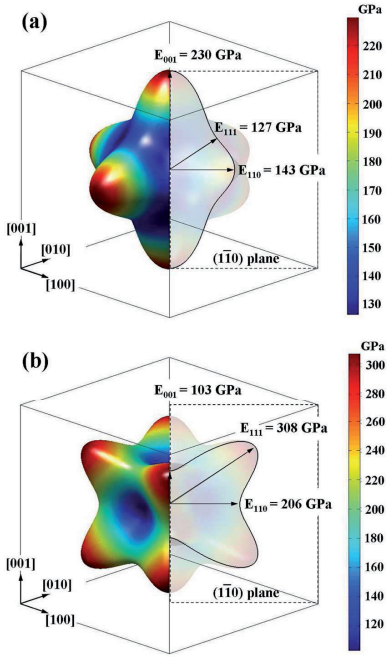

Figure 4.7 Directional dependence of the elastic modulus of (a) γ′-Fe_4N and (b) γ-Fe (Fe-15Ni-15Cr).

their structural similarity. Since γ′-Fe_4N is ferromagnetic while γ-Fe austenitic stainless steels are paramagnetic at room temperature, the difference in magnetic configuration between γ′-Fe_4N and γ-Fe austenitic stainless steels may be responsible for the decrease in stiffness associated with insertion of N into fcc γ-Fe. The dependence of the lattice volume on the magnetization is known as the magneto-volume effect [32, 33]. The volume expansion of γ′-Fe_4N due to its ferromagnetism may cause the reduction of elastic modulus compared to paramagnetic γ-Fe austenitic stainless steels.

Gressmann *et al*. have pointed out that γ-Fe austenitic stainless steels do not constitute a reliable reference for estimates of the elastic constants of γ′-Fe_4N due to the difference in elastic anisotropy [16]. The different directional dependencies of elastic modulus between γ′-Fe_4N and γ-Fe are illustrated in Figures 4.7(a) and (b) by three dimensional polar plots of the elastic modulus as a function of direction for γ′-Fe_4N and γ-Fe (Fe-15Ni-15Cr), which are derived from the elastic constants, C_{11}, C_{12}, and C_{44} given in Table 4.1 and reference [31], respectively. The intersectional plots on a (1$\bar{1}$0) plane provide the elastic modulus values along three major crystallographic axes of [001], [110], and [111]. For calculating the elastic modulus in an arbitrary direction in a cubic

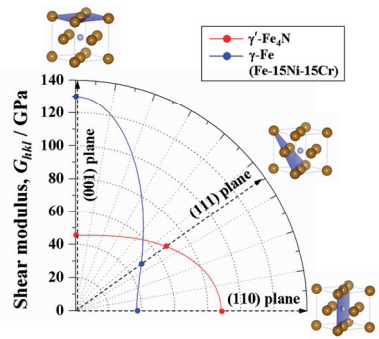

Figure 4.8 Shear plane orientation dependence of the shear modulus of γ'-Fe_4N and γ-Fe (Fe-15Ni-15Cr) along the shear direction of $[1\bar{1}0]$.

structure, the reader is referred to, for example, reference [34]. In the case of γ'-Fe_4N, the highest elastic modulus of 230 GPa is obtained along [001] while the lowest value of 127 GPa along [111]. In contrast, γ-Fe exhibits the highest elastic modulus of 308 GPa along [111] and the lowest of 103 GPa along [001]. The highest stiffness along the <100> direction in γ'-Fe_4N can be understood in terms of the formation of <100> directed Fe-N atomic bonding chains [16].

Besides the elastic modulus, the shear modulus anisotropy of γ'-Fe_4N and γ-Fe (Fe-15Ni-15Cr) is also studied. The shear modulus is of significance in plastic deformation of materials since it is linked to the strength and hardness of materials. For instance, the ideal shear strength of material is given to be proportional to its shear modulus. Figure 4.8 represents the shear modulus for γ'-Fe_4N and γ-Fe (Fe-15Ni-15Cr) as a function of orientation of shear planes along the fixed direction of $[1\bar{1}0]$. The shear modulus on a given shear plane and direction in a cubic structure can be calculated [34]. It can be seen that, for γ'-Fe_4N, the highest shear modulus of 88 GPa is obtained on $(110)[1\bar{1}0]$ while the lowest of 46 GPa on $(001)[1\bar{1}0]$. On the other side, γ-Fe exhibits the reverse shear modulus anisotropy, i.e., the highest of 130 GPa on $(001)[1\bar{1}0]$ and the lowest of 37 GPa on $(110)[1\bar{1}0]$, respectively. The highest shear modulus of γ'-Fe_4N on $(110)[1\bar{1}0]$ implies that γ'-Fe_4N is the strongest against the

shear deformation on (110)$[1\bar{1}0]$. The high shear strength of γ′-Fe_4N on (110) $[1\bar{1}0]$ has also been suggested by first principles stress–strain calculations performed previously [12]. For the discussion on the plastic deformation behavior, however, the shear modulus on (111)$[1\bar{1}0]$ appears to be most important, since {111} planes are common slip planes for dislocations in fcc metals. In fact, stacking faults and twins were observed typically on {111} planes of γ′-Fe_4N [35]. As can be seen in Figure 4.8, the shear modulus of γ′-Fe_4N on (111) $[1\bar{1}0]$ is 67 GPa while that of γ-Fe is 49 GPa. This implies that γ′-Fe_4N is intrinsically at least 1.4 times stronger than γ-Fe regarding plastic deformation. Actually, relatively high hardness values of 8 ± 1 GPa for both γ′-Fe_4N thin film and bulk sample were measured by nanoindentation. An even higher hardness value of 11.6 GPa has previously been reported [11]. Hence, the higher hardness, yet lower elastic modulus of γ′-Fe_4N compared to γ-Fe can be understood in terms of their shear modulus anisotropy. Based on this argument it can be understood why γ′-Fe_4N is performing well in applications for surface wear protection: Leyland and Matthews have identified a high hardness to elastic modulus ratio (*H/E*) to enable superior wear resistant performance [36].

4.4 Conclusions

The elastic properties of γ′-Fe_4N were studied experimentally and theoretically as the difference between calculated and measured literature data is up to 31%. The phase-pure γ′-Fe_4N thin film and bulk-like sample were synthesized, and the elastic moduli were probed by nanoindentation. The elastic moduli of γ′-Fe_4N thin film and bulk-like sample were determined to be 157 ± 11 GPa and 159 ± 17 GPa, respectively. The influence of porosity of γ′-Fe_4N bulk-like sample on the nanoindentation measurements was taken into account through the simultaneous determination and correction of the structural compliance. The measured elastic moduli were

in good agreement with the value of 162 GPa obtained by the *ab initio* calculations establishing the elastic modulus of γ′-Fe_4N. The hardness values of γ′-Fe_4N samples were measured to be 8 ± 1 GPa. The low elastic modulus but yet high hardness of γ′-Fe_4N compared to γ-Fe austenitic stainless steels can be understood in terms of their elastic anisotropy.

4.5 Appendix

Influence of surface roughness on the nanoindentation results

The surface roughness of the sample affects the results of nanoindentation measurements. Since the standard nanoindentation analysis assumes a perfectly flat sample surface, any surface irregularities give rise to measurement errors. In general, the errors become more significant when the indentation depth becomes comparable to a scale of the surface topographical features. It is therefore suggested that, for the indentation on metallic materials, the indentation depth should exceed the surface roughness R_a by a factor of 20 [EN ISO 14577-1]. A simple practical approach to minimize the roughness effect is to increase the indentation depth. This is however limited in a thin film study because of the possible influence of substrate [37]. There is therefore a common rule of thumb, the so-called 10% rule, that the indentation depth should not exceed 10% of the film thickness.

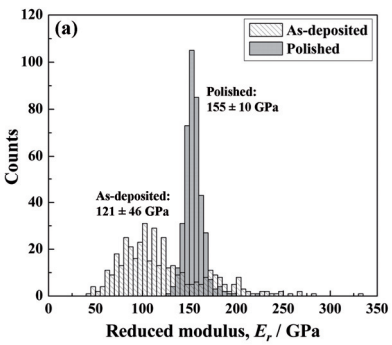

Figure 4.9 Distributions of nanoindentation results of (a) reduced modulus measured for γ′-Fe_4N thin film in as-deposited and after surface polished conditions.

Figure 4.9 demonstrates the influence of surface roughness on the nanoindentation results. The measurements were performed both on the as-deposited and the polished surfaces of the γ′-Fe_4N film.

For sufficient statistics, 400 indentations with a load of 2 mN were carried out for each condition. Most load-displacement data obtained from the as-deposited film were deviated largely from an ideal shape of the curve because of the surface roughness. Nevertheless, all the unloading curves measured were fitted by a power law function, and analyzed by the standard Oliver-Pharr method. As can be seen in Figure 4.9, the reduced moduli measured on the as-deposited film scatter largely, where the values range from 43 to 334 GPa. Although the data distribution appears to be a bimodal-like distribution with the maxima at about 100 and 175 GPa, a simple statistical analysis provides a mean value of 121 ± 46 GPa. On the other hand, data scattering can be significantly reduced by indentations on the polished surface, and the distribution becomes closer to a standard distribution with a mean value of 155 ± 10 GPa. It is interesting to note that the value of 155 GPa measured on the polished surface lies between the two maxima of 100 and 175 GPa identified from the measurements on the rough surface. These results clearly indicate that the surface roughness needs to be removed properly in order to obtain the correct mechanical property data by nanoindentation.

References

[1] J. Kübler, Phys. Lett. A 81 (1981) 81.
[2] P. Mohn, S.F. Matar, J. Magn. Magn. Mater. 191 (1999) 234.
[3] K. Tagawa, E. Kita, A. Tasaki, Jpn. J. Appl. Phys. 21 (1982) 1596.
[4] S.F. Matar, G. Demazeau, B. Siberchicot, IEEE Trans. Magn. 26 (1990) 60.
[5] A. Houben, P. Müller, J. von Appen, H. Lueken, R. Niewa, R. Dronskowski, Angew. Chem., Int. Ed. 44 (2005) 7212.
[6] M. Berg, C.V. Budtz-Jørgensen, H. Reitz, K.O. Schweitz, J. Chevallier, P. Kringhøj, J. Bøttiger, Surf. Coat. Technol. 124 (2000) 25.
[7] F.T. Hoffmann, P. Mayr, Nitriding and Nitrocarburizing, in: ASM Handbook: Friction, Lubrication and Wear Technology, ASM International, 1992, p. 878.
[8] F. Mahboubi, M. Samandi, D. Dunne, A. Bloyce, T. Bell, Surf. Coat. Technol. 71 (1995) 135.
[9] D. Music, J.M. Schneider, Appl. Phys. Lett. 88 (2006) 031914.

[10] E. Zhao, H. Xiang, J. Meng, Z. Wu, Chem. Phys. Lett. 449 (2007) 96.
[11] M.F. Yan, Y.Q. Wu, R.L. Liu, Appl. Surf. Sci. 255 (2009) 8902.
[12] J. Yang, H. Sun, C. Chen, Appl. Phys. Lett. 94 (2009) 151914.
[13] W. Schröter, A. Spengler, HTM, Haerterei-Tech. Mitt. 51 (1996) 356.
[14] S. Zheng, Y. Sun, A. Bloyce, T. Bell, Mater. Manuf. Processes 10 (1995) 815.
[15] A.I. Yurkova, A.V. Byakova, A.V. Belots'ky, Y.V. Milman, S.N. Dub, Mater. Sci. Forum 503-504 (2006) 645.
[16] T. Gressmann, M. Wohlschlögel, S. Shang, U. Welzel, A. Leineweber, E.J. Mittemeijer, Z.K. Liu, Acta Mater. 55 (2007) 5833.
[17] B. Predel: *Fe-N (Iron-Nitrogen)*. O.Madelung, (ed.). SpringerMaterials - The Landolt-Börnstein Database (http://www.springermaterials.com).
[18] J.F. Bobo, H. Chatbi, M. Vergnat, L. Hennet, O. Lenoble, P. Bauer, M. Piecuch, J. Appl. Phys. 77 (1995) 5309.
[19] C. Chang, J.M. Sivertsen, J.H. Judy, IEEE Trans. Magn. 23 (1987) 3636.
[20] H. Jacobs, D. Rechenbach, U. Zachwieja, J. Alloys Compd. 227 (1995) 10.
[21] W.C. Oliver, G.M. Pharr, J. Mater. Res. 7 (1992) 1564.
[22] G. Kresse, J. Hafner, Phys. Rev. B 48 (1993) 13115.
[23] G. Kresse, J. Hafner, Phys. Rev. B 49 (1994) 14251.
[24] G. Kresse, D. Joubert, Phys. Rev. B 59 (1999) 1758.
[25] H.J. Monkhorst, J.D. Pack, Phys. Rev. B 13 (1976) 5188.
[26] F. Birch, J. Geophys. Res. 83 (1978) 1257.
[27] M.J. Mehl, J.E. Osburn, D.A. Papaconstantopoulos, B.M. Klein, Phys. Rev. B 41 (1990) 10311.
[28] R. Hill, Proc. Phys. Soc., London, Sect. A 65 (1952) 349.
[29] O.L. Anderson, J. Phys. Chem. Solids 24 (1963) 909.
[30] W.F. Gale, T.C. Totemeier, Smithells Metals Reference Book (8th Edition), Elsevier, (2004).
[31] A. Teklu, H. Ledbetter, S. Kim, L.A. Boatner, M. McGuire, V. Keppens, Metall. Mater. Trans. A 35 (2004) 3149.
[32] M. Shiga, J. Phys. Soc. Jpn. 50 (1981) 2573.
[33] M. van Schilfgaarde, I.A. Abrikosov, B. Johansson, Nature 400 (1999) 46.
[34] M. Hayes, A. Shuvalov, Trans. ASME 65 (1998) 786.
[35] Z.Q. Liu, Z.K. Hei, D.X. Li, J. Mater. Res. 17 (2002) 2621.
[36] A. Leyland, A. Matthews, Wear, 246 (2000) 1.
[37] R. Saha, W.D. Nix, Acta Mater. 50 (2002) 23.

Chapter 5

γ′-$ZnFe_3N$ thin films: A proposal for a moderately ductile, corrosion protective coating on steel

5.1 Introduction

Iron nitride γ′-Fe_4N exhibits a simple crystal structure referred to as perovskite with the space group $Pm\bar{3}m$ and a lattice parameter of 0.37900(6) nm [1]. Figure 5.1 presents schematically all the atomic positions in the unit cell. In spite of its simple structure, γ′-Fe_4N exhibits a variety of exciting properties, and hence plays a technologically a significant role. For instance, γ′-Fe_4N is a common phase formed after surface nitriding of steel products to enhance their wear, fatigue, and corrosion resistant properties [2-4]. In addition, γ′-Fe_4N is ferromagnetic and hence a promising material for application as high density recording material due to its high saturation magnetization and low coercivity [5, 6].

It is known that a proportion of Fe atoms on Wyckoff positions 1*a* and/or 3*c* in γ′-Fe_4N can be substituted by other metallic elements, M, resulting in the chemical formula γ′-$M_xFe_{4-x}N$ (where *M* = Ni, Pd, Pt, Co, Mn, Cu, Zn, In, Ir, Rh, etc) [7-14]. So far, most of the experimental and theoretical studies on metallic substitutions have been devoted to improving the magnetic properties of γ′-$M_xFe_{4-x}N$ nitrides. As discussed above, γ′-Fe_4N is also widely employed as surface protective layer of nitrided steels in

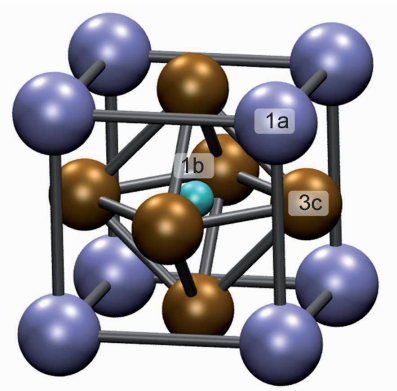

Figure 5.1 Unit cell of γ′-Fe_4N perovskite nitride. Fe (I), Fe (II), and N occupy 1*a*, 3*c* and 1*b* Wyckoff positions, respectively.

which its mechanical properties are the focus of interest. However, the data available on the mechanical properties of γ′-$M_xFe_{4-x}N$ are very limited.

This work focuses on the mechanical properties of the γ′-$ZnFe_3N$ phase. In the steel industry, for example, Zn-based coatings are extensively used for protection against corrosion of steel-sheet products for automobiles based on the galvanizing effect [15], while nitrided steel surfaces exhibit superior wear and corrosion resistance [2-4]. Hence, the materials design idea here is to substitute Zn for Fe in γ′-Fe_4N to improve the corrosion resistant performance while maintaining the favorable mechanical properties of Fe based perovskite nitrides [14]. However, the synthesis of γ′-$ZnFe_3N$ thin films has not previously been attempted, and the basic mechanical properties essential for structural applications are not known.

In this work, the elastic properties of γ′-$ZnFe_3N$ using *ab initio* calculations are studied. Furthermore, γ′-$ZnFe_3N$ thin films are synthesized both onto Si(100) and steel substrates by reactive magnetron sputtering, and the elastic properties and hardness are characterized by nanoindentation. Very good agreement between the measured and calculated elastic modulus of γ′-$ZnFe_3N$ are observed.

5.2 Methods

5.2.1 Theoretical methods

Ab initio calculations based on the density functional theory [16] were performed using the Vienna Ab initio Simulation Package (VASP) [17-19] including projector augmented wave potentials and the generalized-gradient approximation. The integration in the Brillouin zone was done on special *k*-points determined after Monkhorst–Pack [20]. A γ′-$ZnFe_3N$ unit cell consisting of five atoms (Zn at Wyckoff positions 1*a*, Fe at 3*c* and N at 1*b*, see Figure 5.1) was studied on a grid of 11 × 11 × 11 *k*-points with an

energy cut off of 500 eV. Spin polarization was considered since the ground state of γ'-$ZnFe_3N$ was suggested to be ferromagnetic [12]. The energy–volume curve obtained was fitted using the Birch–Murnaghan equation of states [21] to calculate the ground state lattice parameter, *a*, and the bulk modulus, *B*. Elastic constants of $C_{11} - C_{12}$ and C_{44} were calculated by applying an orthorhombic and monoclinic shear strain, respectively, which determines all three independent elastic constants for a cubic structure using the bulk modulus obtained [22]. The polycrystalline elastic modulus, *E*, and shear modulus, *G*, were obtained using the Hill's approximation scheme [23, 24]. The Poisson's ratio, ν, was calculated using a relation, $\nu = (3B - 2G)/(2(3B + G))$.

5.2.2 Thin film depositions and characterization

Fe-Zn-N thin films were deposited using a DC reactive magnetron sputtering technique. A Fe-Zn combined target, i.e. a few pieces of Zn plate were fixed on a Fe target with 50 mm in diameter, was sputtered at 30 W power under the Ar and N_2 gas mixture with the partial pressures of 0.5 and 0.1 Pa, respectively. The size of Zn plates was adjusted in such a way that a Fe to Zn composition ratio in the films is close to 3. Si(100) wafers with a diameter of 2 inches and polished ferritic steel plates (Fe-0.17C-1.4Mn wt.%) 10 mm × 10 mm × 1 mm in dimension were used as substrates. The target-substrate distance was 4 cm. The base pressure before depositions was 5×10^{-4} Pa. The substrate was placed on a Cu plate which was heated up to about 523 K prior to depositions. The depositions were carried out for 80 minutes, resulting in a film thickness of 1.4 μm.

The film composition was studied using energy dispersive X-ray spectroscopy (EDX, EDAX Genesis 2000) at an acceleration voltage of 18 kV. The film microstructure was investigated by scanning electron microscopy (SEM, JEOL JSM-6480). Structural analysis was performed by X-ray diffraction (XRD, Siemens D5000) in the Bragg–Brentano geometry

using a Cu-K_α source. The voltage and current settings were 40 kV and 40 mA, respectively. The film mechanical properties were investigated using nanoindentation (Hysitron TriboIndenter) with a Berkovich indenter tip. A simple loading-unloading function was applied with the maximum load of 2 mN. The load-displacement curves obtained were analyzed based on the method introduced by Oliver and Pharr [25].

5.3 Results and discussion

Table 5.1 contains the results of the *ab initio* calculations. The lattice parameter is calculated to be 0.3765 nm. Kuhnen *et al.* have synthesized γ′-$Zn_{0.6}Fe_{3.4}N$ powders by mechanical alloying, and determined its lattice parameter to be 0.3799 nm [12]. Although a single phase γ′-$ZnFe_3N$ was not obtained in their study, a lattice parameter of γ′-$ZnFe_3N$ was estimated to be about 0.3810 nm by a simple extrapolation from those of γ′-Fe_4N and γ′-$Zn_{0.6}Fe_{3.4}N$. Hence, the calculated value deviates by 1.2% from their experimental value. The elastic modulus of γ′-$ZnFe_3N$ is calculated to be 237 GPa. This value is comparable or slightly higher than that of ferritic steels, i.e. ~200 GPa [26]. It has been suggested that the ratio of bulk to shear modulus (B/G) represents a measure for ductile–brittle behavior with the crossover value of about 1.75 [27]. A B/G ratio > 1.75 is associated with ductility whereas a B/G ratio < 1.75 implies brittle behavior. According to the present calculation, the B/G of γ′-$ZnFe_3N$ is 2.27, indicating that γ′-$ZnFe_3N$ is ductile. However, this B/G value is lower than that of pure γ′-Fe_4N (B/G = 3.12 [28], 2.71 [29], 3.08 [30]) as reported previously, which implies that the Zn substitution in γ′-Fe_4N causes a reduction in ductility. Moreover, it has

a (nm)	C_{11} (GPa)	C_{12} (GPa)	C_{44} (GPa)	B (GPa)	E (GPa)	G (GPa)	ν
0.3765	340	141	85	207	237	91	0.31

Table 5.1 Calculated lattice parameter, a, elastic constants (C_{11}, C_{12}, and C_{44}), bulk modulus, B, elastic modulus, E, shear modulus, G, and Poisson's ratio, ν, for γ′-$ZnFe_3N$ perovskite nitride.

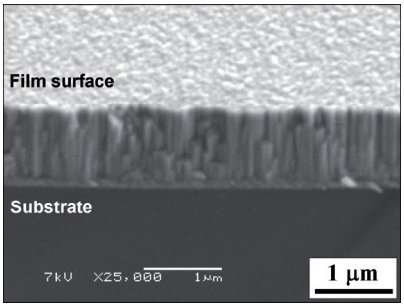

Figure 5.2 Cross-sectional SEM micrograph of γ′-$ZnFe_3N$ thin film deposited on Si(100) substrate.

been suggested that Cauchy pressure, $C_{12} - C_{44}$, could be used to describe the angular character of bonding in metals and compounds [31]. A more negative Cauchy pressure implies that the bonding is more directed or angular in character, while a positive Cauchy pressure gives rise to more metallic bonding. The present study shows a positive Cauchy pressure of 56 GPa for γ′-$ZnFe_3N$, implying that γ′-$ZnFe_3N$ is metallic in bonding character, and hence expected to be moderately ductile.

To validate the calculation results, γ′-$ZnFe_3N$ thin films were synthesized and their mechanical properties were measured. Based on EDX measurement, the film composition was determined to be 61.0 at.% Fe, 20.4 at.% Zn, and 18.6 at.% N, as a mean value of five measurements. This results in the chemical formula of $ZnFe_{2.99}N_{0.91}$, which is close to the stoichiometric composition of γ′-$ZnFe_3N$. Figure 5.2 shows a cross-sectional SEM micrograph of a film deposited on Si(100) substrate. The film exhibits a fine columnar grain structure with a column width of ~100 nm. No evidence for the formation of pores or cavities can be seen either at the surface or cross-section, indicating that the film is rather dense.

Figure 5.3(a) shows an XRD pattern for the film deposited on Si(100). Note that the diffraction intensity is given by logarithmic intensity. Apart from Si(100) substrate peaks, the diffractogram consists of a very strong peak at 2θ of around 41.0° and two minor peaks at around 47.7 ° and 88.9°. These peaks are believed to be associated with diffractions from (111), (200), and (222) planes for γ′-Fe_4N type perovskite phase. From the interplanar spacings for each diffraction plane detected, the lattice parameter was

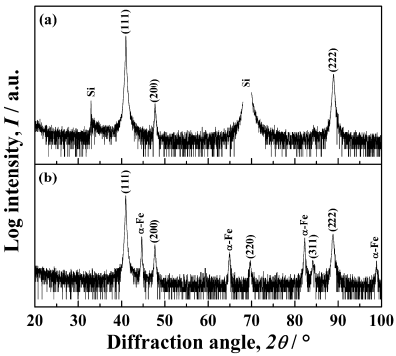

Figure 5.3 X-ray diffraction patterns for γ′-$ZnFe_3N$ thin films deposited on (a) Si(100) and (b) on steel substrate.

determined to be 0.381 nm, which is consistent with that suggested by Kuhnen *et al.* [12]. This experimental value is slightly larger than that of 0.379 nm reported for pure γ′-Fe_4N [1]. This slight increase in lattice parameter compared to γ′-Fe_4N is most probably due to Zn substitutions [12]. Hence, based on the diffractogram and composition analysis data, the formation of a single phase γ′-$ZnFe_3N$ during reactive magnetron sputtering exceeding the previously studied solubility limit [12] is inferred.

The strong diffraction intensities for the (111) and (222) planes indicate that the film deposited is textured. The film microstructure can therefore be characterized as (111) fiber texture. Because of the strong (111) fiber texture formation, some diffraction peaks are not detected in the Bragg–Brentano geometry. For instance, possible superlattice diffractions such as from (100) and (110) planes, which can be regarded as evidence for the ordered occupation of N at the body centered site and/or the ordered occupation of Zn atoms at the corner sites in the unit cell, are not seen in the diffractogram. To evaluate the presence of superlattice diffractions in the film deposited, the sample was also analyzed supplementary using another diffractometer with a Cu-K_α X-ray source (Bruker D8 GADDS) equipped with an areal detector and a tilt function on a sample stage. We could detect at least a trace of (110) superlattice diffraction at around 33.2° measured under an appropriate sample tilt. This fact supports, at least partially, the ordered occupation of N and/or Zn atoms to form the γ′-$ZnFe_3N$ structure. Most probably, N occupies the 1*b* site and Zn 1*a* site as

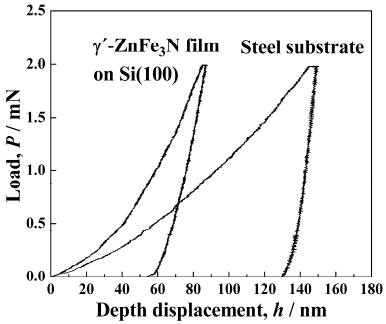

Figure 5.4 Nanoindentation load-displacement curves for γ′-$ZnFe_3N$ thin film deposited on Si(100) and for steel substrate.

suggested previously [12]. We have also deposited γ′-$ZnFe_3N$ thin films on steel substrates, see Figure 5.3(b). Apart from α-Fe peaks from the substrate, all peaks detected can be associated with γ′-$ZnFe_3N$ phase. Hence, the formation of a single phase γ′-$ZnFe_3N$ is confirmed also on steel substrates without the formation of other Fe-Zn intermetallic reaction products.

The elastic modulus and hardness of γ′-$ZnFe_3N$ films were studied by nanoindentation. Figure 5.4 shows an example of load-displacement curves obtained from γ′-$ZnFe_3N$ films on Si(100). A load-displacement curve measured directly on the steel substrate is also included for comparison. At the applied load of 2 mN, the maximum indentation depth for the γ′-$ZnFe_3N$ film amounts to < 100 nm which is still less than one-tenth of the film thickness, 1.4 μm, and hence the influence of substrate on the measured results is expected to be minimal. Based on 25 indentations, the reduced modulus, E_r, for γ′-$ZnFe_3N$ films on Si(100) was determined to be 218 ± 16 GPa. When the calculated Poisson's ratio of 0.31 is employed, the elastic modulus of γ′-$ZnFe_3N$ derived is 244 ± 22 GPa. This value deviates by only 3% from the calculated value, see Table 5.1, which confirms a good agreement between the *ab initio* calculation and the experiment. In addition, similar values of elastic modulus of 259 ± 35 GPa were measured for the films deposited on steel substrate. The hardness values of γ′-$ZnFe_3N$ films deposited were measured to be 12 ± 2 GPa, which can be compared to a hardness of 11.6 GPa for γ′-Fe_4N as previously reported [28]. For comparison, the hardness of the steel substrate used was measured to be

3.5 ± 0.3 GPa. Hence, the γ′-$ZnFe_3N$ could potentially be utilized for hard coating applications. The measured hardness values of γ′-$ZnFe_3N$ films are also comparable to surface hardness for plasma nitrided austenitic stainless steels (700-1200 HV) [32], surface hardness for plasma carburized steels (~900 HV) [33], and so-called MAX-phase Cr_2AlC thin films (~13 GPa) [34], the application of which has also been proposed as a protective coating for steels [35]. With this work, we hope to inspire others to evaluate the corrosion properties of γ′-$ZnFe_3N$ films on steel products.

5.4 Conclusions

Based on the materials design idea to substitute Zn for Fe in γ′-Fe_4N to improve the corrosion performance while maintaining the favorable mechanical properties, γ′-$ZnFe_3N$ thin films were synthesized on Si(100) as well as on steel substrates. The elastic modulus and hardness of γ′-$ZnFe_3N$ films are determined by nanoindentation to be 244 ± 22 GPa and 12 ± 2 GPa, respectively. The measured elastic modulus deviates by 3% from the *ab initio* calculation result. Based on the calculated bulk to shear modulus ratio of 2.27 and positive Cauchy pressure ($C_{12} - C_{44}$) of 56 GPa, γ′-$ZnFe_3N$ is suggested to be moderately ductile. The application of γ′-$ZnFe_3N$ as a corrosion protective coating on steels is considered to be promising.

References

[1] H. Jacobs, D. Rechenbach, U. Zachwieja, J. Alloys Compd. 227 (1995) 10.
[2] F.T. Hoffmann, P. Mayr, Nitriding and Nitrocarburizing, in: ASM Handbook: Friction, Lubrication and Wear Technology, ASM International, 1992, p. 878.
[3] M. Berg, C.V. Budtz-Jørgensen, H. Reitz, K.O. Schweitz, J. Chevallier, P. Kringhøj, J. Bøttiger, Surf. Coat. Technol. 124 (2000) 25.
[4] F. Mahboubi, M. Samandi, D. Dunne, A. Bloyce, T. Bell, Surf. Coat. Technol. 71 (1995) 135.
[5] K. Tagawa, E. Kita, A. Tasaki, Jpn. J. Appl. Phys. 21 (1982) 1596.
[6] S.F. Matar, G. Demazeau, B. Siberchicot, IEEE Trans. Magn. 26 (1990) 60.

[7] G.W. Wiener, J.A. Berger, J. Met. 7 (1955) 360.
[8] H.H. Stadelmaier, A.C. Fraker, Trans. Metall. Soc. AIME 218 (1960) 571.
[9] S. Matar, L. Fournes, S. Cherubin-Jeannette and G. Demazeau, Eur. J. Solid State Inorg. Chem. 30 (1993) 871.
[10] B. Siberchicot, S.F. Matar, L. Fournes, G. Demazeau, P. Hagenmuller, J. Solid State Chem. 84 (1990) 10.
[11] R.S. de Figueiredo, J. Foct, A.V. dos Santos, C.A. Kuhnen, J. Alloys Compd. 315 (2001) 42.
[12] C.A. Kuhnen, R.S. de Figueiredo, A.V. dos Santos, J. Magn. Magn. Mater. 219 (2000) 58.
[13] J. von Appen, R. Dronskowski, Angew. Chem. Int. Ed. 44 (2005) 1205.
[14] D. Music, J.M. Schneider, Appl. Phys. Lett. 88 (2006) 031914.
[15] A.R. Marder, Prog. Mater. Sci. 45 (2000) 191.
[16] P. Hohenberg, W. Kohn, Phys. Rev. B 136 (1964) 864.
[17] G. Kresse, J. Hafner, Phys. Rev. B 48 (1993) 13115.
[18] G. Kresse, J. Hafner, Phys. Rev. B 49 (1994) 14251.
[19] G. Kresse, D. Joubert, Phys. Rev. B 59 (1999) 1758.
[20] H.J. Monkhorst, J.D. Pack, Phys. Rev. B 13 (1976) 5188.
[21] F. Birch, J. Geophys. Res. 83 (1978) 1257.
[22] M.J. Mehl, J.E. Osburn, D.A. Papaconstantopoulos, B.M. Klein, Phys. Rev. B 41 (1990) 10311.
[23] R. Hill, Proc. Phys. Soc., London, Sect. A 65 (1952) 349.
[24] O.L. Anderson, J. Phys. Chem. Solids 24 (1963) 909.
[25] W.C. Oliver, G.M. Pharr, J. Mater. Res. 7 (1992) 1564.
[26] S.A. Kim, W.L. Johnson, Mater. Sci. Eng. A 452-453 (2007) 633.
[27] S.F. Pugh, Philos. Mag. 45 (1954) 823.
[28] M.F. Yan, Y.Q. Wu, R.L. Liu, Appl. Surf. Sci. 255 (2009) 8902.
[29] E. Zhao, H. Xiang, J. Meng, Z. Wu, Chem. Phys. Lett. 449 (2007) 96.
[30] T. Gressmann, M. Wohlschlögel, S. Shang, U. Welzel, A. Leineweber, E.J. Mittemeijer, Z.-K. Liu, Acta Mater. 55 (2007) 5833.
[31] D.G. Pettifor, Mater. Sci. Technol. 8 (1992) 345.
[32] S.-P. Hannula, P. Nenonen, J.-P. Hirvonen, Thin Solid Films 181 (1989) 343.
[33] J.M. Baek, Y.R. Cho, D.J. Kim, K.H. Lee, Surf. Coat. Technol. 131 (2000) 568.
[34] J.M. Schneider, D.P. Sigumonrong, D. Music, C. Walter, J. Emmerlich, R. Iskandar, J. Mayer, Scr. Mater. 57 (2007) 1137.
[35] C. Walter, D.P. Sigumonrong, T. El-Raghy, J.M. Schneider, Thin Solid Films 515 (2006) 389.

Chapter 6

Synthesis and elastic properties of perovskite $Pd_xFe_{4-x}N$ thin films

6.1 Introduction

A fraction of Fe in perovskite Fe_4N (space group $Pm\bar{3}m$) can be replaced by Pd, resulting in the formation of $PdFe_3N$, where Pd is positioned at the cube corner sites, Fe at the face centered sites, and N occupies the body centered sites, respectively [1, 2]. In spite of this crystallographically simple structure, $PdFe_3N$ exhibits exciting physical and chemical properties. $PdFe_3N$ is a ferromagnetic compound with the Curie temperature of about 600 K [3], and is potentially valuable material for magnetic recording applications [2, 4, 5]. The decomposition temperature of $PdFe_3N$ is above 1000 K [3], which is considerably higher than the isostructural ternary nitrides $RhFe_3N$ (~800 K) [6] and $GaFe_3N$ (~810 K) [7]. A*b initio* data suggest that $PdFe_3N$ may behave ductile upon mechanical loading due to its high bulk modulus to C_{44} ratio [8]. This further raises the attractiveness of $PdFe_3N$ for magnetic material applications. However, no experimental data on the elastic properties of $PdFe_3N$ are available in literature. Furthermore, in the case of Pd substitution in Fe_4N, a continuous solubility of Pd between Fe_4N and $PdFe_3N$ has previously been reported, resulting in the formation of single phase $Pd_xFe_{4-x}N$ compounds, where x ranges from 0 and 1 [1]. Accordingly, the resulting elastic properties may be affected by local Pd composition variations.

The purpose of the present study is to explore the mechanical properties, in particular, the elasticity of $PdFe_3N$. The influence of local Pd composition variations on the elastic properties is also studied systematically using the combinatorial thin film approach. The

experimentally determined elastic properties by nanoindentation are compared to *ab initio* calculations.

6.2 Thin film depositions and characterization

$Pd_xFe_{4-x}N$ thin films were deposited using a combinatorial reactive magnetron sputtering technique. A schematic illustration of the deposition set-up is shown in Figure 6.1. Pure elemental Fe and Pd targets (50 mm in diameter) were co-sputtered using the Ar and N_2 gas mixture with the partial pressures of 0.40 and 0.27 Pa, respectively. The sputtering powers for the Fe and Pd targets were kept at 150 and 15 W, respectively. The Pd/Fe composition ratios in deposited films were adjusted by limiting the amount of Pd flux using a rotatable shutter installed at the front of the Pd target as schematically illustrated in Figure 6.1. A Si(100) wafer with a diameter of 2 inches was used as a substrate, and heated at about 623 K during depositions. The targets–substrate distance was about 10 cm. The deposition chamber was evacuated down to 10^{-5} Pa prior to depositions. The compositionally homogeneous films were deposited with substrate rotation whereas the films with composition gradient, i.e., combinatorial films, were prepared without substrate rotation. The depositions for 2 hours resulted in the film thickness of approximately 1.8 μm.

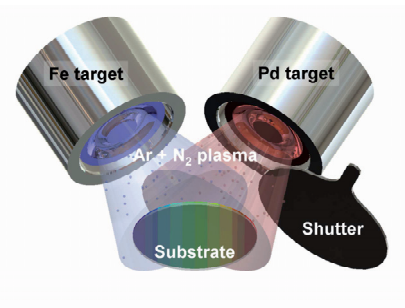

Figure 6.1 Schematic illustration for the experimental setup for the deposition of $Pd_xFe_{4-x}N$ thin films.

The film morphology and composition were investigated by scanning electron microscopy (SEM, JEOL JSM-6480) and energy dispersive X-ray spectroscopy (EDX, EDAX Genesis 2000), respectively. The EDX measurements were performed at a beam acceleration voltage of 15 kV. Fe, Pd, and N were included for quantification. The

crystallographic structures of the homogeneous films were analyzed by X-ray diffraction (XRD, Siemens D5000) with Cu-K_α radiation under the Bragg–Brentano geometry whereas the combinatorial films were investigated using a micro-beam XRD (Cu-K_α) system (Bruker D8 GADDS) with a beam collimator diameter of 0.5 mm under a fixed incident beam angle of 20°. In both diffraction systems, the volt age and current settings of the X-ray generators were 40 kV and 40 mA, respectively. The film mechanical properties were studied by nanoindentation (Hysitron TriboIndenter) using a Berkovich indenter tip. The load–displacement curves were recorded with a load of up to 2.5 mN. The reduced modulus was determined based on the standard analytical method [9]. In order to minimize the influence of surface roughness on the nanoindentation measurements, the film surface was polished prior to indentations.

6.3 Results and discussion

Figure 6.2 shows XRD patterns for the compositionally homogeneous $Pd_xFe_{4-x}N$ thin films deposited with varied Pd/(Fe+Pd) atomic ratios of (a) 0, (b) 0.104, (c) 0.212, and (d) 0.236. The ratio of 0.25 corresponds to the ideal composition of $PdFe_3N$. The N contents in these films, i.e. N/(Fe+Pd+N) at.%, were measured to be within 19–21 at.%. This is very close to 20 at.% expected for $Pd_xFe_{4-x}N$ compounds. Consequently, the chemical compositions of the films in Figure 6.2(a) and (d) are very close to stoichiometric Fe_4N and $PdFe_3N$, respectively. The diffraction patterns presented are all related to the

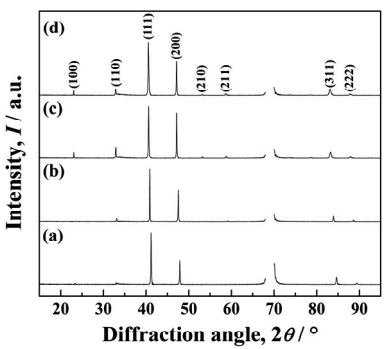

Figure 6.2 XRD patterns for the compositionally homogeneous $Pd_xFe_{4-x}N$ thin films with different Pd/(Fe+Pd) ratios: (a) 0, (b) 0.104, (c) 0.212, and (d) 0.236.

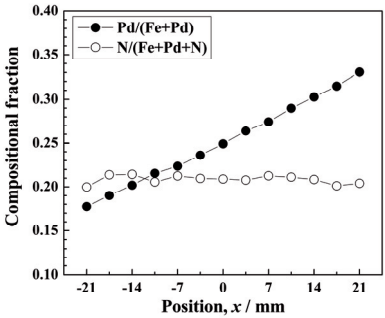

Figure 6.3 Lateral compositional gradients measured on combinatorial $Pd_xFe_{4-x}N$ film.

perovskite Fe_4N structure as the indexed diffraction planes. No evidence for the formation of other phases can be seen in the diffractograms, indicating that the films are phase pure. The presence of superlattice diffractions such as (100) and (110) is at least in part, consistent with ordered occupations of N and/or Pd at the respective positions in the unit cell. Namely, N atoms tend to be located at the body centered sites of the cell whereas Pd populates the cube corner sites.

In addition to compositionally homogeneous films, combinatorial thin films were deposited. Figure 6.3 illustrates the lateral compositional gradient produced on a combinatorial $Pd_xFe_{4-x}N$ film. Within a distance of 42 mm on the substrate, a continuous linear variation of Pd/(Fe+Pd) between 0.177 and 0.330 is obtained. Again, the ratio of 0.25 is consistent with the ideal composition of $PdFe_3N$. It should be noted that the N content is almost constant at about 20 at.% irrespective of the position along the Pd concentration gradient (Figure 6.3). This allows us to investigate systematically the effect of the Pd content variation on the properties of $Pd_xFe_{4-x}N$. In the present work, a combinatorial film with lower Pd/(Fe+Pd) ratios of 0.128–0.237 was also deposited. According to the micro-beam XRD measurements on these combinatorial films, the diffraction peaks detected for different Pd contents were all consistent with the perovskite Fe_4N. Similar to the results in Figure 6.2, no evidence for the formation of additional phases was identified even for the samples exhibiting Pd/(Fe+Pd) > 0.25, namely $x > 1$ in $Pd_xFe_{4-x}N$.

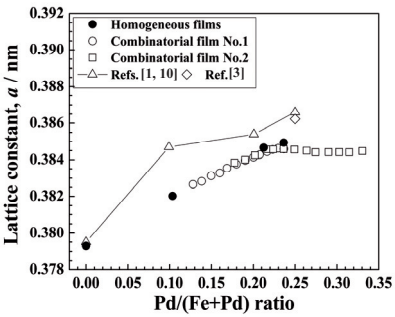

Figure 6.4 Change in lattice parameter of $Pd_xFe_{4-x}N$ films as a function of Pd content in comparison to literature data.

Figure 6.4 gives the change in lattice constant as a function of Pd content in the $Pd_xFe_{4-x}N$ films. The lattice parameters were evaluated from (111) and (200) *d*-spacings, and the averaged values thereof are presented here. The literature data for powder samples [1, 3, 10] are also included for comparison. A lattice constant of binary Fe_4N film is determined to be 0.3793 nm. This is consistent with literature data [10, 11]. The lattice constant increases linearly with increasing the Pd content up to a Pd/(Fe+Pd) ratio of about 0.25. This systematic increase in lattice constant with Pd is mainly caused by the Pd substitution in the lattice of perovskite Fe_4N. In the present thin film study, a lattice parameter of about 0.385 nm is obtained for the composition close to $PdFe_3N$. This is 0.3–0.4% smaller than those of powder samples reported previously [1, 3]. Similarly, the Pd containing $Pd_xFe_{4-x}N$ films with $x < 1$ exhibit smaller lattice constants compared to those for powder samples. The reason for these differences in lattice constants between thin films and powder samples of $Pd_xFe_{4-x}N$ is still unknown. As discussed later, this may be related to a difference in the magnetic states.

It is also interesting to notice that the lattice constant levels off at a Pd/(Fe+Pd) ratio of about 0.25, and it remains almost unchanged with the further increase in Pd content. This may be associated with the effect of atomic ordering in the lattice. For instance, it has been reported in Fe-Al binary alloys that ordering gives rise to a reduction in lattice constant [12]. The constant lattice parameter for $x > 0.25$ may also be related to a solubility limit of Pd in $Pd_xFe_{4-x}N$. However the present XRD measurements

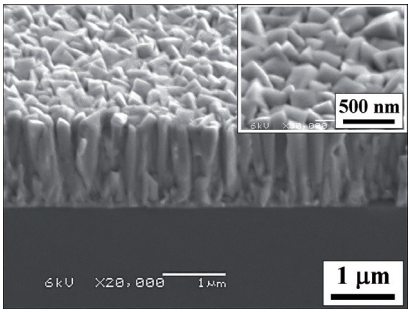

Figure 6.5 SEM micrograph showing cross-sectional feature of $PdFe_3N$ thin film.

did not reveal indications for the formation of other crystalline phases. Nevertheless, it might be the case that the volume fraction of additional phases, if they exist, was too small to be detected by the present measurement setup and/or they were just amorphous.

Figure 6.5 shows a cross-sectional SEM micrograph for the $PdFe_3N$ film, the corresponding XRD pattern of which is shown in Figure 6.2(d). The film microstructure consists of columnar grains with a column width of 200–300 nm. The film growth exhibiting a columnar structure is very common in sputter depositions. The inset figure emphasizes a surface topographical feature in as-deposited condition. The as-deposited film surface appears to be quite rough, which is most probably attributed to the evolution of crystallographic faceting during film growth process. Such a rough surface topographical feature often induces large systematic and statistical errors in nanoindentation measurements especially when an indentation penetration depth is comparable to a characteristic surface height variation. Hence, in the present work, the film surface was polished prior to nanoindentation, reducing the surface roughness of the as-deposited thin films.

Figure 6.6 summarizes the reduced moduli measured by nanoindentation on the $Pd_xFe_{4-x}N$ films. 20 indentations were performed on each sample. The maximum indentation penetration depths were about 110 nm, which corresponds to less than 10% of the film thickness. The reduced moduli of the Fe_4N and $PdFe_3N$ films were measured to be 147 ± 4 GPa and 162 ± 11 GPa, respectively, implying that the Pd substitution causes a slight increase in stiffness. In the previously published *ab initio* calculations,

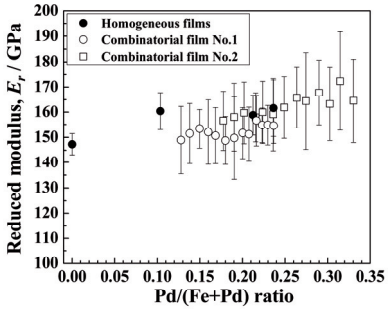

Figure 6.6 Change in reduced modulus as a function of Pd content in $Pd_xFe_{4-x}N$ films.

the polycrystalline elastic modulus and Poisson's ratio of $PdFe_3N$ are not discussed. In order to compare the experiment and theory, the elastic modulus of $PdFe_3N$ was also calculated here. The calculation method employed was essentially the same as already described in Chapter 4 for Fe_4N or Chapter 5 for $ZnFe_3N$, and the results are shown in Table 6.1. Based on the nanoindentation results, the experimental elastic modulus for the $PdFe_3N$ film is determined to be 170 ± 14 GPa if a calculated Poisson's ratio of 0.31 is employed. On the other hand, the *ab initio* calculations predict the elastic modulus of 225 GPa for $PdFe_3N$ which is 32% higher than the present nanoindentation results. A good agreement between experiment and theory has been obtained for Fe_4N (Chapter 4) as well as $ZnFe_3N$ (Chapter 5). The reason for the relatively large discrepancy between the experiment and theory on the elasticity for $PdFe_3N$ is unknown. Coupling between magnetism and equilibrium volume, and hence elastic stiffness, is known as the magneto-volume effect [13, 14]. Although $PdFe_3N$ is considered to be ferromagnetic at room temperature, the metastable magnetic configurations of $PdFe_3N$ thin films might be quenched during kinetically limited thin film growth, which in turn might result in a discrepancy of the elastic modulus between the experiment and theory. As presented earlier, the lattice constants measured for the $Pd_xFe_{4-x}N$ films are smaller than literature data.

a (nm)	C_{11} (GPa)	C_{12} (GPa)	C_{44} (GPa)	B (GPa)	E (GPa)	G (GPa)	ν
0.3861	324	127	79	193	225	86	0.31

Table 6.1 Calculated lattice parameter, a, elastic constants (C_{11}, C_{12}, and C_{44}), bulk modulus, B, elastic modulus, E, shear modulus, G, and Poisson's ratio, ν, for $PdFe_3N$.

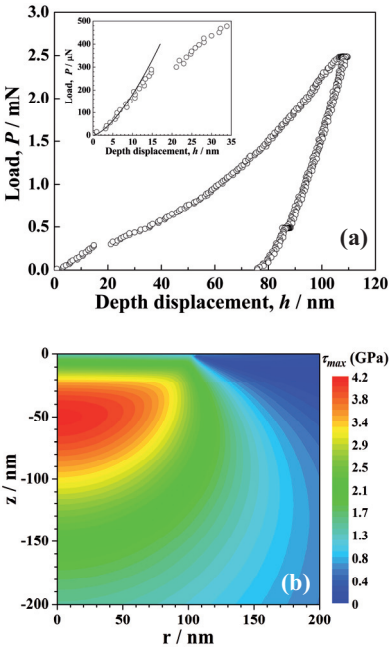

Figure 6.7 (a) Nanoindentation load–displacement curve obtain from the $PdFe_3N$ thin film. The inset figure emphasizes a pop-in event during loading. Calculated Hertzian curve (solid line) is also included. (b) Distribution of local maximum shear stress calculated for the critical load.

This difference in lattice constants might also be an indication of possible modification of the magnetic ordering in the $Pd_xFe_{4-x}N$ films deposited in the present work. For better understating, a more systematic study on the correlation between magnetic and elastic properties of the $Pd_xFe_{4-x}N$ films is required. Furthermore, any microstructural effects such as density, column/grain-boundaries, texture, etc, of the deposited films on the nanoindentation results may need to be taken into account as well.

In addition to the standard nanoindentation analysis, the onset of plasticity of the $PdFe_3N$ film during loading is also evaluated based on the Hertz elastic contact theory. The basic theory of the analytical method is introduced in Chapter 2, Section 2.4.3.2. The tip radius used was ~760 nm. Figure 6.7(a) presents an example of the nanoindentation load–displacement curves obtained from the $PdFe_3N$ film. The inset figure provides an initial portion of the loading stage including a calculated curve according to the Hertz contact theory. There is a clear pop-in event observed at a load of about 300 μN, which is related to the onset of plasticity. Below this critical load, the experimental data agree well to the Hertzian curve, indicating that the deformation is completely elastic up to

this load. The spatial distribution of the local maximum shear stress calculated at this critical indentation load is illustrated in Figure 6.7(b). In this case, the maximum shear stress developed within an indented volume amounts to 4.1 GPa. Similar analysis including more data for statistics gives the values of 4.2 ± 0.7 GPa for the $PdFe_3N$ and 3.3 ± 0.4 GPa for the Fe_4N film. It has been suggested that the maximum shear stress determined at the onset of plasticity during nanoindentation are associated with the homogeneous nucleation of dislocations [15, 16], and close to the ideal shear strength of material, ~*G*/10, where *G* is the shear modulus. The critical shear stress for the $PdFe_3N$ film is increased by 27% compared to Fe_4N, implying that the Pd substitution gives rise to the increase in the intrinsic resistance against dislocation nucleation upon mechanical loading. The possible increase in elastic modulus, hence shear modulus, by the Pd substitution may in part be responsible for the increased critical shear stress. Also, as already discussed in Chapter 3, the critical shear stress obtained by nanoindentation may be used to discuss the ductile–brittle behavior of materials. The critical shear stress for the $PdFe_3N$ films in the present work is comparable to or even lower than typical ductile materials such as for Al, Au, Ag, Cu, Ta, Ni, and Fe/steel, and hence $PdFe_3N$ is expected to be also ductile. This is consistent with the prediction from *ab initio* calculations about the possible ductility of $PdFe_3N$ [8].

6.4 Conclusions

In this study, phase pure perovskite $Pd_xFe_{4-x}N$ thin films were successfully deposited using combinatorial reactive magnetron sputtering, and the mechanical properties thereof were probed by nanoindentation. The elastic modulus of the $PdFe_3N$ film was determined to be 170 ± 14 GPa. On the other side, the *ab initio* calculation gave the value of 225 GPa. Based on the systematic study using the combinatorial $Pd_xFe_{4-x}N$ thin films, the influence of Pd content on the elastic modulus was found to be small.

$PdFe_3N$ was suggested to be ductile based on the measurements of the critical shear stress for the onset of plastic deformation.

References

[1] H.H. Stadelmaier, A.C. Fraker, Trans. Metall. Soc. AIME 218 (*1960*) 571.
[2] P. Mohn, K. Schwarz, S. Matar, G. Demazeau, Phys. Rev. B 45 (1992) 4000.
[3] D. Music, J. Burghaus, T. Takahashi, R. Dronskowski, J.M. Schneider, Eur. Phys. J. B 77 (2010) 401.
[4] J. von Appen, R. Dronskowski, Angew. Chem., Int. Ed. 44 (2005) 1205.
[5] C.A. Kuhnen, A.V. dos Santos, J. Alloys Compd. 297 (2000) 68.
[6] A. Houben, P. Müller, J. von Appen, H. Lueken, R. Niewa, R. Dronskowski, Angew. Chem., Int. Ed. 44 (2005) 7212.
[7] A. Houben, J. Burghaus, R. Dronskowski, Chem. Mater. 21 (2009) 4332.
[8] D. Music, J.M. Schneider, Appl. Phys. Lett. 88 (2006) 031914.
[9] W.C. Oliver, G.M. Pharr, J. Mater. Res. 7 (1992) 1564.
[10] G.W. Wiener, J.A. Berger, J. Met. 7 (1955) 360.
[11] H. Jacobs, D. Rechenbach, U. Zachwieja, J. Alloys Compd. 227 (1995) 10.
[12] R.A. Buckley, S. Kaviani, Mater. Sci. Eng. A 258 (1998) 173.
[13] M. van Schilfgaarde, I.A. Abrikosov, B. Johansson, Nature 400 (1999) 46.
[14] M. Shiga, J. Phys. Soc. Jpn. 50 (1981) 2573.
[15] D. Lorenz, A. Zeckzer, U. Hilpert, P. Grau, H. Johansen, H.S. Leipner, Phys. Rev. B 67 (2003) 172101.
[16] D.F. Bahr, D.E. Kramer, W.W. Gerberich, Acta Mater. 46 (1998) 3605.

Chapter 7

Spontaneous whisker growth from thin films containing soft metal and rare earth element

7.1 Introduction

One-dimensional nanostructured materials also referred to as nanowires, nanorods, and nanowhiskers are known to exhibit unique physical and chemical properties compared to three-dimensional bulk materials. The attractive properties of nanowires provide many potential applications as novel functional nanodevices [1, 2]. While many different synthesis techniques for self-organized nanowires have been reported such as Vapor-Liquid-Solid (VLS) method [3], solution method [4, 5], laser ablation [6, 7], and thermal evaporation [8, 9], the development of new synthesis concepts and techniques for nanowires with well-controlled morphology, growth rate, size, crystallinity, and chemistry is a challenging task.

Nanowires may be classified into two groups based on their growth behavior. Firstly, wires growing from their tips, the wire forming species are supplied from vapor and/or liquid phase surrounding. One-dimensional growth in this case is most commonly facilitated through confinement by a liquid droplet. Most synthesis techniques reported so far utilize this mechanism. Secondly, wires are also formed by growth from the roots. A well-known example is the spontaneous formation of soft metal (SM) whiskers such as Sn, Cd, and Zn used for electroplating materials for electronic components [10-12]. Although the SM-whisker growth mechanism has not been fully understood yet, it is generally accepted that a major driving force for the growth of SM-whiskers is related to compressive stresses developed in SM base matrices [11, 13-15]. Namely, SM can be extruded out of the surface in the form of whiskers to release the compressive stresses caused by intrinsic (e.g. residual stress related to

material processing, impurities, microstructural defects, and intermetallic formation) and/or extrinsic reasons (e.g. external stress and oxidation, etc). Previously, the stress-induced whisker growth has been recognized as a possible synthesis technique of one-dimensional nanostructured materials. Shim *et al.* have reported the growth of Bi-nanowires on as-sputtered films after thermal annealing, which was facilitated by the relaxation of thermal stress developed due to a mismatch of thermal expansion between the film and substrate [16]. Saka *et al.* have reported rapid growth of Cu nanowhiskers on evaporated polycrystalline Cu films with the aid of local stress gradients in the film [17]. Cheng *et al.* have proposed a method of fabricating Bi nanowires from the surfaces of sputtered Bi-CrN composite thin films where the driving force for the Bi-nanowire formation was reported to be the high compressive residual stress in these composite films [18]. The spontaneous formation of SM-whiskers from the surfaces of SM containing ternary carbide and nitride bulk samples has been observed [19]. The whisker growth was attributed to the compressive stresses originating within the samples due to the volume expansion associated with the oxidation of SM.

Recently, rapid spontaneous Sn-whisker growth has been reported in Sn-solder alloys containing rare earth (RE) elements [20-24]. The addition of RE elements was argued to lead to the formation of $RESn_3$ intermetallic phases such as $LaSn_3$, $CeSn_3$, and YSn_3 within Sn matrix phases. The driving force for rapid Sn-whisker growth was considered to be related to the compressive stresses developed due to preferential oxidation of RE elements in $RESn_3$ phases under atmosphere exposure. The preferential oxidation of RE elements of $RESn_3$ phases resulted in the formation of RE element rich oxide layers by leaving pure Sn. Such a reaction is accompanied by large volume expansions, and hence compressive stresses built up in a confined volume, which eventually acted as the driving force for extrusion of Sn-whiskers. Similarly, rapid spontaneous SM-whisker

growth has been reported in bulk compounds of $NdSn_3$, $NdIn_3$, and $LaPb_3$ [25, 26]. The formation of $RE(OH)_3$ compounds was identified after exposure to atmosphere instead of simple RE-oxides.

The growth rates of Sn-whiskers from $RESn_3$ were reported to be ~10 Å/s [22, 26], which are two to three orders of magnitude higher than those observed for Sn whisker extrusion during Sn plating applications (e.g. 0.2-0.4 Å/s [27, 28]). Moreover, those whiskers can be formed on the sample surface spontaneously just upon exposure to atmosphere. This is attractive from a view point of submicron/nanostructure engineering although the SM whisker formation has commonly been considered to be detrimental because of the potential risk for electrical short cut, and hence damaging components. The stress induced whisker extrusion from $RESM_3$ compounds could potentially be utilized as a novel synthesis route for the rapid fabrication of self-organized one-dimensional submicron/nanostructured materials.

Among many possible combinations of SM-RE systems, the In-Y binary system is one of the candidates of material systems to be studied since the intermetallic compound YIn_3 is thermodynamically stable [29], and therefore expected to provide rapid spontaneous In-whiskering similar to Sn-whisker formation reported previously from Sn-solder alloys. Although the possible application of pure In-whiskers seems to be limited in practice, its oxide In_2O_3 is known to be a wide band gap transparent semiconductor, and hence In_2O_3 nanowires have many potential applications such as for gas-sensors and ultraviolet photodetectors [30].

Herein the spontaneous growth behavior of In-whiskers from YIn_3 thin films deposited by combinatorial magnetron sputtering is reported. The analysis of morphology and extrusion kinetics along the Y/In concentration gradient of the compositionally graded thin films enables an efficient investigation of the composition dependence of whisker extrusion morphology and kinetics. Only within ~7 at.% spread in

composition, we find the In-whisker diameter ranging from ~0.2 to a few μm or even larger. Occasionally, a growth rate of In-whiskers as high as ~1500 Å/s is observed, which is even two orders of magnitude larger than rapid Sn-whisker formation from $RESn_3$ phases reported previously [22, 26]. Based on these experimental observations, an alternative synthesis pathway for the growth of one-dimensional submicron/nanostructures is suggested, where whisker morphology and growth kinetics are controlled by the film composition.

7.2 Experimental methods

Compositionally graded In-Y thin films were deposited using the combinatorial magnetron sputtering platform (as presented in Figure 2.11) schematically shown in Figure 7.1. Two magnetron cathodes equipped with In and Y targets of 39 mm in diameter were placed facing the substrate at an angle of approximately 15° with respect to the substrate normal. The target-substrate distance was approximately 6 cm. The deposition chamber was evacuated prior to depositions to a base pressure of ~10^{-4} Pa using a turbomolecular pump. The In and Y targets were co-sputtered onto a 2 inch Si (100) substrate for 30 min at an Ar pressure of 0.35 Pa with DC powers of 25 W and 50 W, respectively. The depositions were carried out at room temperature, namely without intentional substrate heating.

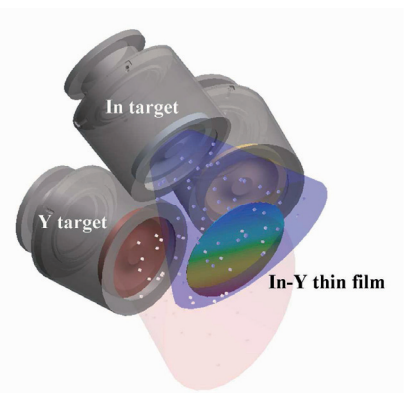

Figure 7.1 Schematic illustration of combinatorial magnetron sputtering set-up for deposition of In-Y thin films with composition gradient.

Detailed surface investigations were carried out in a scanning electron microscope (SEM, JEOL JSM-6480) equipped with an

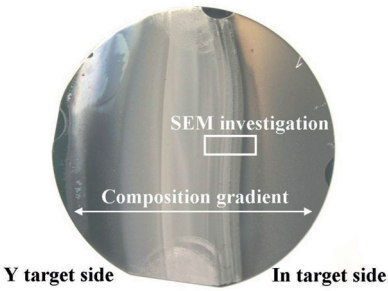

Figure 7.2 Photograph of In-Y thin film with lateral composition gradient deposited on 2 inch Si-wafer after exposure to atmosphere for 30 hours.

energy dispersive X-ray analyzer (EDX, EDAX Genesis 2000). The investigations were focused on a film surface segment including compositions close to YIn_3 at which an appreciable amount of whiskers was observed. For the EDX analysis, In-*L*, Y-*L*, and O-*K* characteristic X-ray lines were used for the identification of In, Y, and O, respectively. In-Y compositions were quantified using the ZAF method. In addition to the morphological and compositional studies, structural analysis was performed by micro X-ray diffraction using a general area diffraction detector system (GADDS, Bruker D8) with a collimated X-ray beam (Cu-K_α) using a pin-hole collimator with 0.5 mm in diameter. The voltage and current settings were 40 kV and 40 mA, respectively. The incident angle of the X-ray beam was fixed at 15°.

7.3 Results and Discussion

After exposure of the as-deposited films to atmosphere, In-whiskers were found to form spontaneously on certain film surface segments. Figure 7.2 shows a photograph of an In-Y film kept in atmosphere for 30 hours at room temperature. One can see a variation in film surface appearance along its composition gradient. As it will be shown below, this is primarily due to a variation of surface topographical features including different size and morphology of In-whisker formation.

Figure 7.3(a) shows a SEM micrograph obtained from a selected area of the film shown in Figure 7.2. SEM micrographs of Figures 7.3(b)-(g) were obtained from positions denoted by b-g in Figure 7.3(a). After exposure of the film to atmosphere, whiskers are found to grow

spontaneously on the film surface investigated. According to EDX measurements, no evidence for the presence of Y in the whiskers could be detected. The morphology, size, and population of In-whiskers appear to be

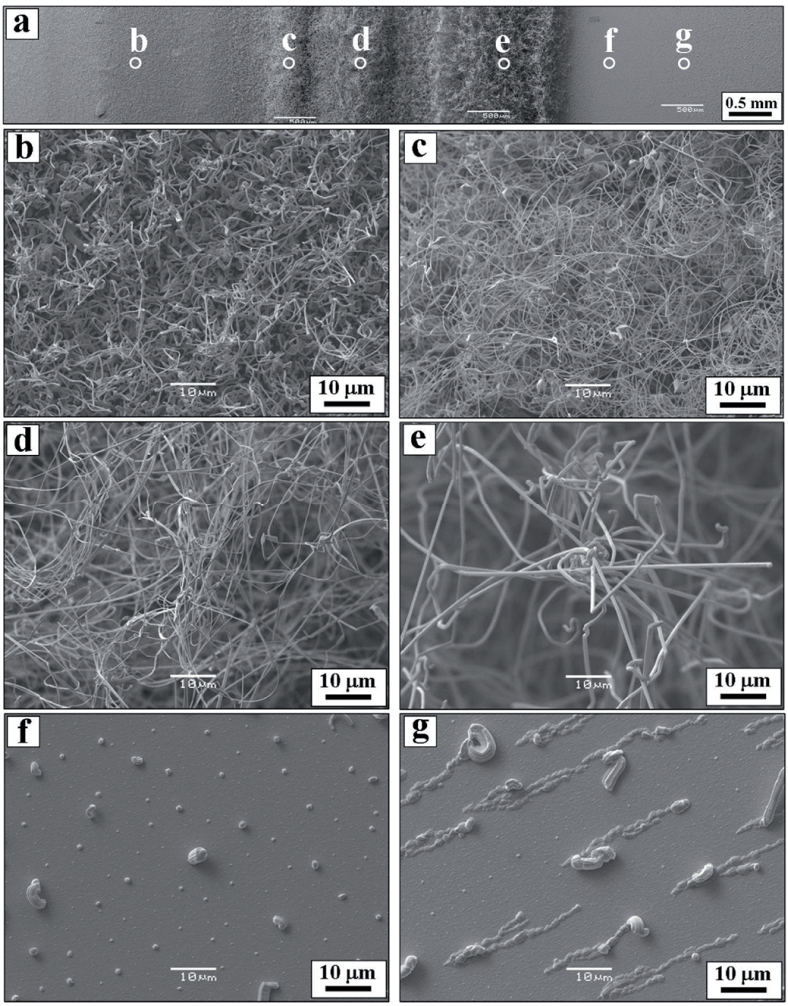

Figure 7.3 SEM micrographs showing a variety of In-whisker morphologies obtained from the marked area in Figure 7.2: (a) large area, low magnification image, and (b)-(g) high magnification images taken from positions denoted by (b)-(g) in Figure 7.3(a).

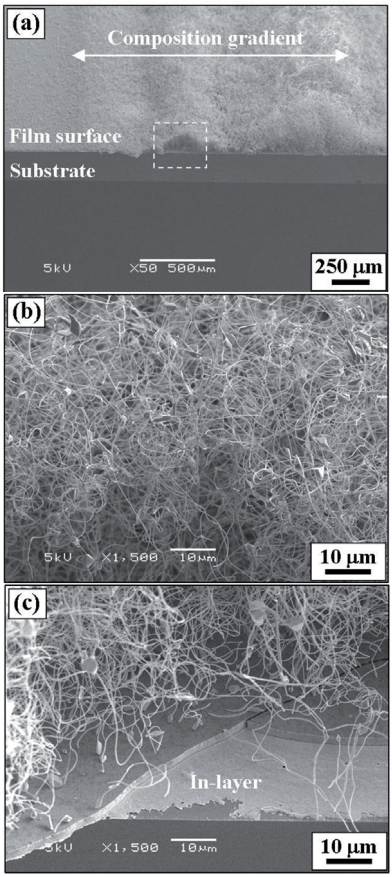

Figure 7.4 SEM micrographs showing cross-sectional features of a film with composition gradient: (a) low magnification image (left side corresponds to In-rich area), high magnification images of a top (b), and a bottom (c) part of In-whiskers grown. The micrographs were taken after one month exposure to atmosphere.

largely dependent on the position along the In-Y concentration gradient, and hence on the as-deposited film composition. The In-whisker diameter observed ranges from ~0.2 μm to a few μm and occasionally even larger. It should be noted that such a small size of whiskers with the diameter of, in particular, < 1 μm is not common for typical spontaneous Sn-whiskers observed in plating. Generally speaking, thin In-whiskers with the diameter of < 1 μm with large population are observed at the film compositions close to stoichiometric YIn_3 while thicker whiskers with smaller population are primarily located at the In-rich side. When the Y composition is reduced to approximately 18 at.% (balance to 100 at.% is In), no whisker formation is observed, instead, hillock or nodule-like structures appear. Thus, an appreciable amount of spontaneous In-whiskering is confined to a narrow concentration range of 18 to 25 at.%Y.

To determine the cause for In-whisker formation, film cross-sections were studied. Figure 7.4 provides cross-sectional SEM images obtained

from a segment of a film exhibiting the growth of In-whiskers after exposure to atmosphere. The substrate was cleaved along the composition gradient. Figures 7.4(b) and (c) display whiskers in the upper and lower region of the frame shown in Figure 7.4(a), respectively. The growth of In-whiskers with the diameter of a few hundreds nanometers can be seen in Figure 7.4(b). Figure 7.4(c) shows cross-sectional as well as surface features of the In-Y film after In-whisker formation. In-whiskers are connected to the film surface at their roots. In addition, compared with a large tangle of In-whiskers seen from a top view (Figure 7.4(b)), the actual population of roots at the film surface appears to be relatively small.

The spontaneous growth mechanism of In-whiskers from YIn_3 thin films presented here is believed to be similar to the one proposed previously for rapid Sn-whisker formation from $RESn_3$ compounds [22, 24]. Namely, the growth of In-whiskers is driven by the preferential reaction of Y with atmosphere to form Y oxides and/or Y hydroxides. In the case of Y, the following reactions might occur upon exposure.

$$4YIn_3 + 3O_2 \rightarrow 2Y_2O_3 + 12In \quad (7.1)$$

$$2YIn_3 + 6H_2O \rightarrow 2Y(OH)_3 + 6In + 3H_2 \quad (7.2)$$

These reactions are energetically preferred because of the large exothermic standard enthalpies of formation for Y_2O_3 (-1919.4 kJ/mol [31]) and $Y(OH)_3$ (-1472.3 kJ/mol [32]) compared to that for YIn_3 (-41.8 kJ/mol [29]). While the formation of Y_2O_3 and/or $Y(OH)_3$ provides free In atoms, a large volume expansion occurs. Using molar volumes of In (1.57×10^{-5} m^3/mol), YIn_3 (5.83×10^{-5} m^3/mol [33]), Y_2O_3 (4.49×10^{-5} m^3/mol [34]), and $Y(OH)_3$ (3.62×10^{-5} m^3/mol [35]), one can estimate possible volume changes of +19.3% and +42.9% for the formation of Y_2O_3 and $Y(OH)_3$, respectively. These large expansive volume strain values cause compressive stresses in the film, which eventually act as the major driving force for In-whisker extrusion.

It is also interesting to notice in Figure 7.4(c) that a layer of In is formed at the film-substrate interface. This is expected to happen if the In

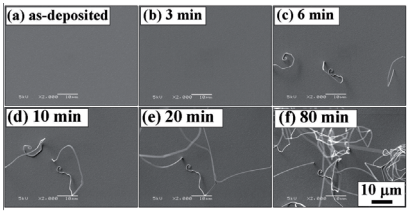

Figure 7.5 Series of SEM micrographs showing temporal growth behavior of In-whisker with different atmosphere exposure time: (a) as-deposited, (b) after 3 min, (c) 6 min, (d) 10 min, (e) 20 min, and (f) 80 min.

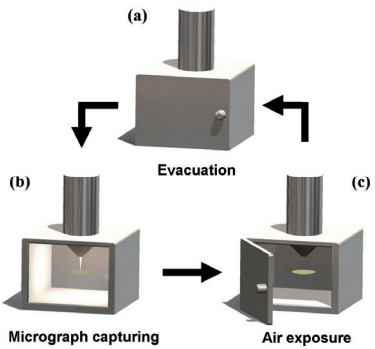

Figure 7.6 Schematic illustration of the SEM observation process to capture the growth behavior of In-whisker upon atmosphere exposure. The process of (a) evacuation, (b) micrograph capturing, and (c) atmosphere exposure is repeated several times.

extrusion force is larger than the adhesive forces between the film and the substrate.

To further verify the hypothesis of atmosphere exposure induced In-whisker growth, we have studied the temporal growth behavior of In-whiskers during exposure. Figure 7.5 illustrates a series of SEM micrographs showing an initial stage of In-whisker growth. In order to capture a surface condition as close as possible to as-deposited state, an In-Y film was transferred from the deposition chamber to the SEM chamber within < 5 min exposure time. After the first micrograph was captured at a selected position on the film surface as shown in Figure 7.5(a), the SEM chamber was vented, thus intentionally exposing the film surface to atmosphere for a certain time. Then, the chamber was evacuated again, and a subsequent micrograph was acquired at the same position as the previous one. As schematically illustrated in Figure 7.6, this exposure-observation process was repeated several times to reveal an initial stage of whisker growth. The exposure time given in each micrograph in the figures represents the total exposure time measured from the first venting process.

It is obvious from the images shown in Figure 7.5 that In-whiskers are extruded spontaneously from the film surface upon atmosphere exposure. According to EDX measurement performed on the smooth surface shown in Figure 7.5(a), the film composition was determined to be about 22 at.%Y. After an incubation time of ~3 min, the whisker nucleation occurs, and they grow continuously as the exposure time is increased. Based on a rough measurement of the change in whisker length with time, the whisker growth rate is estimated to be as high as ~1500 Å/s corresponding to the growth of a 30 μm long whisker in 3 min, according to Figure 7.5(c). This is even two orders of magnitude larger than those observed for bulk $RESM_3$ compounds (~10 Å/s) [22, 26]. The reason for this rather extensive difference in growth rate between YIn_3 thin films and bulk $RESM_3$ compounds is unknown at this moment. As we will discuss later, the difference in microstructures between thin films and bulk materials may be responsible.

It is also of great importance to mention here that in high vacuum no measurable dimensional change of In-whiskers was observed when the film was kept in the SEM chamber for 24 hours. This suggests that, for In-whisker growth to occur, a reaction between the YIn_3 films and atmosphere is essential as suggested previously for SM-whisker formation from $RESM_3$ compounds [20-23].

Figure 7.7 shows a series of SEM micrographs (Figures 7.7(a)-(c)) and X-ray diffraction (XRD) patterns (Figure 7.7(d)) upon exposure to atmosphere obtained at the film composition of about 21 at.%Y. The collimated X-ray results in an irradiated surface area of ellipse with the transverse diameter of 2.5 mm in the present measurement set-up. In order to minimize a concentration spread within the irradiated area, the measurement was carried out in such a way that the transverse direction of the ellipse was perpendicular to the concentration gradient in the film. Hence, the position for the SEM observations and XRD measurements are almost identical. Although the XRD measurements were carried out under

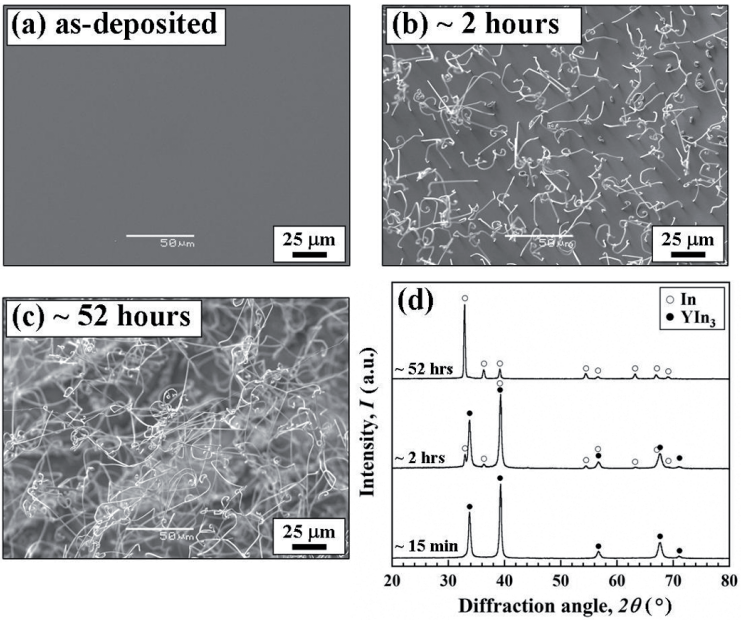

Figure 7.7 Temporal structural evolution on film surface with different atmosphere exposure time: SEM micrographs for (a) as-deposited, (b) after ~2 hours, (c) after ~52 hours, and (d) corresponding XRD patterns.

exposure, the use of the GADDS system with an areal detector enabled fast acquisition of diffraction patterns. The acquisition time for patterns was only 2 min which minimized possible changes of the diffraction patterns due to In-whisker growth during measurements. The XRD pattern for as-deposited state, i.e. total exposure time < 15 min, indicates that the film structure is single phase cubic $L1_2$-YIn_3, see Figure 7.7(d). Hence, the formation of metastable cubic fcc $Y_{1-x}In_3$ phase with a slight Y deficiency appears likely. The formation of metastable phases is commonly observed during low temperature thin film growth [36]. In-whiskers grow continuously upon further exposure, see Figures 7.7(b) and (c), and correspondingly diffraction peaks originating from the tetragonal In phase appear, see Figure 7.7(d). Although we expected the formation of Y_2O_3 and/or $Y(OH)_3$ in the film after

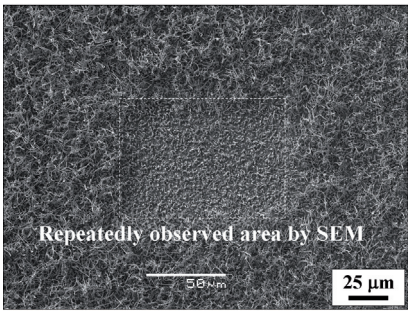

Figure 7.8 SEM micrograph showing area of retardation of In-whisker growth after being repeatedly exposed to an electron beam.

exposure, the presence of those compounds was not detected by XRD. This may be due to the formation of amorphous oxides and/or hydroxides due to the fact that the reactions take place at room temperature.

The importance of reactions between the In-Y film surface and atmosphere for In-whisker growth is emphasized by a SEM micrograph shown in Figure 7.8. A frame at the center represents an area which has been investigated repeatedly by SEM for studying In-whisker growth process. It is obvious that less In-whiskers grow on the surface after being observed by SEM than in the close vicinity thereof. This indicates that electron beam irradiation of the film surface during observation retards the In-whisker growth kinetics. Xian and Liu have also reported that the spontaneous Sn-whisker growth from $NdSn_3$ compound was stopped after being observed in SEM [26]. It is common that carbon contamination thin films are formed on the sample surface being investigated by SEM due to the interaction of the electron beam with the absorbed surface layers [37]. As a possible reason for retardation of In-whisker growth as shown in Figure 7.8, therefore, we suggest that a carbon layer forms on the surface after being observed repeatedly by SEM, and acts as a protective layer against reactions with atmosphere.

To further study possible reactions with atmosphere upon exposure to air and the correlation to In-whisker formation, temporal changes in film composition upon exposure have been investigated as well. Figures 7.9(a) and (b) show the changes in film composition as a function of exposure time at two different as-deposited compositions, (a) 22 and (b) 25 at.%Y.

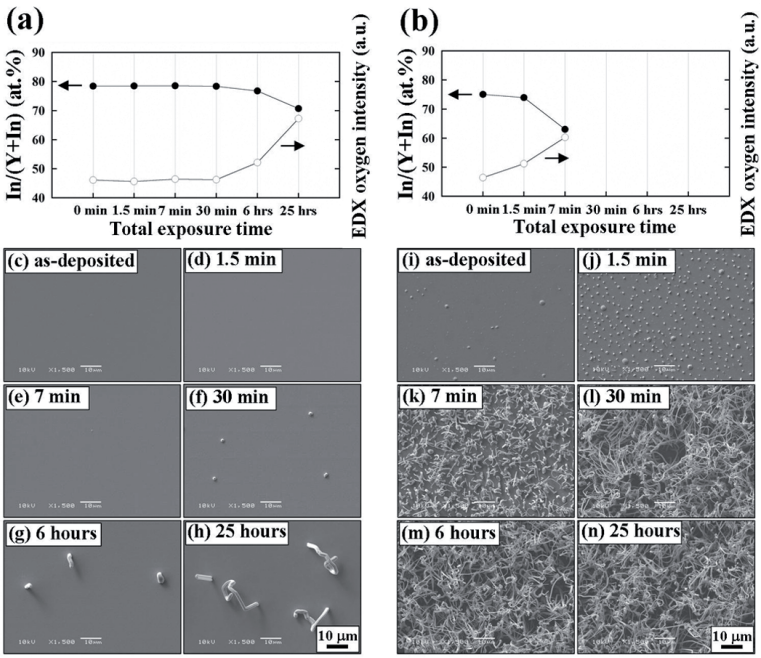

Figure 7.9 Temporal changes of film compositions and In-whisker growth with different atmosphere exposure time for two different as-deposited films with 22 at.%Y, (a) EDX result, (c)-(h) SEM micrographs, and 25 at.%Y (b) EDX result, (i)-(n) SEM micrographs.

The corresponding SEM micrographs after each exposure time are given in Figures 7.9(c)-(n). However, the investigation positions were slightly shifted intentionally after each exposure to exclude the influence of electron beam radiation as discussed above. The EDX analyzes were carried out using a spot-mode focused only on the film surface to avoid signal from the In-whiskers. Since the quantification of oxygen content using EDX is considered to be less reliable without using a suitable standard sample, only a relative change in intensity of O-*K* characteristic X-ray peak was used as an indicator for oxygen content in the film.

It should be noted that there is a large difference in morphology and extrusion kinetics of In-whiskers at two different as-deposited film

compositions of 22 and 25 at.%Y, see Figure 7.9. In both cases, the oxygen content in the film increases as the exposure time is increased. On the other hand, the In content decreases as In-whiskers grow upon exposure. This indicates that the diffusion of In atoms to the roots of growing In-whiskers occurs upon exposure. Furthermore, as can be seen for 22 at.%Y, the nucleation and subsequent growth of In-whiskers seem to be correlated with the onset of the increase in oxygen content in the film. This supports the hypothesis that the formation of Y_2O_3 and/or $Y(OH)_3$ is involved for the growth of In-whiskers upon exposure of In-Y thin films.

One of the most interesting phenomena observed in the present In-Y thin film study is that the morphology and extrusion kinetics of In-whiskers are strongly affected by the chemical composition, even within the narrow composition range of 18 to 25 at.%Y. This range could be related to a possible homogeneity range for the formation of single phase $Y_{1-x}In_3$ with an Y deficiency. However, a more systematic study for the correlation between the composition, phase constitution, and morphology in as-deposited In-Y thin films is necessary for better understanding. As for the size of whiskers, Tu *et al.* have proposed that radius of Sn-whisker, R, is determined by a balance between surface energy per unit area, γ, and strain energy per unit volume, ε, as following [15],

$$R = 2\gamma / \varepsilon \tag{7.3}$$

Thus, qualitatively speaking, thin (thick) In-whiskers are expected to form when the strain energy, hence compressive stress, is large (small). It might be the case that the change in Y composition causes the change in reactivity between In-Y thin films and atmosphere, and hence the change in strain energy stored in the film. A lower strain energy should be associated with a lower Y content in the film simply because of the smaller volume of Y_2O_3 and/or $Y(OH)_3$ which could be formed. This is consistent with the here reported observation that thicker In-whiskers are formed at smaller Y concentrations than the nominal YIn_3. It should also be pointed out that the

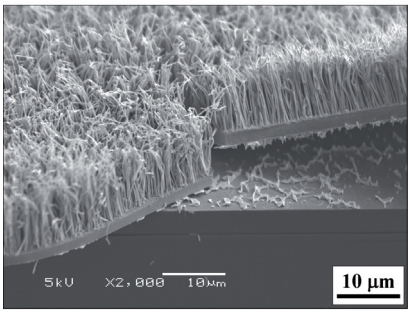

Figure 7.10 SEM micrograph of uniform, dense In-whisker structure forming on a film surface. This micrograph was taken after three days exposure.

In-whisker growth behavior may be influenced not only by the chemical composition, but also by the constitution and microstructure of the film. Sputtered thin films are known to exhibit quite different microstructural features compared to bulk materials [36]. For instance, the grain size of sputtered thin films is often in the range of 10-100 nm, which is one or two orders of magnitude smaller than those of typical bulk polycrystalline materials. Because of the large grain boundary density, the film reactivity to atmosphere is expected to be enhanced due to grain boundary diffusion as compared to bulk samples. The very large whisker growth rate, ~1500 Å/s, obtained in the present thin film study may be understood in terms of an accelerated reaction due to fine grain structures of the thin films.

Finally, as already mentioned above, the use of compositionally graded In-Y thin films enables the efficient investigation of interesting morphological In-whisker features. For instance, in Figure 7.10, a cross-sectional feature of a film exhibiting uniquely self-organized In-whiskers is presented. The thin In-whiskers with the diameter of ~0.2 μm are well-aligned, highly densely in a large area along the surface normal, and the length of each whisker is very similar and about 10 μm. This suggests that the whiskers nucleate almost simultaneously. This type of whisker morphology may be useful for application where a large surface to volume ratio is required.

7.4 Conclusions

In this study the spontaneous formation of In-whiskers from YIn_3 thin films deposited by combinatorial magnetron sputtering was presented. In-whiskers were found to be extruded spontaneously from the roots only upon exposure of the films to atmosphere, but not in vacuum. In-whisker growth is accompanied by an increase in oxygen content in the films. It is suggested that the In-whiskers are extruded from the film surface due to compressive stresses developed by preferential reactions of Y to form more stable compounds such as Y_2O_3.

It was also found that the morphology and extrusion kinetics of In-whiskers were strongly dependent on the Y composition of as-deposited films. The diameter of the In-whiskers observed ranges from ~0.2 μm up to a few μm or even larger within a composition range between 18 and 25 at.%Y. Based on these data, the whisker morphology and growth kinetics can be controlled through tuning the film composition. The results provide an alternative pathway towards the controlled growth of one-dimensional submicron/nanostructured materials.

References

[1] C.M. Lieber, Z. L. Wang, MRS Bull. 32 (2007) 99.
[2] Y. Xia, P. Yang, Y. Sun, Y. Wu, B. Mayers, B. Gates, Y. Yin, F. Kim, H. Yan, Adv. Mater. 15 (2003) 353.
[3] R.S. Wagner, W.C. Ellis, Appl. Phys. Lett. 4 (1964) 89.
[4] J.D. Holmes, K.P. Johnston, R.C. Doty, B.A. Korgel, Science 287 (2000) 1471.
[5] T.J. Trentler, K.M. Hickman, S.C. Goel, A.M. Viano, P.C. Gibbons, W.E. Buhro, Science, 270 (1995) 1791.
[6] Y.F. Zhang, Y.H. Tang, N. Wang, D.P. Yu, C.S. Lee, I. Bello, S.T. Lee, Appl. Phys. Lett. 72 (1998)1835.
[7] A.M. Morales, C.M. Lieber, Science 279 (1998) 208.
[8] B.D. Yao, Y.F. Chan, N. Wang, Appl. Phys. Lett. 81 (2002) 757.
[9] Y.C. Kong, D.P. Yu, B. Zhang, W. Fang, S.Q. Feng, Appl. Phys. Lett. 78 (2001) 407.
[10] U. Lindborg, Acta Metall. 24 (1976) 181.
[11] U. Lindborg, Metall. Mater. Trans. A 6 (1975) 1581.

[12] P.L. Key, Proc. 20th Electronic Components Conference (1970) 155.
[13] R.M. Fisher, L.S. Darken, K.G. Carroll, Acta Metall. 2 (1954) 368.
[14] B.Z. Lee, D.N. Lee, Acta Mater. 46 (1998) 3701.
[15] K.N. Tu, C. Chen, A.T. Wu, J. Mater. Sci.: Mater. Electron.18 (2007) 269.
[16] W. Shim, J. Ham, K. Lee, W.Y. Jeung, M. Johnson, W. Lee, Nano Lett. 9 (2009) 18.
[17] M. Saka, F. Yamaya, and H. Tohmyoh, Scr. Mater. 56 (2007) 1031.
[18] Y.T. Cheng, A.M. Weiner, C.A. Wong, M.P. Balogh, M.J. Lukitsch, Appl. Phys. Lett. 81 (2002) 3248.
[19] M.W. Barsoum, E.N. Hoffman, R.D. Doherty, S. Gupta, A. Zavaliangos, Phys. Rev. Lett. 93 (2004) 206104-1.
[20] T.H. Chuang, Scr. Mater. 55 (2006) 983.
[21] T.H. Chuang, C.C. Chi, H.J. Lin, Metall. Mater. Trans. A 39A (2008) 604.
[22] T.H. Chuang, S.F. Yen, J.Electron. Mater. 35 (2006) 1621.
[23] M.A. Dudek, N. Chawla, J. Electron. Mater. 38 (2009) 210.
[24] M.A. Dudek, N. Chawla, Acta Mater. 57 (2009) 4588.
[25] M. Liu, A.P. Xian, J. Alloys Compd. 486 (2009) 590.
[26] A.P. Xian, M. Liu, J. Mater. Res. 24 (2009) 2775.
[27] K.N. Tu, Acta Metall. 21 (1973) 347.
[28] V.K. Glazunova, K.M. Gorbunova, J. Cryst. Growth,10 (1971) 85.
[29] A. Palenzona, S. Cirafici, Thermochim. Acta 13 (1975) 357.
[30] G. Cheng, E. Stern, S. Guthrie, M.A. Reed, R. Klie, Y. Hao, G. Meng, L. Zhang, Appl. Phys. A: Mater. Sci. Process. 85 (2006) 233.
[31] E.G. Lavut, N.V. Chelovskaya, J. Chem. Thermodyn. 22 (1990) 817.
[32] I.I. Diakonov, K.V. Ragnarsdottir, B. R. Tagirov, Chem. Geol. 151 (1998) 327.
[33] K.H.J. Buschow, H.W. de Wijn, A.M. van Diepen, J. Chem. Phys. 50 (1969) 137.
[34] L. Smrcok, Cryst. Res. Technol. 24 (1989) 607.
[35] G.W. Beall, W.O. Milligan, H.A. Wolcott, J. Inorg. Nucl. Chem. 39 (1977) 65.
[36] J.A. Thornton, Annu. Rev. Mater. Sci. 7 (1977) 239.
[37] W.A. Knox, Ultramicroscopy 1 (1976) 175.

Chapter 8
Summary

It has previously been suggested based on *ab initio* calculations that non-oxide perovskites with the general formula of AB_3X, where *A* and *B* are metals, and *X* is B, C, or N, may exhibit unique mechanical properties such as superior ductility, and hence serve as a damage tolerant material. The first part of this thesis work explores the mechanical properties of non-oxide perovskite phases through thin film approach. Ternary perovskite borides and iron based perovskite nitrides were the main material systems investigated in the present work.

YPd_3B ($YPd_{2.73}B_{1.18}$) thin films were synthesized at low temperatures using combinatorial magnetron sputtering, and the mechanical properties thereof were studied by nanoindentation. The elastic modulus was determined to be 137 ± 2 GPa, which was in good agreement with *ab initio* data. The onset of plasticity was also studied using the Hertz elastic contact theory. The analyzed critical shear stress for plastic deformation was found to be comparable to typical ductile metallic materials, indicating that YPd_3B was also classified as ductile material. (Chapter 3)

The elastic properties of iron based perovskite Fe_4N were studied experimentally and theoretically. Two different types of samples, i.e. sputtered thin films and porous bulk-like samples, were employed for nanoindentation measurements. The elastic moduli of Fe_4N thin films and bulk-like samples were measured to be 157 ± 11 GPa and 159 ± 17 GPa, respectively, which were consistent with *ab initio* calculations. The influence of porosity on the nanoindentation measurement for the bulk-like sample was corrected by the measurement of “structural compliance”. The measured elastic modulus of Fe_4N was apparently lower than those of austenitic stainless steels in spite of their structural similarity. The

comparatively low elastic modulus, but high hardness of Fe_4N can be understood in terms of elastic anisotropy. (Chapter 4)

Zn-containing iron nitride $ZnFe_3N$ thin films were proposed as a new corrosion protective coating for steels. $ZnFe_3N$ thin films were synthesized both on Si and steel substrates, and the mechanical properties thereof were probed by nanoindentation. The ductile behavior of $ZnFe_3N$ was predicted based on *ab initio* calculations. The measured elastic modulus and hardness of the $ZnFe_3N$ films were determined to be 244 ± 22 and 12 ± 2 GPa, respectively. Good agreement was obtained between experiment and theory in terms of the elastic properties. (Chapter 5)

The influence of Pd substitution on the elastic modulus of Fe_4N was studied. $PdFe_3N$ thin films as well as compositionally spread $Pd_xFe_{4-x}N$ thin films were deposited by combinatorial magnetron sputtering. Based on the nanoindentation results, the elastic modulus of $PdFe_3N$ thin film was 170 ± 14 GPa GPa whereas *ab initio* calculations predicted the value of 225 GPa. The reason for this relatively large discrepancy between experiment and theory is not clear. A possible modification of the magnetic state of the $PdFe_3N$ thin films might affect the measured elastic modulus in conjunction with the magneto-volume effect. The systematic study on the combinatorial $Pd_xFe_{4-x}N$ thin films revealed that the influence of the Pd concentration on the elastic modulus was small. According to the evaluation of the critical shear stresses for the onset of plasticity, $PdFe_3N$ as well as Fe_4N were expected be classified as ductile material. (Chapter 6)

In the second part of this thesis work, the spontaneous growth of soft metal nanowhiskers was investigated using the combinatorial thin film approach. In-Y binary thin films with compositional gradients were deposited. In-whiskers were found to be extruded spontaneously from the roots of whiskers only upon exposure of the films to atmosphere, but not in vacuum. In-whisker growth was accompanied by an increase in oxygen content in

the films. It was suggested that the In-whiskers are extruded from the film surface due to compressive stresses developed by preferential reactions of Y to form more stable compounds such as Y_2O_3.

It was also found that the morphology and extrusion kinetics of In-whiskers were strongly dependent on the Y composition of as-deposited films. The diameter of the In-whiskers observed ranged from ~0.2 μm up to a few μm or even larger within a composition range between 18 and 25 at.%Y. Based on these data, the whisker morphology and growth kinetics can be controlled through tuning the film composition. The results provide an alternative pathway towards the controlled growth of one-dimensional submicron/nanostructured materials. (Chapter 7)

Curriculum Vitae

Name: Tetsuya Takahashi

Date of Birth: 07 August 1979

Place of Birth: Tochigi in JAPAN

06/2006 – 09/2011:

Wissenschaftlicher Mitarbeiter (Ph.D candidate), Materials Chemistry, RWTH Aachen University, Germany

Education

10/2003 – 05/2006:

Master Program, Metallurgical Engineering, Physical Metallurgy and Materials, RWTH Aachen University, Aachen, Germany

04/2002 – 09/2003:

Graduate School, Department of Production Systems Engineering, Toyohashi University of Technology, Aichi, Japan

04/1998 – 03/2002:

Department of Production Systems Engineering, Toyohashi University of Technology, Aichi, Japan

Academic qualifications

05/2006 Master of Science, RWTH Aachen University, Aachen, Germany (Thesis completed at Max-Planck Institut für Eisenforschung, Düsseldorf, Germany)

03/2002 Bachelor of Engineering, Toyohashi University of Technology